2015

CFD Simulation of Impinging Jet Flows and Boiling Heat Transfer

Mehrdad Shademan
University of Windsor

CFD Simulation of Impinging Jet Flows and Boiling Heat Transfer

By

Mehrdad Shademan

A Dissertation

Submitted to the Faculty of Graduate Studies

through the Department of Mechanical, Automotive & Materials Engineering

in Partial Fulfillment of the Requirements for

the Degree of Doctor of Philosophy

at the University of Windsor

Windsor, Ontario, Canada

2015

CFD Simulation of Impinging Jet Flows and Boiling Heat Transfer

By

Mehrdad Shademan

APPROVED BY:

_____

Dr. B.-C. Wang, External Examiner

University of Manitoba, Winnipeg, MB

_____

Dr. V.T. Roussinova

Department of Civil & Environmental Engineering

_____

Dr. G.W. Rankin

Department of Mechanical, Automotive & Materials Engineering

_____

Dr. A. Fartaj

Department of Mechanical, Automotive & Materials Engineering

_____

Dr. R. Balachandar (Co-Advisor)

Department of Mechanical, Automotive & Materials Engineering

_____

Dr. R.M. Barron (Co-Advisor)

Department of Mechanical, Automotive & Materials Engineering

Apr 21, 2015

DECLARATION OF CO-AUTHORSHIP/PREVIOUS PUBLICATION

I. Co-authorship Declaration

I hereby declare that this dissertation contains original material that is the result of joint research. R. Barron and R. Balachandar contributed to all chapters by providing the opportunities and facilities necessary to complete the research along with intellectual guidance. V. Roussinova also contributed to Chapter 3 by providing experimental results and constructive guidance, detailed comments and helpful direction. In all chapters, the ideas, data interpretation, and writing of all manuscripts and dissertation were performed by the author, Mehrdad Shademan.

I am aware of the University of Windsor Senate Policy on Authorship and I certify that I have properly acknowledged the contribution of other researchers to my thesis. I certify that, with the above qualification, this dissertation, and the research to which it refers, is the product of my own work.

II. Declaration of Previous Publications

This dissertation includes three original papers that have been previously published in peer-reviewed journals and conferences, as follows:

Dissertation Chapter	Publication tile/full citation	Publication status
Chapter 2	Shademan, M., Balachandar, R., Barron, R.M., 2013. CFD analysis of the effect of nozzle stand-off distance on turbulent impinging jets. Canadian Journal of Civil Engineering 40(7): 603-612	published
Chapter 3	Shademan, M., Roussinova, V., Barron, R.M., Balachandar, R., 2014. Large eddy simulation of round impinging jets with large stand-off distance. ASME Congress, Montreal, Canada	published
Chapter 4	Shademan, M., Balachandar, R., Barron, R.M., 2014. CFD simulation of boiling heat transfer using OpenFOAM. ASME Congress, Montreal, Canada	published

I certify that I have obtained written permission from the copyright owner(s) to include the above published material(s) in my dissertation. A copy of these written permissions is included in the Appendix. I certify that the above material describes work completed during my registration as a graduate student at the University of Windsor.

I certify that, to the best of my knowledge, my dissertation does not infringe upon anyone's copyright nor violate any proprietary rights and that any ideas, techniques, quotations, or any other material from the work of other people included in my dissertation, published or otherwise, are fully acknowledged in accordance with the standard referencing practices. Furthermore, to the extent that I have included copyrighted material that surpasses the bounds of fair dealing within the meaning of the Canada Copyright Act, I certify that I have obtained written permission from the copyright owner(s) to include such material(s) in my dissertation.

I declare that this is a true copy of my dissertation, including any final revisions, as approved by my dissertation committee and the Graduate Studies office, and that this dissertation has not been submitted for a higher degree to any other University or Institution.

ABSTRACT

Circular jets impinging vertically on flat surfaces have many practical applications in industry. Nozzle height-to-diameter ratio plays an important role in the performance of this type of jet.

In this thesis a step by step approach has been followed to cover different aspects of impinging jets. In the first step, a steady Reynolds-Averaged Navier-Stokes simulation has been carried out on impinging jets with different nozzle stand-off distances. A strong dependency of the jet characteristics on the nozzle height-to-diameter ratio was observed. The simulations show that an increase in this ratio results in larger shear stress and more distributed pressure on the wall.

In the second step, an unsteady simulation using Large Eddy Simulation has been performed on an impinging jet with large stand-off distance. Good agreement was observed between the mean value results obtained from the current simulations and experiments. Unlike impinging jets with small stand-off distance, where the ring-like vortices keep their interconnected shape upon reaching the plate, no sign of interconnection was observed on the plate for the large stand-off distance case. A large deflection of the jet stagnation streamline was observed in comparison to the cases with small nozzle height-to-diameter ratios. Large fluctuations of the unsteady wall shear stresses were also captured.

A boiling model was developed for impinging jets with heat transfer. An Eulerian-Eulerian two-phase flow model was implemented using an open source code for the simulation (OpenFOAM). Initially, an adiabatic two-phase model was developed for flow in a pipe. Following this, the energy equation was activated to

account for non-adiabatic and boiling conditions. The simulation predictions were found to be in reasonable agreement with the experimental data and show significant improvement over previous numerical results. Finally, the model was upgraded for an impinging jet flow by implementing new correlations. The results obtained from the current model show reasonable agreement with the experimental results. The model can be confidently used for the evaluation of adiabatic and non-adiabatic impinging jet flows.

DEDICATION

To my parents and my wife, Sara.

For their love and to whom I owe everything.

ACKNOWLEDGEMENTS

TABLE OF CONTENTS

CFD SIMULATION OF BOILING HEAT TRANSFER IN AN IMPINGING JET
USING OPENFOAM

LIST OF FIGURES

LIST OF TABLES

NOMENCLATURE

A_b	Area covered by nucleation bubbles
A_s	Surface area of the wall per unit volume
$\ddot{A}_w$	Contact area with the wall per unit volume
C_D	Drag force coefficient
C_L	Lift force coefficient
C_{hl}	Liquid Stanton number
C_{pl}	Specific heat of liquid
C_f	Fanning friction number
C_{WL}	Wall lubrication force coefficient
d_B	Bubble detachment diameter
d_{ref}	Reference diameter of bubbles
D	Nozzle diameter
f	Bubble detachment frequency
$\vec{F}$	Force
$\vec{F}_g^L$	Lift force
$\vec{F}_g^{WL}$	Wall lubrication force
$\vec{F}_g^{TD}$	Turbulent dispersion force
$\vec{F}_g^{VM}$	Virtual mass force
$\vec{F}_g^D$	Drag force
$\vec{g}$	Gravity acceleration
h_C	Convection heat transfer coefficient
h_{sat}	Saturation enthalpy of liquid
h_g	Enthalpy of gas phase
h_k	Specific enthalpy of phase k
h_l	Enthalpy of liquid
H	Nozzle height
IAC	Interfacial area concentration
N_w	Site density of bubbles
p	Pressure
P_s	Stagnation point pressure
q_k^t	Turbulent heat flux
$\ddot{q}_w$	Wall heat flux density
$\dot{q_W}$	Total heat flux from the wall
$\dot{Q_E}$	Evaporative heat flux
$\dot{Q_C}$	Convective heat flux
Q_k	Heat flux
$\dot{Q_Q}$	Quenching heat flux
$r_{1/2}$	Jet half width
R_k	Diffusion of phase k
R_k^t	Turbulent diffusion of phase k

Re	Reynolds number
t	Time
t_w	Bubble waiting time
T_1	Time period for roll up vortices close to the nozzle
T_2	Time period for large scale structures hitting the plate
T_w	Wall temperature
T_l	Liquid temperature
$T_{sat,l}$	Saturation temperature of liquid
u_τ	Shear velocity
$\overline{uu}$	Normal stress in x direction
$\overline{vv}$	Normal stress in y direction
$\overline{uu}$	Normal stress in z direction
$\overline{uv}$	Shear stress in x-y plane
$\overline{uw}$	Shear stress in x-z plane
$\overline{vw}$	Shear stress in y-z plane
U_j	Jet exit velocity
U_c	Jet centreline velocity
U_m	Jet radial maximum velocity
$\vec{U}_k$	Velocity of phase k

Greek symbols

δ_2	Distance above the plate at which V = 0.5Vm
ρ_k	Density of phase k
k	Turbulent kinetic energy
ε	Turbulent dissipation rate
ν	Kinematic viscosity
ω	Specific turbulent dissipation rate
θ	Circumferential direction
η	Kolmogorov length scale
Δ	Grid size
τ_{ij}	Subgrid-scale stresses
α_k	Void fraction of phase k
Γ_{ki}	Phase change from phase k to i
Γ_{ik}	Phase change from phase i to k
k_l	Heat conductivity of liquid
ΔT_{sub}	Subcooling temperature
ΔT_{sup}	Superheat temperature
$\emptyset^C$	Source term for bubble coalescence
$\emptyset^B$	Source term for bubble breakup
$\emptyset^{nuc}$	Source term for bubble nucleation
μ^{mol}	Molecular viscosity
μ^{bubble}	Bubble induced viscosity
μ^{turb}	Turbulent viscosity

CHAPTER 1

INTRODUCTION AND LITERATURE REVIEW

1.1. Background and motivation

Turbulent jets impinging on a flat surface are commonly used in many industrial applications where enhancement of heat and mass transfer is required. Examples of such applications include cooling, heating, cleaning and drying. In this type of flow, the flow field is a combination of several distinct features, such as a free jet, a stagnation flow, and a radial wall jet (see Fig. 1.1). Each of these flows has its own particular characteristics which have gained the attention of many researchers.
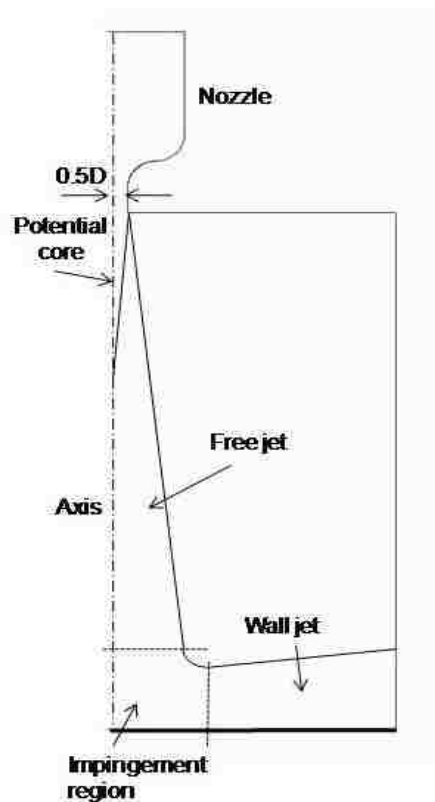
Fig. 1.1 Definition schematic of an axisymmetric impinging jet

1.1.1. Adiabatic round impinging jets

The characteristics of round impinging jets strongly depend upon several parameters such as Reynolds number, distance between the nozzle and the plate, nozzle geometry and the rate of turbulence introduced at the inlet to the domain (Manceau et al. 2014).

The core of the free jet is surrounded by a growing shear layer. In this shear layer the development of the Kelvin-Helmholtz instabilities results in the formation of ring vortices. Yule (1978) defined the term "vortex" as a part of a flow field accompanying a concentrated, continuous, coherent distribution of vorticity which is uniform in the direction of the vorticity vector. With increasing downstream distance the ring vortices change into large eddies. An eddy may be described as a vorticity containing region of fluid which can be identified as a moving coherent structure in the flow (Yule, 1978). These eddies are significant features of the turbulent region of the jet. However, features like three-dimensionality and irregularity of the vorticity field restrict us fromdenoting them as a ring vortex.

The ring vortices which change into large eddies (see Figs. 1.2 and 1.3) have a three-dimensional shape and have lost their axisymmetric behaviour. These eddies influence the flow field and cause pressure fluctuations on the plate (Hadziabdic and Hanjalic, 2008). This phenomenon causes an unsteady behaviour in the radial distributions ofwall shear stress and wall pressure and will eventually influence the rate of the heat transfer from the plate (Hall and Ewing, 2006). A wall jet is formed on the plate which is totally under the influence of the

unsteady structures impinging on the plate. These impinging unsteady structures cause separation and reattachment of the flow in the wall region which are associated with variations in the wall shear stress (El Hassan et al. 2013).
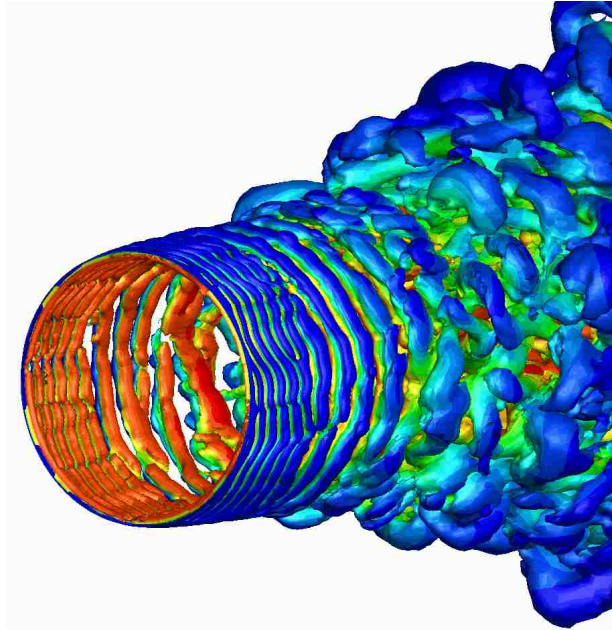
Fig. 1.2 Iso-surfaces of λ_2 criterion colored with velocity magnitude contours close to the nozzle exit

Fig. 1.3 Iso-surface of pressure contours (-20 Pa) (top view)

The jet exit mean velocity remains constant inside the core part of the free jet region, where the turbulence intensity is very low. Once the core reaches its maximum penetration, which is associated with an increase in turbulence intensity, a sharp decay in the jet centreline velocity occurs. Basically, penetration of the turbulence from the shear layer to the core part of the jet destroys the jet and results in a large decay in jet streamwise velocity. In the impinging zone, the flow loses its axial velocity and changes direction due to the presence of the plate. A wall jet is formed on the plate and attains a fully developed behaviour as it travels towards the downstream.

There are many numerical and experimental studies in the literature on different aspects of impinging jets. These analyses include investigations on the steady and unsteady flow parameters, effect of nozzle stand-off distance, behaviour of wall shear stress, pressure distribution and also separation and reattachment of flow along the wall jet zone.

On the experimental side, the work carried out by Yule (1978) has been of particular interest to researchers because of its fundamental overview on the physics of impinging jets. Yule (1978) showed that for impinging jets with large distance between the nozzle and the plate, large eddies have a wide range of sizes and trajectories with no symmetry between them. This phenomenon results in an unsteady three-dimensional behaviour of large scale structures causing pressure fluctuation in the impinging zone.

The effect of nozzle stand-off distance on flow parameters has been investigated by different researchers. Beltaos and Rajaratnam (1974, 1977)

classified impinging jets with H/D > 8.3 into three sub-regions including free jet, impinging region and wall jet zone as shown in Fig. 1.1. Following this, Giralt et al. (1977) conducted experiments on axisymmetric turbulent impinging jets for 3 < H/D < 25. They developed an experimental correlation between flow parameters and different H/D ratios. Although their study covered different H/D cases, it was limited to a mean value analysis and did not present any time history of the data.

Another aspect of impinging jetswhich has been investigated by different researchers is the behaviour of wall shear stress and static pressure in different flow configuration. Bradshaw and Love (1961) measured velocity, wall static pressure and skin friction for a case with H/D = 2. They observed that the high pressure region on the plate is slightly larger than the diameter of the jet. The peak of the wall skin friction magnitude occurred at a radius equal to that of the jet. A study carried out by Deshpande and Vaishnav (1982) showed a decreasing trend for the wall shear stress as the nozzle stand-off distance increases. Recent unsteady analysis of El Hassan et al. (2013) on the wall shear stress using particle image velocimetry showed significant influence of large-scale vortical structures on the wall shear stress (Re = 1260, H/D = 2). The influences of the vortex ring, the secondary and the tertiary vortices were reported to be the main mechanisms involved in the wall shear stress variation.

On the numerical side, there are different Reynolds-Averaged Navier-Stokes (RANS) analyses as well as Large Eddy Simulations (LES) and Direct Numerical Simulations (DNS) of impinging jets. In case of RANS analysis, most

6

of the studies are focused on the challenges associated with the turbulence modeling of impinging jets.

The research of Craft et al. (1993) is one of the fundamental RANS studies on impinging jets which investigates the issues with the turbulence modeling for this type of flow. The benchmarking of the simulations was performed using the experimental results of Cooper et al. (1993). Their study suggested the higher performance of the Reynolds Stress Model with the wall reflection models compared to other turbulence models.

Due to the limitations associated with LES and DNS computations, most of these studies deal with small H/D ratios. Olsson and Fuchs (1998) performed large eddy simulations for a case with H/D = 4. The purpose of their simulations was to study the turbulence parameters and the dynamic behaviour of impinging jets. They noticed generation of secondary vortices in the wall jet region which was found to be a result of primary vortices generated at the jet exit shear layer. They also observed that the primary vortices do not have an axisymmetric shape when approaching the plate.

Hadziabdic and Hanjalic (2008) used LES to analyze a circular impinging jet at Re = 20,000 and H/D = 2. The case that they analyzed showed that due to the small distance between the nozzle and the plate, the generated vortices are short-lived and undergo a faster stretching breakdown than in a free jet due to the radial deflection. They also noticed that because of the jet flapping, the stagnation point meanders in time around the jet geometrical centre. They concluded that the second peak in the Nusselt number observed along the plate

was due to the reattachment of the recirculation bubble and associated turbulence production.

Uddin et al. (2013) used LES to model impinging jets at two Reynolds numbers of 13,000 and 23,000 at H/D = 2, in order to extract the reason for the second peak observed in the radial distribution of the Nusselt number profile. They found that the flow acceleration in the developing region of the boundary layer is closely related to the secondary peak in the radial distribution of Nusselt number.

Wu and Piomelli (2014) performed LES to study the roughness effects on the evolution of azimuthal vortices in impinging jets with H/D = 1 and Re = 66,000. They modeled one case with laminar inflow and another one with turbulent inflow conditions. They observed a wider and weaker wall jet for the rough surface compared to the smooth surface for the turbulent case. They noticed that the peak of the velocity profile on the wall jet was shifted away from the plate. They concluded that roughness results in transition to the turbulence regime even if the inlet jet is laminar.

1.1.2. Round impinging jets with boiling heat transfer

One of the important applications of impinging jets in industry is their usage in removal ofalarge amount of heat from a surface. For example, impinging jets are used to cool electronic components in the computer industry and to dissipate the heat in pistons in the automotive industry. Boiling heat transfer may increase the heat transfer rate, while in other cases it significantly

reduces the heat transfer, which could allow the wall temperature to increase to the burnout point. Boiling heat transfer is characterized by a curve with different regimes, as shown in Fig. 1.4. In Regime I, due to the small temperature difference between the wall and liquid (wall superheat), the heat transfer mechanism is only through free convection. This single-phase heat transfer problem can be treated using common analytical solutions for free convection. The nucleate boiling regime, which is characterized by two sub-regimes (II and III), begins once bubbles are generated on the surface. Regime II refers to the condition when the isolated bubbles are formed at their own nucleation sites without interacting with each other when departing the surface. At higher wall superheat (Regime III), bubbles coalesce at different directionsas a consequence of higher nucleation frequency. Further increase of the wall superheat causes the boiling curve to rise to the local maximum heat flux point, called the critical heat flux (CHF). At this stage the high generation of vapor compared to previous stages results in a blockage between the surface and liquid. Therefore, heat must be transported through the vapor layer which is less efficient and results in a reduction in the heat flux. In the design of appliances working with boiling heat transfer, the CHF point is defined as a thermal limit in which further increase of wall superheat is accompanied with lower heat flux removal.
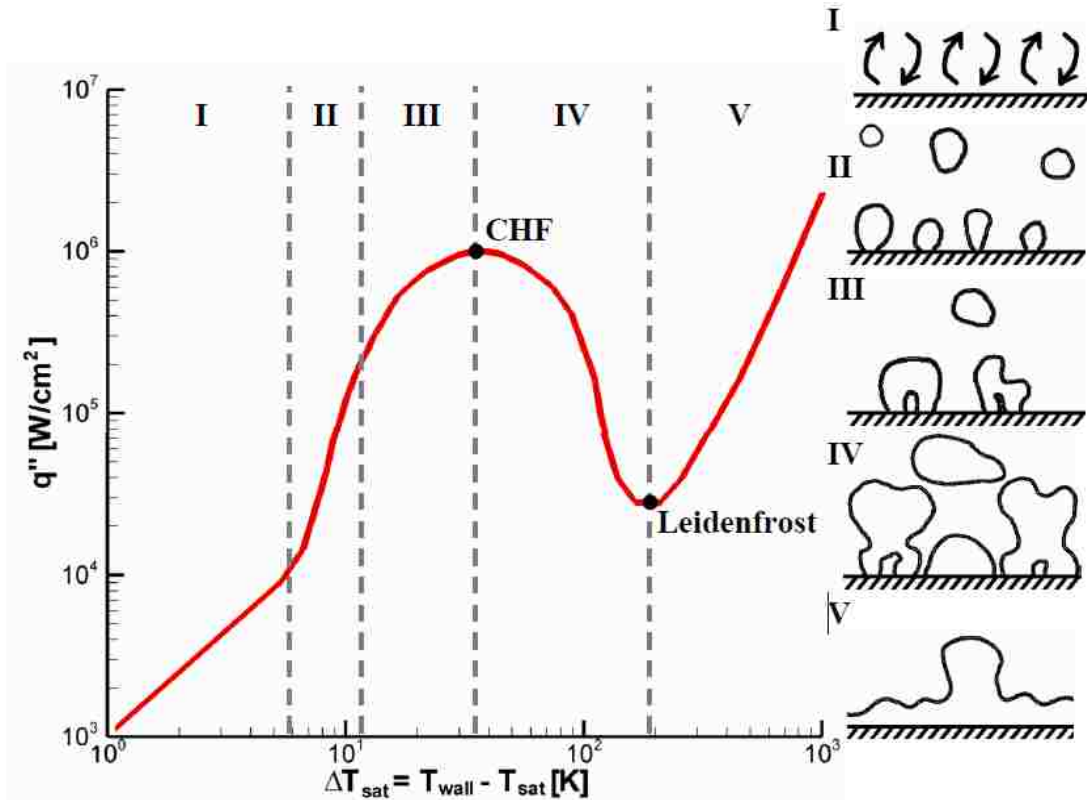
Fig. 1.4 Typical boiling curve and associated boiling regimes (Coursey, 2007)

The transition boiling regime (Regime IV) occurs after the CHF point, characterized by increasing wall temperature while the heat flux removal decreases. This is due to the increase of bubbles generated on the surface (dry area). Therefore, this regime is not known to present any practical applications. Finally, following the transition regime, the boiling curve reaches a local minimum point denoted as the Leidenfrost point. At this point, the surface enters the film-boiling regime (V). In this regime, in order to transfer heat to the liquid, it must be conducted across a continuous vapor film. This regime of heat transfer is an inefficient processand is not recommended for cooling purposes. It results in high heat fluxes but the temperature requirement is very high.

There are a number of studies in literature on the numerical modeling of subcooled boiling. Basically, most of these studies deal with the challenges of numerically modeling the boiling phenomenon and correlating it with the experimental results.In this regard, the model developed at Rensselaer Polytechnic Institute (RPI) by Kurul and Podowski (1990, 1991) has gained significant attention. According to the RPI model, the boiling heat transfer is divided into three components; convective, quenching and evaporative heat fluxes. The convective part provides for single-phase convection, quenching refers to liquid filling the wall vicinity after bubble detachment due to vaporization and the evaporative component is for the fluid that evaporates.

The numerical simulation of boiling heat transfer is performed by employing different two-phase flow methods. The Eulerian-Eulerian and Volume of Fluid (VOF) approaches are widely used for this purpose. The Eulerian-Eulerian method is more accurate because it solves the balance equations of mass, momentum and energy for both phases separately. However, it is computationally more expensive. The coupling of two phases is carried out by introducing source/sink terms such as interfacial forces and heat flux in these equations.

Krepper and Rzehak (2011) used the Eulerian-Eulerian approach in CFX software for modeling the boiling heat transfer in a pipe flow. Most of their results showed good agreement with the experimental results, except for the bubble size radial distribution. Evaluation of their model shows that there is no interfacial area concentration (IAC) equation solved in their simulation. IAC is responsible for

changes in the bubble size and takes into account the effect of bubble break-up and coalescence in the model. In their recent study, Krepper et al. (2013) updated their model by implementing a population balance method which takes into account the variation of bubble size due to bubble breakup/coalescence and condensation/evaporation processes. The quality of their results was significantly improved, especially for the bubble size distribution.

Michta (2011) and Michta et al. (2012) used OpenFOAM to model the boiling heat transfer in a pipe flow and considered the IAC equation as well as different interfacial forces in the model. The choice of OpenFOAM was based on the fact that it is an open source code and gives permission to the user to modify the code and to incorporate the appropriate experimental correlations. They found reasonable results in the adiabatic part of their code, however, for the boiling part the results were not in a good agreement with the experiments.

Kunkelmann and Stephan (2010) simulated the nucleate boiling heat transfer using the Volume of Fluid (VOF) method in OpenFOAM. The boiling of a single bubble was simulated by modifying the OpenFOAM default solver. Their model captured the growth, departure and movement of the bubble. Good agreement with the experimental results was observed for the bubble size as well as the mean wall superheat.

There are several different interfacial forces acting on both the continuum and dispersed phases in two-phase flows. They include, drag, lift, wall lubrication, turbulent dispersion and added mass forces. In order to properly model these interfacial forces which have a strong influence on the distribution of

the bubbles in two-phase flow simulations, different correlations have been suggested by different researchers. Drag is one of the primary interfacial forces which is generated by the continuous phase on the dispersed phase due to the movement of the dispersed phase. The correlation developed by Ishii and Zuber (1979) has been widely used for modelling the effect of the drag force. Tomiyama et al. (2002) measured trajectories of single air bubbles in simple shear flow to determine the transverse lift force acting on single bubbles. Their correlation has gained a lot of attention in the literature for modelling the lift force in two-phase flows. Antal et al. (1991) was the first to develop an analytical expression for the wall lubrication force. This is a repulsive force generated by the wall which pushes the bubbles away from it. Later, Tomiyama (1988) improved this model to pipe geometries. Frank (2005) upgraded the Tomiyama (1998) wall lubrication force coefficient and made it independent of the geometry. The virtual mass force which is generated due to the relative acceleration of one phase to the other is another important interfacial force. The correlation developed by Zuber (1964) has been widely used for the virtual mass force by many researchers.

Narumanchi et al. (2008) developed a numerical model for boiling heat transfer in an impinging jet. The application of their study was in the cooling of power electronic components. They employed the Eulerian-Eulerian approach in Fluent software and found reasonable results for the prediction of wall superheat in the stagnation point region. However, no information was provided about the use of IAC and other interfacial force equations in their model.

Abishek et al. (2013) numerically studied the effect of heater-nozzle ratio on the boiling phenomenon in an impinging jet. The jet Reynolds number was 2,500 with a subcooling of 20°C. They used the RPI model for decomposing the heat flux on the impingement plate and RNG k-ε to model the turbulence. The Eulerian-Eulerian two-phase flow model was used for the simulation. They found that irrespective of the heater-nozzle size ratio, at high superheat temperatures the quenching heat flux contributes to the major part of the heat flux. They also developed a correlation for the heat flux as a function of wall superheat and the size of the heater.

1.1.3. Objectives and outline of the dissertation

As the literature shows, there are many numerical and experimental simulations to study the various aspects of impinging jets. On the experimental side, detailed unsteady analysis of flow structures seem to be limited. On the numerical side, most of the unsteady studies are either RANS based or only cover small stand-off distances (H/D < 4).

In the first phase of this dissertation (Chapter 2), the mean value analysis is carried out on impinging jets to evaluate the effect of nozzle stand-off distance on different mean flow parameters. In this regard, Reynolds-Averaged Navier-Stokes simulations are carried out using different turbulence models at three nozzle height-to-diameter (H/D) ratios.

In the second phase (Chapter 3), due to the limited reporting of unsteady results, the analysis is extended to the transient case to better understand the

flow features at large nozzle height-to-diameter ratios. The objective is to answer critical questions raised by the steady analysis in Chapter 2. In this regard, an unsteady simulation using Large Eddy Simulation (LES) is carried out on an impinging jet with H/D = 20.

Commercial software has limitations in implementing the appropriate experimental correlations for every simulation, Furthermore, due to the inaccuracy observed in the previous numerical simulations of boiling heat transfer, it is of interest to develop a CFD code to simulate the boiling heat transfer for an impinging jet. As the literature shows, previous CFD approaches for boiling simulation in impinging jets do not take into account all aspects of two-phase flow phenomenon, particularly in the boiling part of the model. In this regard, adetailed Eulerian-Eulerian two-phase flow model was developed using the open source codeOpenFOAM, which takes into account the effects of interfacial forces, breakup/coalescence of the bubbles as well as the interfacial area concentration (IAC) equation (chapter 4). It is expected that the model developed in this dissertation presents more accurate results than previous investigations and advances the state-of-the-art research on boiling simulation for both pipe flow and impinging jets.

CHAPTER 2

RANS ANALYSIS OF THE EFFECT OF NOZZLE STAND-OFF DISTANCE

ON TURBULENT IMPINGING JETS

2.1. Introduction

Reynolds-Averaged Navier-Stokes (RANS) simulations have been carried out on turbulent impinging jets to evaluate the effect of nozzle height-to-diameter ratio on different flow parameters. In this regard, three cases with different H/D ratios have been selected for the simulations, corresponding to short (H/D = 2), intermediate (H/D = 6) and long (H/D = 18.5) jets.

Circular jets impinging vertically on flat surfaces have many practical applications such as in heating, cooling, metal cutting, fabric weaving and cleaning. Most of the experiments on impinging jets have been performed for short stand-off distances, i.e., with an impingement height (H) to nozzle diameter (D) ratio of less than six. Cooper et al. (1993) carried out experiments on a jet impinging on a large plane surface and measured mean and turbulence quantities in different regions of the jet. They considered two Reynolds numbers, 23,000 and 70,000, while the H/D ratio varied from two to ten, with particular focus between two and six. For H/D < 6, researchers have found that the core of the jet is still developing when reaching the plate surface (Nishino et al. 1996; Hadziabdic and Hanjalic 2008, Shademan et al. 2013).

For larger impingement heights (H/D > 8.3), Beltaos and Rajaratnam (1974, 1977) classified the flow into three different regions: the free jet portion (region I), the impingement zone (region II) and the axisymmetric wall jet portion (region III), as illustrated in Fig. 2.1.Giralt et al. (1977) conducted experiments on axisymmetric turbulent impinging jets with H/D ratios ranging from 3 to 25 at Re =

34,000 up to 80,000. Based on their experimental data, they developed a conceptual model for submerged, axisymmetric, turbulent impinging jets, which can be used to analyze the effect of increasing the nozzle distance from the plate. Recently, Rajaratnam et al. (2010) performed measurements on an impinging jet with a large H/D ratio of 18.5 at Re = 100,000 using a standard constant temperature hot-wire anemometer and evaluated the mean and turbulence characteristics in regions I and II. They noticed self-similarity in the radial distribution of mean velocity profiles up to regions close to the impingement zone.
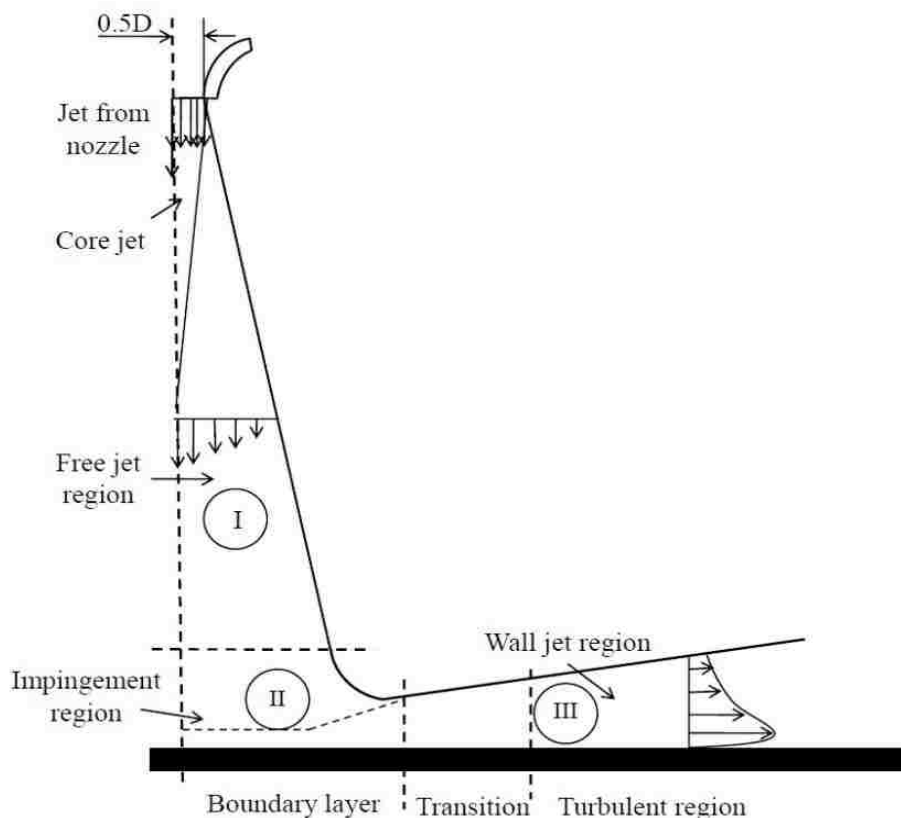
Fig. 2.1 Definition schematic of an impinging circular jet with large height-to-diameter ratio (adapted from Rajaratnam et al. (2010))

Numerical simulation of a round jet impinging on a flat surface using Reynolds-Averaged Navier-Stokes (RANS) turbulence models have been the subject of considerable research, forming part of the 2nd ERCOFTAC-IAHR Workshop on Refined Flow Modelling in 1993. Subsequently, Craft et al. (1993) published their research using different turbulence models to analyze the heat transfer in the impingement region of the jet, i.e., region II. They observed that the results were not in good agreement with experimental data and attributed this to the weakness associated with the eddy viscosity stress-strain relationship in the turbulence models used. They also implemented second-moment closure models. Due to the incorrect response of the wall reflection process, the eddy viscosity model (k - ε) and the basic Reynolds Stress Model (RSM) failed to produce reasonable results. However, an improved RSM which takes into account the wall reflection effects generated satisfactory results.

Most of the previous analyses of impinging jets deal with a specific nozzle stand-off distance. As mentioned earlier, the experiments by Giralt et al. (1977) were carried out to study the effect of stand-off distance, but the evaluation is limited to the quantities inside the jet, the variation of turbulence intensity along the jet axis and presentation of a numerical model for determining the wall shear stress. There is a lack of information regarding the effect of impingement distance on the mean and turbulence quantities in different regions of the impinging jet, including the free jet portion, impinging zone and the wall jet region. The focus of the current study is to investigate the mean and turbulence characteristics in all three regions of the impinging jet flow for different H/D

values. In addition, it is also of practical interest to evaluate the mean and turbulence quantities in regions very close to the wall because of the uncertainties associated with the experimental techniques in this region.

In this chapter, three-dimensional RANS simulations have been carried out for H/D = 2, 6 and 18.5 at Re = 100,000. H/D = 2 represents a jet with impingement occurring in the potential core region. Jets with H/D = 6 are in a transitional state and the core of the jet is almost fully penetrated by the external flow. At H/D = 18.5, the jet can be considered as fully developed with distinct regions of flow including potential core, free jet and impingement zone. The experiments performed by Rajaratnam et al. (2010) have been used as the primary benchmark to validate the numerical model. However, other experimental data from Bradshaw and Love (1961) and Giralt et al. (1977) are also used to assess the accuracy of the computational results.

2.2. Numerical method

2.2.1. Geometry modelling and boundary conditions

In this research, a high velocity air jet exiting from a circular nozzle impinges vertically on a flat plate and spreads out as a radial wall jet. The nozzle has an exit diameter of D = 23.4 mm. The stand-off distances between the nozzle exit plane and the plate are H = 46.8 mm (H/D = 2), 140.4 mm (H/D = 6) and 432 mm (H/D = 18.5). The value H/D = 18.5 is specifically chosen to match the experimental conditions used by Rajaratnam et al. (2010). The inflow direction is

normal to the plate. Details of the computational domain and mesh generated for the current simulations are shown in Fig. 2.2.
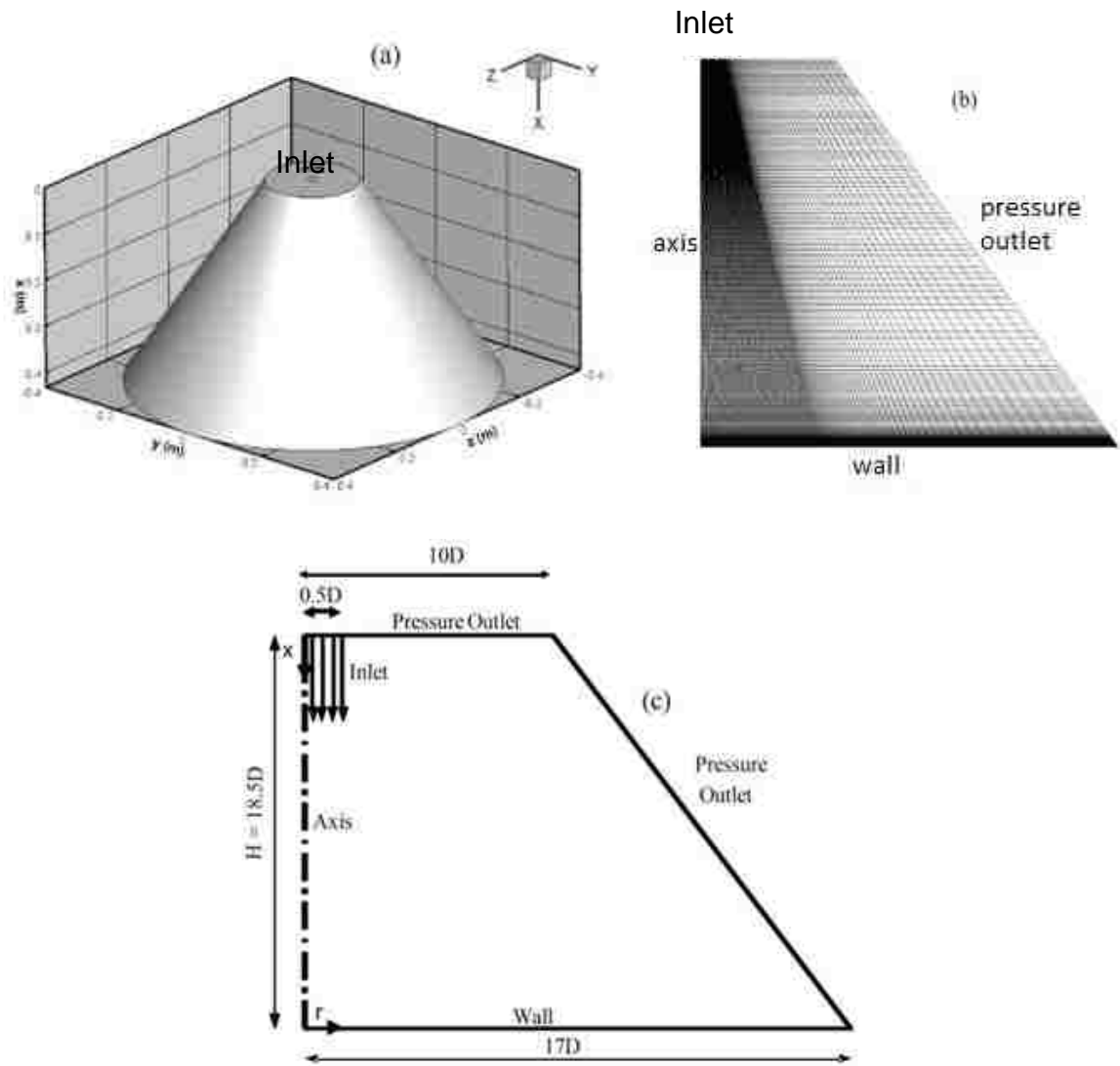
Fig. 2.2 (a) Full 3D geometry, (b) cross-section of the computational domain and mesh, and (c) domain dimensions and boundary conditions

The full 3D geometry for the H/D = 18.5 case is illustrated in Fig. 2.2a and the structured mesh system and half cross-section of the domain with the boundary

conditions applied in the numerical model are shown in Figs. 2.2b and 2.2c, respectively. In Fig. 2.2c, the jet is aligned with the x-axis and r is the radial distance from the x-axis. To ensure that the location of the outlet boundary has negligible influence on the pressure and velocity fields, the computational domain is taken to have a radius of 0.4 m (17D) along the plate. Shorter distances between the pressure outlet boundary and the jet axis were taken for the H/D = 2 and 6 cases, but sufficiently long enough to minimize the influence of this boundary on the flow field.

A constant velocity of 61m/s is imposed at the inlet, corresponding to a Reynolds number of 100,000 based on the nozzle exit velocity and diameter. Since the air escapes to the atmosphere through the side and top boundaries of the computational domain, they are set as pressure outlets. The plate is considered to be a no-slip boundary. The Low Reynolds Number Modelling (LRNM) method (Launder and Spalding, 1974) is used as a numerical model to accurately capture the wall effect.

In order to provide a fine mesh with minimal skewness in the boundary layer near the impinging wall, the mesh system is constructed of hexahedral elements. A high-density mesh, as shown in Fig. 2.2b, is used to capture the high shear stresses within the jet, as well as those generated near the plate, particularly in the impingement zone. For the rest of the domain, where the wall effect is smaller, a coarser mesh is used. Different mesh schemes, including fully structured, fully unstructured and hybrid meshes with different numbers of cells were tested. Finally, based on comparison of the simulated and experimental

results, the fully structured mesh was chosen for all subsequent simulations. Grid independence tests were also performed, the grid size being increased in 20% increments until no noticeable variance in the drag force exerted on the plate was observed. The total number of cells required to ensure a grid independent solution from the current simulations was approximately 1.1 x 10^6 for H/D = 2, 1.38 x 10^6 for H/D = 6 and 1.84 x 10^6 for H/D = 18.5.

2.2.2. Governing equations

The impinging jet flow is modeled by the steady 3D incompressible RANS equations, representing conservation of mass and momentum balance. These equations, in tensor form, are:

$$\frac{\partial \bar{u}_i}{\partial x_j} = 0 \tag{2.1}$$

$$\frac{\partial}{\partial x_j}\left(\bar{u}_i \bar{u}_j\right) = \frac{\partial}{\partial x_j}\left[\nu\left(\frac{\partial \bar{u}_i}{\partial x_j} + \frac{\partial \bar{u}_j}{\partial x_i}\right)\right] - \frac{1}{\rho}\frac{\partial \bar{p}}{\partial x_i} - \frac{\partial \overline{u_i u_j}}{\partial x_j} \tag{2.2}$$

where x_i, u_i, u_i', p, ρ and ν denote the coordinate directions, velocity, the velocity fluctuations, pressure, density and kinematic viscosity, respectively, and the over-bar indicates a time-averaged quantity (Hoffmann and Chiang, 2000).

Cooper et al. (1993) has reported that for the simulation of impinging jets, the k - ε model over-predicts the turbulent kinetic energy near the stagnation point. In order to reduce this effect, different turbulence models, which take into account the non-isotropic nature of the turbulent viscosity, have been considered.

The Realizable k – ε model (Shih et al. 1995), the k - ω SST (Shear Stress Transport) model (Menter, 1994) and the Reynolds Stress Model (RSM) (Launder et al. 1975) have been implemented in the current simulations. For the Realizable k - ε model, the LRNM is used.The k - ω SST turbulence model takes into account the low-Re effects in the flow. In the SST version of the model, the standard k – ω model is used for the near-wall region, combined with a standard k – ε model in the fully turbulent zone (Menter, 1994). The Reynolds Stress Model (RSM), which is also used in this study, takes into consideration multi-scale and anisotropic effects of turbulence. In RSM, a transport equation is solved for each of the unknown stresses in the Reynolds stress tensor. A wall reflection scheme and pressure gradient terms are included in the model (Launder et al.1975). The details of these models can be found in FLUENT 6.3.26 User's Guide.

The finite volume method is used to discretize the governing equations, with the QUICK scheme for discretization of the convective terms. The Standard scheme for the pressure interpolation is used. For the pressure-velocity coupling, the SIMPLE algorithm developed by Patankar and Spalding (1972) has been applied. FLUENT 6.3.26 is used to solve the discretized governing equations. During the simulations the drag force exerted on the plate was monitored, and the solution was considered converged when no significant change in drag was observed (changes less than the order of 10^{-3}). For all results presented in this chapter, the residuals of the continuity, momentum and turbulence equations are all of the order of 10^{-4} or less.

2.3. Results

To understand the effect of the nozzle height on the behaviour of impinging jets, different mean and turbulent flow parameters have been analyzed at various H/D ratios. These quantities include the decay of centreline velocity, radial distribution of axial velocity, pressure and shear stress distribution along the plate, and mean and root mean square (rms) velocities in the wall jet region.

2.3.1. Centreline velocity

To validate the current CFD simulations, the results are compared with the available experimental data of Giralt et al. (1977) and Rajaratnam et al. (2010). Although there are three distinct cases in the current simulations (H/D = 2, 6 and 18.5), for the purpose of identifying the best RANS turbulence model to use for subsequent analysis, only the H/D =18.5 case was selected for a detailed comparison. According to the results shown in Fig. 2.3, the Realizable k - ε and RSM models show some over-prediction of the centreline velocity entering the impingement zone, but recover to provide a close match to the data of Rajaratnam et al. (2010) near the plate surface. On the other hand, the k - ω SST model provides a good agreement with the data of Rajaratnam et al. (2010) through the impingement zone and very close to the plate. Note that k - ω SST activates the k - ε model in regions where there is no wall effect.
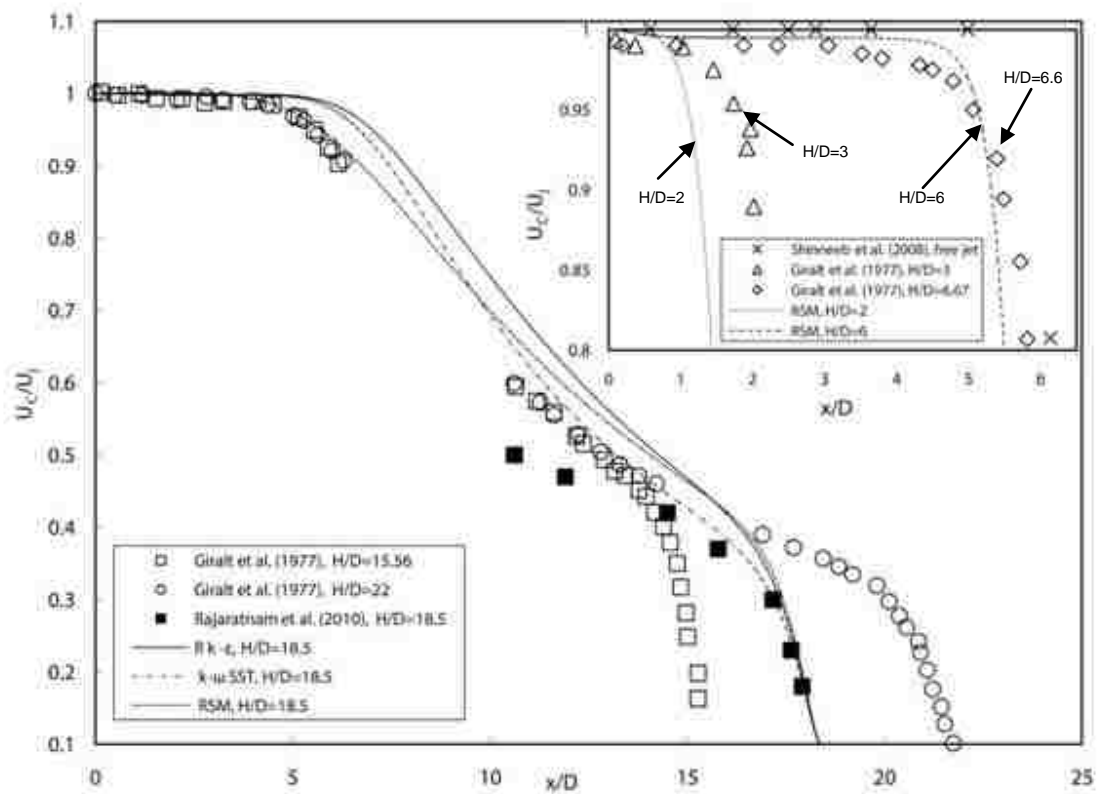
Fig. 2.3 Comparison between computational and experimental centreline velocity

All three models show good agreement with the H/D = 18.5 experimental data of Rajaratnam et al. (2010) as the flow approaches the plate (region II), but Fig. 2.3 also shows that RSM yields more accurate centreline velocity in the free jet (region I). Based on this comparison, and also considering that RSM is a non-isotropic turbulence model, the RSM was selected as the main turbulence model for further simulations in all H/D cases. The following sections investigate the variation of the centreline velocity as the H/D ratio increases from 2 to 18.5.

2.3.1.1. H/D = 2

The case of H/D < 6 represents an impinging jet where the core of the jet reaches the plate and has not yet been fully penetrated by the ambient flow. No fully developed free jet region exists for this type of impinging jet and different regimes of the jet are not distinguishable. To obtain a better understanding of this kind of impinging jet, H/D = 2 was chosen for the current CFD study and the results are compared with the available experimental data of Giralt et al. (1977) at H/D = 3 (see inset in Fig. 2.3). This comparison confirms that the current results follow the expected trend. For H/D = 2, no significant decay in the centreline velocity between the nozzle and the plate is observed, except in the impinging zone which starts around x/D = 1 and extends to the stagnation point.

2.3.1.2. H/D = 6

As previously discussed, H/D = 6 represents an intermediate regime of an impinging jet in which the core of the jet has reached the maximum penetration (Beltaos and Rajaratnam, 1977). Therefore, the current CFD analysis was carried out at H/D = 6 and the results are compared with the experimental data of Giralt et al. (1977) at H/D = 6.67 and the free jet results of Shinneeb et al. (2008) (see inset in Fig. 2.3). Similar to H/D = 2, at H/D = 6 no decay in the centreline velocity is observed up to the impinging zone (i.e., 0 <x/D < 5), which confirms that the core of the jet is still developing up to a location very close to the plate. Comparing the results with a free jet (Shinneeb et al. 2008), it is clear that the jet

27

is influenced by the impingement wallfor x/D > 5. Results for the radial distribution of the axial velocity are discussed in Section 2.3.2.

2.3.1.3. H/D = 18.5

According to the literature discussed above and also based on the results shown in Fig. 2.3, H/D = 18.5 represents an impinging jet in which all three sub-regions of an impinging jet co-exist, namely the free jet region, impingement zone and wall jet region. Figure 2.3 shows that for H/D = 18.5, the core of the jet is still developing up to about x/D = 6and no decay in the centreline velocity can be observed. For x/D > 6, the free jet region starts to develop and a large decay in centreline velocity occurs up to about x/D = 15 as the ambient flow is entrained with the jet. For x/D > 15, the flow senses the plate and a much sharper decay in the centreline velocity can be seen compared to the decay in the region 6 < x/D < 15. This is due to the transfer of the momentum from the axial to the radial direction.

One can note from Fig. 2.3 that the results of Rajaratnam et al. (2010) deviate significantly from the results of the present simulations and the experimental results of Giralt et al. (1977) for x/D < 14. It is important to recall that the design of the nozzle has an impact on the downstream evolution of the jet (Xu and Antonia, 2002). The shape of the nozzle affects the behaviour of the shear layer at the jet exit, influencing flow characteristics such as jet expansion in the radial direction, jet development and most importantly the interaction with the

impingement zone. This could be the reason for this discrepancy. Nevertheless, for x/D > 17, where the flow approaches the impingement point, the mean values of the streamwisecentreline velocity obtained from the CFD calculations (H/D = 18.5) match very well with the measurements of Rajaratnam et al. (2010), and fall between the results of Giralt et al. (1977) corresponding to H/D = 15.6 and H/D = 22.

2.3.2. Radial distribution of velocity

Figure 2.4 illustrates the effect of H/D on the radial distribution of the streamwise mean velocity, normalized by the local maximum value U_m, for locations near the impingement plate (0.785 < x/H < 0.99). The radial distance is normalized by the jet half-width δ_1, defined as the radial location where $U = 0.5U_m$.

For H/D = 2, Fig. 2.4a shows that there is a slight shift in the peak of the streamwise velocity profiles towards the axis when moving from x/H = 0.785 to 0.93. This phenomenon confirms that the flow is still accelerating and results in a transfer of momentum from the axial to radial direction in the region 0.785 < x/H <0.93. For the rest of the axial stations x/H = 0.97, 0.98 and 0.99, the streamwise velocity profiles collapse on each other.

In Fig. 2.4b the streamwise velocity profiles at several axial stations are plotted for H/D = 6. The flat shape of the profile (no decay in the centreline velocity) at the x/H = 0.785 station shows that the core of the jet (with some

minor losses) has retained its top-hat shape up to this station. The peak observed in the other profiles is located off the centreline, which confirms that the flow has started to change direction from axial to radial. Comparison of the jet diameter at similar axial stations for H/D = 2 and H/D = 6 (Figs. 2.4a and 2.4b) shows a decrease in this value as the H/D ratio increases.

The velocity profiles at stations very close to the plate (x/H = 0.98 and 0.99) bring out another important difference between the H/D = 2 and 6 cases. Note that due to limitations in experimental techniques, measurements in regions very close to the plate are susceptible to large uncertainties. Figure 2.4a illustrates that there is a collapse in the velocity profiles at these stations for H/D = 2, which suggests that the flow has changed direction before these stations. However, for the same stations with H/D = 6, some changes in the peak of the profiles can be observed in Fig. 2.4b, indicating that momentum transfer occurs from the axial to the radial direction even at these stations very close to the plate. Figure 2.4c shows that the velocity profiles at all x/H stations have the same peak region along the centreline. This implies that the core of the jet is not developing anymore and the flow has reached an almost fully developed condition. The simulation results presented in Fig. 2.4c are consistent with the classification of impinging jets based on the H/D ratio presented by Beltaos and Rajaratnam (1974, 1977).
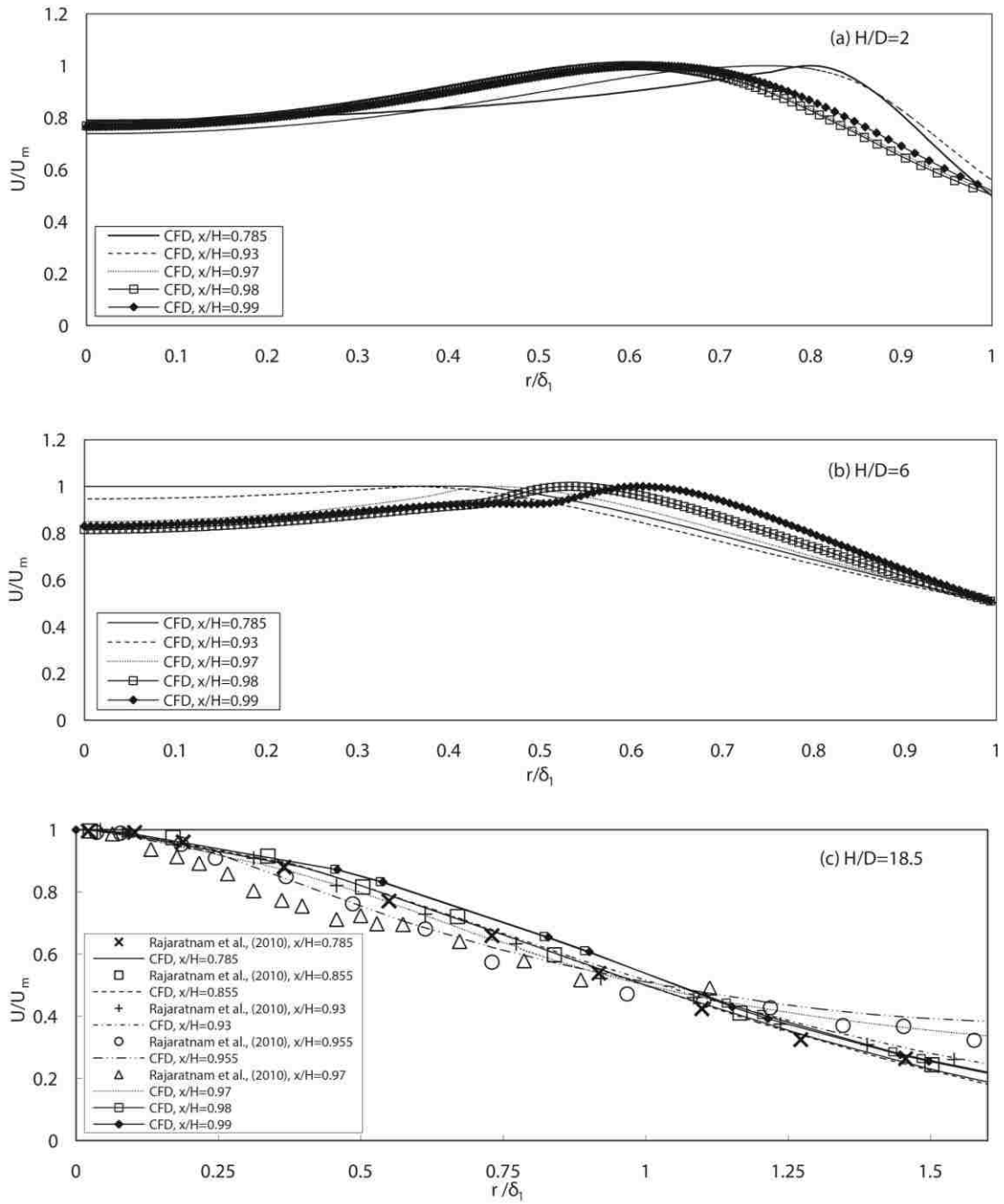
Fig. 2.4 Mean velocity distribution at different x/H stations, comparing experimental data and CFD results; (a) H/D = 2, (b) H/D = 6, (c) H/D = 18.5

2.3.3. Radial distribution of shear stress

2.3.3.1. Shear stress in regions I, II and III

Figure 2.5 shows the comparison between radial distribution of shear stress for three H/D ratios. The results show that there is a local maximum and minimum in the radial distribution of the shear stress (Figs. 2.5a, 2.5c and 2.5e). The first peak (maximum) occurs due to the entrainment of the ambient air into the exiting flow from the nozzle. As the flow expands in the radial direction the peak loses its magnitude. The second peak (minimum) is located in the region very close to the wall. It can be seen that as the flow gets closer to the wall the magnitude of the peak shear stress starts to increase, and at a specific station it starts to exhibit a decreasing behaviour. A good representation of this phenomenon can be seen in the inset (Figs. 2.5b, 2.5d, 2.5f) where the contours of $\overline{uv}/U_j^2$ in the impingement zone of the computational domain have been illustrated. In this figure, the positive peak shear stress is observed at x/H stations between the nozzle and the impingement zone. In the region where the flow changes direction from axial to radial, both positive and negative values of shear stress can be seen, and for the region very close to the plate, only the negative values of shear stress remain. Comparison of the shear stress profiles at different H/D shows that the magnitude of the peak value of the shear stress in the region close to the wall (x/H = 0.97 ~ 0.98) increases when H/D increases from 2 to 6 and then changes to a decreasing trend for H/D from 6 to 18.5.
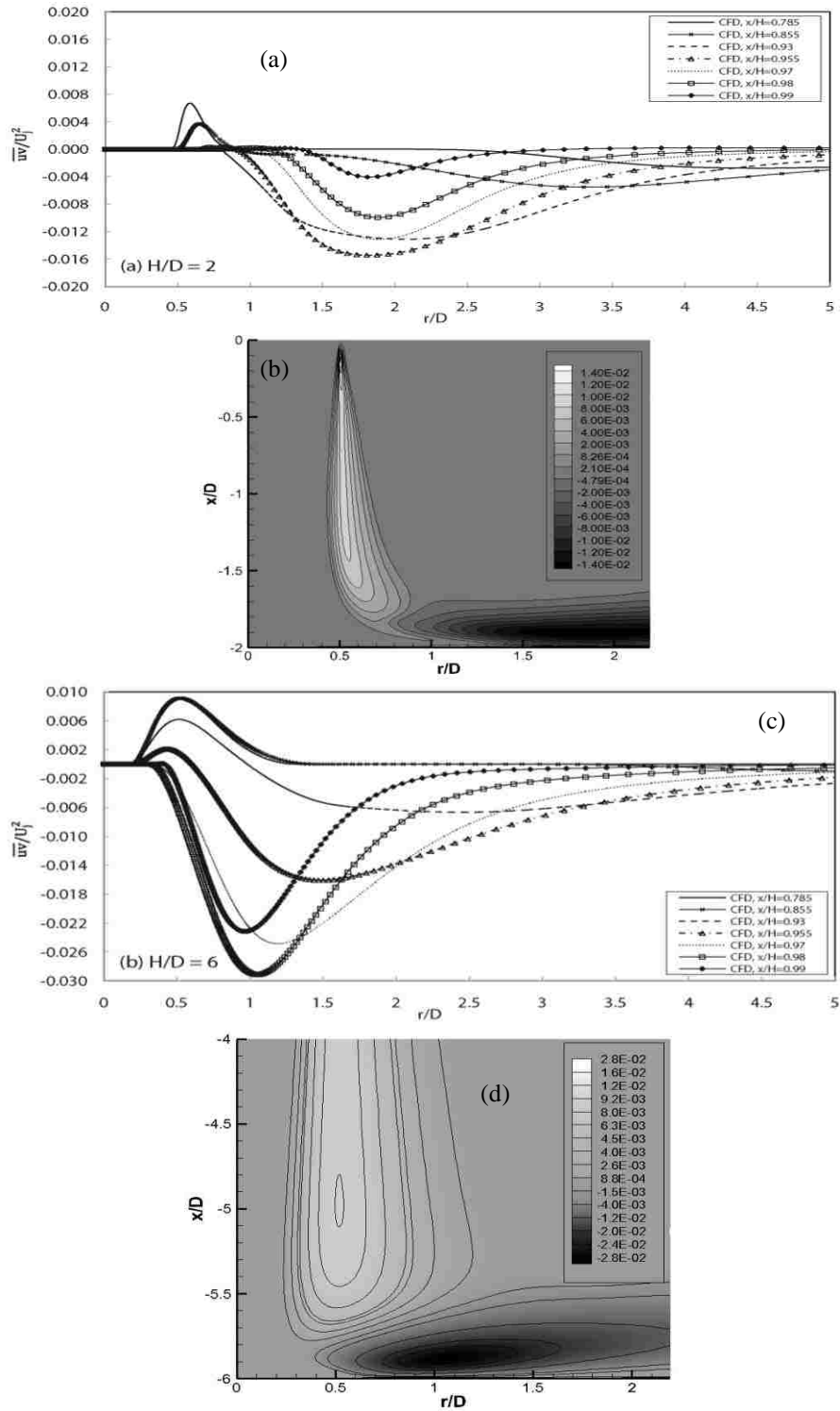
Fig. 2.5 Comparison of experiments and CFD for the shear stress profiles $\overline{uv}/U_j^2$

at different x/H stations and H/D ratios (continued)
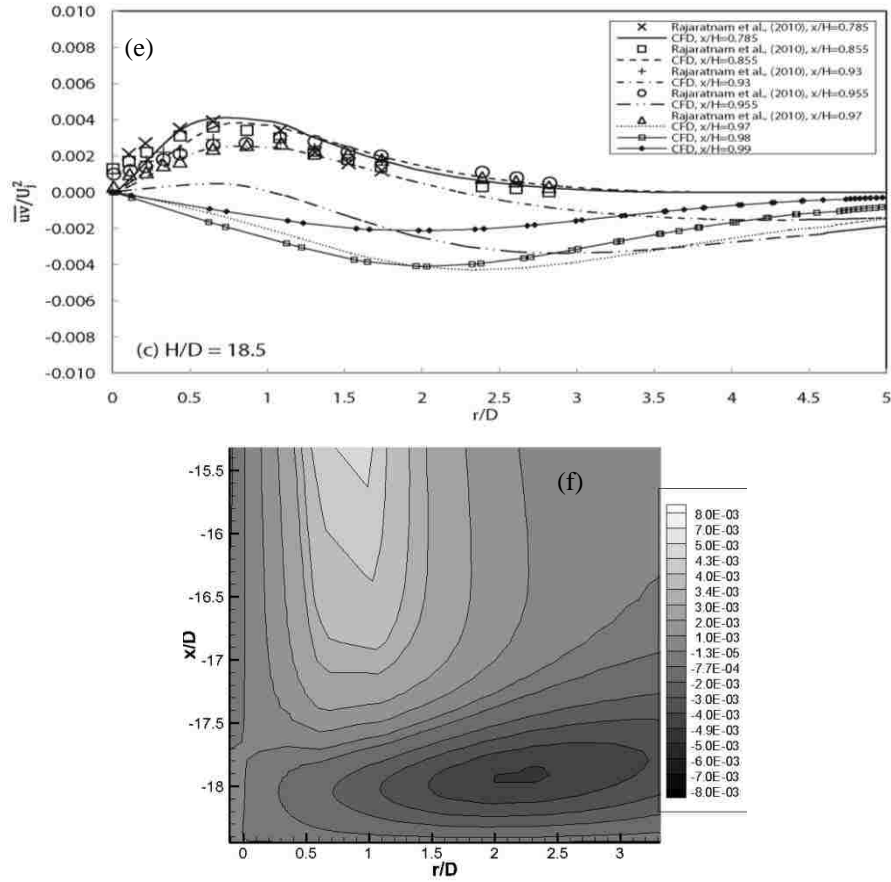
Fig. 2.5 (continued) Comparison of experiments and CFD for the shear stress profiles $\overline{uv}/U_j^2$ at different x/H stations and H/D ratios

Figure 2.5e compares the predicted shear stress with those of Rajaratnam et al. (2010) at H/D = 18.5. At most x/H stations, except very close to the plate at x/H = 0.955 and 0.97, the CFD results match well with the experiments. Measurements at locations very close to the wall are associated with higher uncertainties. The well-known difficulties of experimental techniques in accurately capturing the large variation of shear stress in regions very close to the wall (x/H = 0.97 ~ 0.99) further support the contributions of CFD analysis in these regions.

2.3.3.2. Wall shear stress

Figure 2.6 displays the wall shear stress distribution from the current simulations and the impinging jet measurements carried out by Alekseenko and Markovich (1994) at Re = 41,600 and H/D = 2. Also shown are the experimental results of Bradshaw and Love (1961) at Re = 150,000 and H/D = 18. In this figure, the radial direction is non-dimensionalized by the jet height, while the shear stress is normalized by ρU_j^2. The quantity plotted along the vertical axis is chosen to be consistent with other studies.

According to this figure, the peak wall shear stress is increased when the distance between the nozzle and the plate is increased, which is similar to the trend predicted by the numerical model of Giralt et al. (1977). As noted by Giraltet al. (1977) for small nozzle heights, the jet entering the impingement zone has a uniform velocity profile, causing lower flow acceleration near the stagnation point and therefore smaller shear stress values. By increasing the H/D ratio, the peak of the velocity profile shifts towards the centreline, resulting in maximum flow acceleration in the region close to the axis.
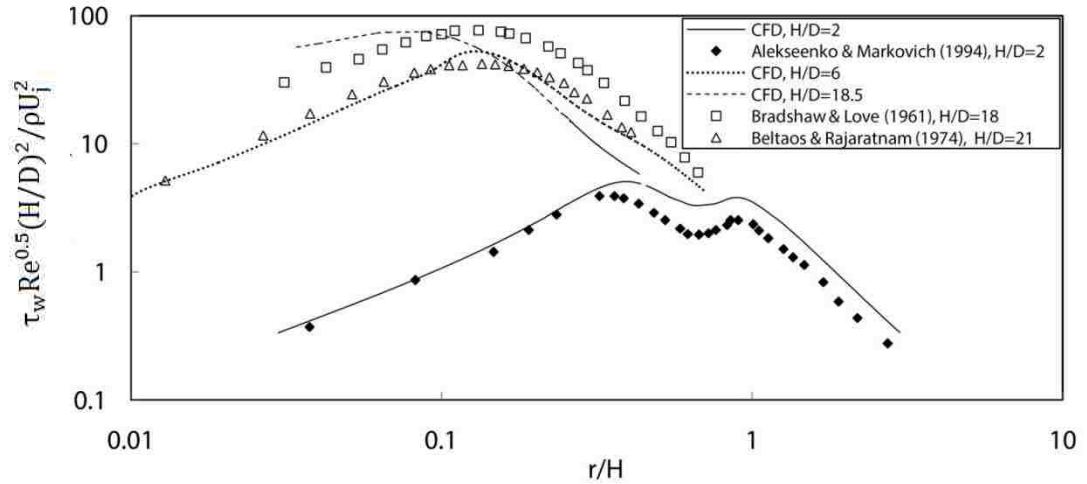
Fig. 2.6 Wall shear stress along the impingement plate

Both the experimental results and the present simulations indicate the presence of two peaks in the wall shear stress distribution when H/D = 2. With increasing H/D, a single peak is located closer to the jet axis. Kataoka and Mizushina (1974) and Alekseenko and Markovich (1994) noticed that for small H/D values the transition from a laminar to turbulent boundary layer within the impingement zone is accompanied by a sudden increase in the wall shear stress. Consistent with their experiments, this phenomenon can be observed for H/D = 2 in Fig. 2.6, where the wall shear stress experiences a sudden increase near r/H = 1. For small H/D ratios, the transition from laminar to turbulent boundary layer in the wall jet part of the flow occurs slightly later compared to jets with large H/D ratios. This is due to the fact that in small H/D impinging jets, the potential core of the jet reaches the impingement region, whereas for large H/D cases the flow is turbulent when it enters the impingement zone.

2.3.4. Static pressure along the plate

Figure 2.7 compares the static pressure distribution along the plate for different stand-off distances. The static pressure values are normalized by the static pressure at the stagnation point, P_s. The radial direction is normalized by $r_{1/2}$, which is the radial position at which $P = 0.5P_s$. The numerical predictions obtained at all H/D ratios are consistent with the measurements by Bradshaw and Love (1961) and by Giralt et al. (1977) at large H/D.
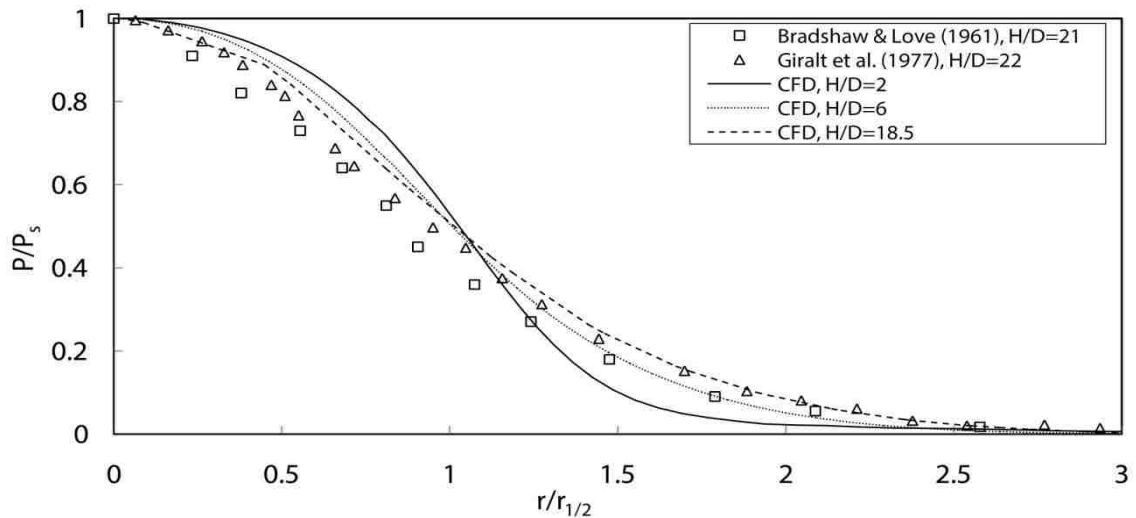
Fig. 2.7 Static pressure along the impingement plate

For small stand-off distance (H/D = 2), the initial shape of the velocity profile is nearly uniform, as illustrated in Fig. 2.3 (inset) and Fig. 2.4a. Therefore, the pressure distribution in this case is wide and the region where higher pressure exists is larger. As the value of H/D increases, the jet velocity profile loses its uniform behaviour and the momentum is higher in regions close to the

centreline. This trend continues as the H/D ratio increases up to 18.5, for which a fully penetrated jet exists. At this ratio, a more gradual radial decay in the pressure profile is observed, which is in reasonable agreement with the experimental data of Bradshaw and Love (1961) at H/D = 21 and Giralt et al. (1977) at H/D = 22.

2.3.5. Wall jet region

Following impingement, the flow spreads out as a radial wall jet. As the flow moves along the wall, a boundary layer is formed. There are a number of experiments and numerical simulations on wall jet flows. These analyses include either jet flows exiting from a nozzle which is parallel to the plate or from a nozzle perpendicular to the plate. To analyze the results of the current simulations in the wall jet portion of the flow, the experimental data of Bradshaw and Love (1961) for H/D = 18 has been used as a benchmark. The mean values of the normalized radial velocity V/V_m for the three H/D values are plotted as a function of $(H-x)/\delta_2$ in Fig. 2.8, where V_m is the local maximum value of V, (H-x) is the normal distance from the plate and δ_2 is the distance above the plate at which $V = 0.5V_m$. Figure 2.8 shows a comparison between the experimental data of Bradshaw and Love (1961) at H/D = 18 and the numerical results for different H/D ratios at various r/D stations along the plate. This figure indicates that the present numerical simulations generate reasonable results which follow the trend of the experimental data. The results suggest that in regions located in the downstream

portion of the flow along the wall, a fully developed condition can be expected for all H/D values.
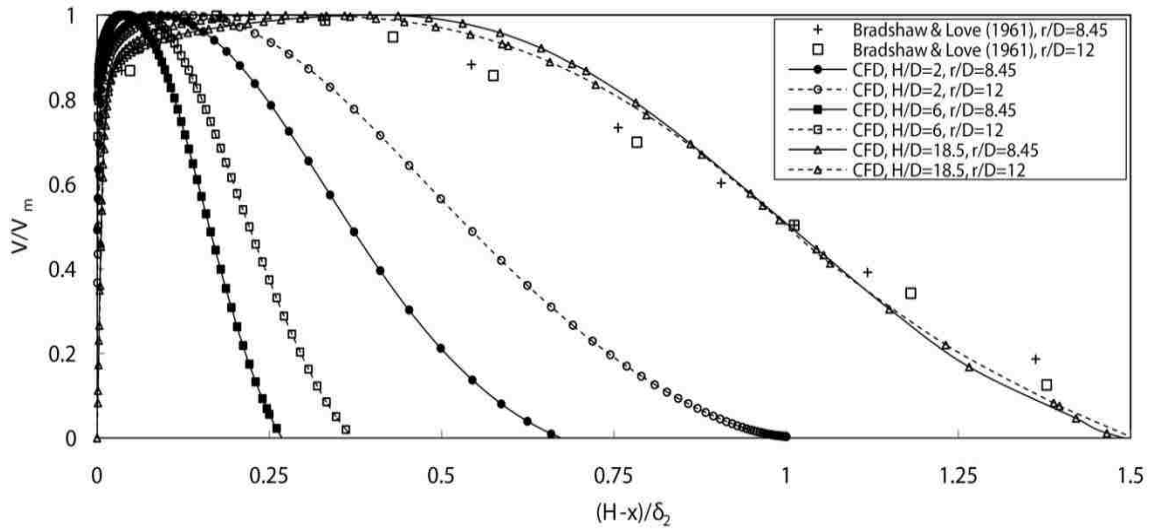
Fig. 2.8 Radial velocity V/V_m at different r/D stations in the wall jet

By comparing the spread between the velocity profiles at the two radial distances (r/D = 8.45 and 12) in all three H/D cases, it can be concluded that the rate of development of the wall boundary layer increases by increasing the H/D ratio. According to Fig. 2.8, a faster boundary layer development can be observed for impinging jets with larger nozzle heights.
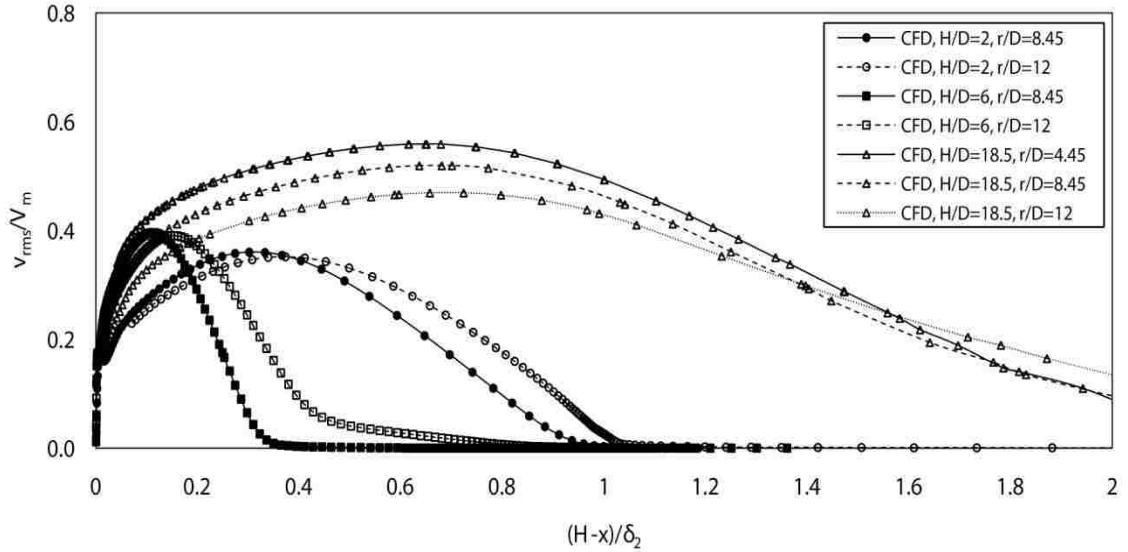
Fig. 2.9 Comparison of v_{rms}/V_m for different nozzle heights, at different r/D stations in the wall jet region (fully developed)

Further analysis has been performed for key turbulence parameters, at different stations along the plate. Figures 2.9 and 2.10 illustrate the root mean square radial velocity v_{rms}/V_m and the Reynolds stress $\overline{uv}/V_m^2$ obtained from the CFD simulations for the three H/D values at different r/D stations along the wall. Both v_{rms}/V_m and $\overline{uv}/V_m^2$ profiles show a decreasing behaviour as the flow travels along the wall towards the downstream. A fully developed condition over the plate can be expected in sections far off the centreline of the impinging jet.

Compared to the mean velocity profile in the wall jet region, a similar behaviour can be seen for the v_{rms}/V_m and $\overline{uv}/V_m^2$ profiles. These figures show that an increase in nozzle height results in faster development for the turbulence

40

quantities. It should be noted that no experimental data are presented in Figs. 2.9 and 2.10 becauseit is not available in the literature.
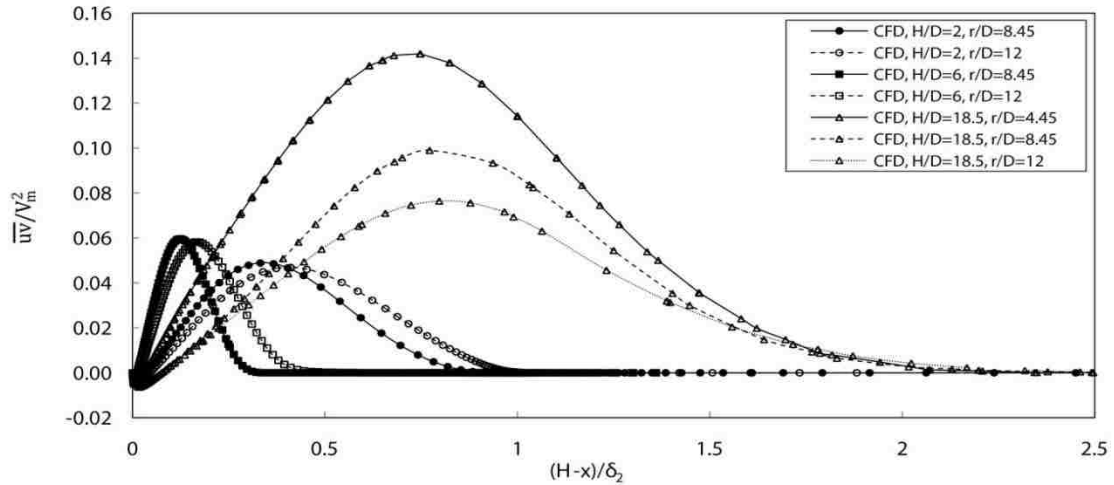
Fig. 2.10 Comparison of $\overline{uv}/V_m^2$ for different nozzle heights, at different r/D stations in the wall jet region (fully developed)

2.3.6. Wall heat transfer

To investigate the dependency of the heat transfer rate from the plate on the nozzle height-to-diameter ratio, the energy equation was activated in the model. A constant temperature of 300°K was considered for the jet exiting from the nozzle. A constant heat flux (q_v = 1000 W/m^2) was applied on the plate, which causes the fluid to be heated during the impingement and also along the wall region. The local convective heat transfer coefficient (h) can be calculated from

$$h = \frac{q_v}{(T_w - T_j)} \tag{2.3}$$

where T_w is the wall temperature and T_j is the jet temperature at the exit of the nozzle. The local Nusselt number, which is representative of the heat transfer ratio, is defined as

$$Nu_D = \frac{hD}{\kappa} \tag{2.4}$$

where κ is the conductive heat transfer coefficient of the fluid. Figure 2.11 illustrates the variation of the local Nusselt number on the plate with different H/D ratios. This figure demonstrates that increase in the H/D ratio causes significant changes in the behaviour of the heat transfer phenomena on the plate. The first feature observed is the change in the number of the peaks with increasing stand-off distance H/D. At H/D = 2 two peaks are found at approximately r/D = 0.8 and 1.7, which is consistent with the observed behaviour of the wall shear stress distribution. The first peak is due to the large flow acceleration after impingement and the second one is due to the transition to the turbulent regime in the wall region, as previously discussed by Colucci and Viskanta (1996).
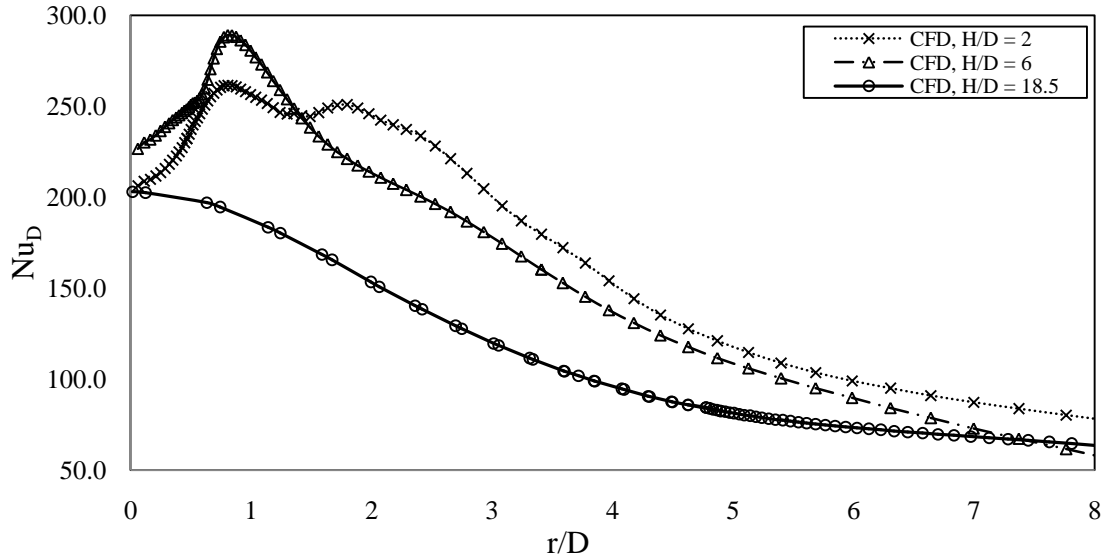
Fig. 2.11 Nusselt number distribution along the plate at different H/D ratios

Increasing H/D to 6.0 changes the trend of the Nusselt number curve. The magnitude of the first peak increases while the second peak disappears. The location of the Nusselt number peak is very similar to the H/D = 2 case and is located around r/D = 0.8. In this case, the trend of the Nusselt number curve is similar to the trend of wall shear stress.

By increasing the H/D value to 18.5, the Nusselt number magnitude decreases in comparison to the two previous cases. The location of the peak value moves towards the centreline. The reason for this behaviour lies in the fact that for impinging jets with large H/D ratios (larger than 6 ~ 8), the jet approaches a fully penetrated condition and the maximum velocity of the jet is located only along the centreline. This is similar to the trend in the data obtained by Colucci and Viskanta (1996) for larger H/D ratio in their experiments.

2.4. Conclusions

Three different nozzle stand-off distances (H/D), representative of the generally accepted classification of impinging jets, were modeled and the results have been compared to available experimental data. The present study adds to the existing state of knowledge by also providing detailed information very close to the impingement plate. Results indicate a strong relationship between the flow behaviour of an impinging jet and the height-to-nozzle diameter ratio. The effect of increasing the nozzle stand-off distance on flow parameters can be summarized as following:

1. Centreline velocity: For H/D = 2 and 6, no decay was observed in the centreline velocity. For H/D = 18.5 no decay was seen up to an axial distance of x/D = 6. A significant reduction occurs for 6 < x/D < 15. For 15 < x/H < 18.5, a larger decay was observed compared to other stations due to the influence of the impingement zone and the transfer of momentum from the axial to the radial direction.

2. Streamwise velocity in different radial distances: The position of the peak in radial distribution of the velocity at similar streamwise directions for different H/D cases moves towards the centreline, leading to reduction in the diameter of the jet.

3. Pressure along the plate: The region of high pressure on the plate is gradually reduced with increasing H/D, primarily due to the change in the shape of the jet profile.

4. Wall shear along the plate: At small H/D values, two peaks of the wall shear can be seen, due to transition from a laminar to turbulent boundary layer. For large H/D, a single peak was observed because the potential core does not reach the plate.

5. Shear stress distribution in the jet: Two peaks of the shear stress exist in the entire flow domain. One is due to the interaction of the exiting flow from the nozzle with the ambient air and the other one is due to the wall effect. When moving in the axial direction towards the wall, the shear stress increases up to a certain station and then decreases.

6. Wall heat transfer: There are two peaks in the Nusselt number curve for small H/D values. As the H/D increases the second peak disappears, following the same trend observed for wall shear stresses. For very large H/D cases, the peak of the Nusselt number curve is reduced and is shifted towards the centreline.

CHAPTER 3

LARGE EDDY SIMULATION OF ROUND IMPINGING JETS WITH LARGE

STAND-OFF DISTANCE

3.1. Introduction

Impinging jets have many practical applications in cooling, heating, metal cutting and industrial cleaning. They include different types of flows such as free jet flow, stagnating flow and a wall jet (see Fig. 1.1). In an impinging jet, flow exiting from the nozzle interacts with the ambient flow and due to the Kelvin-Helmholtz instabilities a street of roll-up vortices is generated. There is a frequency for the generation of these vortices which is dependent on different parameters such as boundary conditions, nozzle geometry and Reynolds number. While traveling towards the plate, these vortices interact, break up, pair and coalesce with neighbouring vortices and their symmetrical shape is lost. This results in an unsteady three-dimensional behaviour for pressure and shear stresses in the impingement zone and a vorticity field in the entire domain. The heat transfer from the plate is also influenced by these unsteady three-dimensional structures approaching the plate.

Chapter 2 provided important mean value results for impinging jets with different H/D ratios. The effect of the H/D ratio on the mean wall shear stress, wall pressure and velocity distribution was investigated. However, since the simulations were based on steady RANS models, no information on unsteady flow phenomena such as vorticity generation and the creation and breakdown of large scale structures was obtained.

In this chapter an unsteady CFD analysis is performed on an impinging jet with large stand-off distance. Firstly, the generation and evolution of the roll-up

vortices, their transition to large scale structures and their influence on different parts of the flow field are investigated to provide a more complete picture of the impinging jet flow, and to develop an understanding of the physics associated with these time-dependent phenomena. Secondly, the unsteady flow characteristics at a large stand-off distance are compared and contrasted with the results at small stand-off cases available in the literature.

To resolve the unsteady flow features at large stand-off distances, it is necessary to develop an appropriate numerical model. As indicated earlier, RANS models have limitations in predicting the flow features, specifically: (i) inaccurate prediction of the stagnation zone flow, (ii) over-prediction of the stagnation point heat transfer, (iii) issues with turbulence modelling in different regions of the flow (Dewan et al. 2012, Zuckerman and Lior, 2005, Shademan et al. 2013). Consequently, Direct Numerical Simulation (DNS) or Large Eddy Simulation (LES) would be more appropriate choices for the unsteady analysis. However, research has shown that in order to resolve all scales of motion in DNS, the number of grid points would have to be of the order of $Re^{9/4}$. This is a limitation that currently makes DNS practical only for low Reynolds number flows as well as for small H/D cases where the physical flow domain is relatively small. For example, Chung et al. (2002) used DNS to simulate an unsteady slot jet with H/D = 10 and Re = 300, 500 and 1,000. Hattori and Nagano (2004) simulated a plane impinging jet using DNS at Re = 9,120 for values of H/D = 0.5, 1 and 2. Both plane and round impinging jets with H/D = 10 were investigated by Tsubokura et al. (2003) using DNS at Re = 2,000 and LES at Re = 6,000.

Recently, Dairay et al. (2015) performed a DNS study on a round impinging jet with H/D = 2 at Re = 10,000 using a total of 952,247,081 cells. As the literature shows, previous DNS studies are associated with either small H/D ratios (H/D < 2) or low Reynolds number flows (Re < 2000), and require a large number of cells, making the simulations too costly for practical use.

In LES only large and high energy containing eddies are resolved and the small ones are modeled. This method demands reasonably fine meshes at higher Reynolds numbers, but it is more flexible compared with DNS and can be a meaningful alternative for industrial applications. Many of the jet studies reported in the literature deal with simple plane jets at low Reynolds numbers. Examples include LES studies on plane impinging jets by Voke and Gao (1998) at Re = 6,500, and by Beaubert and Viazzo (2003) at Re = 3,000 and 7,500. Hadziabdic and Hanjalic (2008) used LES to investigate a circular impinging jet at Re = 20,000 and H/D = 2 and recently Uddin et al. (2013) performed LES on impinging jets at Reynolds numbers of 13,000 and 23,000 at H/D = 2. The literature shows that most of the LES jet studies only cover small stand-off distances with high Reynolds number or large stand-off cases with small Reynolds number.

In the current research, LES is used to investigate the unsteady flow characteristics of an impinging jet with a large stand-off distance at a high Reynolds number. These flow characteristics resolve questions about how the pressure fluctuations and wall shear distribution vary with time; how much the jet axis meanders around the centre in the impingement region; how the fluid

structure changes as the flow moves from the nozzle towards the plate; and how the separation and reattachment occur in the impinging zone and influence the wall shear stress.

In this chapter, Large Eddy Simulation was performed for an impinging jet with height-to-diameter ratio H/D = 20 at the Reynolds number of 28,000 (based on the velocity at the nozzle exit (U_j) and jet diameter (D)). This simulation was designed to mimic the experimental setup at the Hydraulic Engineering Laboratory at the University of Windsor (Roussinova and Balachandar, 2012). The benchmarking experiments were conducted in a water jet facility using a round nozzle with an exit diameter D = 0.01 m and a distance of H = 0.2 m between the plate and the nozzle. The rectangular tank was 2 m long, 1 m wide and 0.7 m deep as illustrated in Fig 3.1. The nozzle and the flow conditioning system have been described in detail in free jet studies using particle image velocimetry (PIV) by Tandalam et al. (2010) and Tian et al. (2012). These experiments as well as the results presented in the literature by other investigators have been used for the purpose of validating the current simulations.
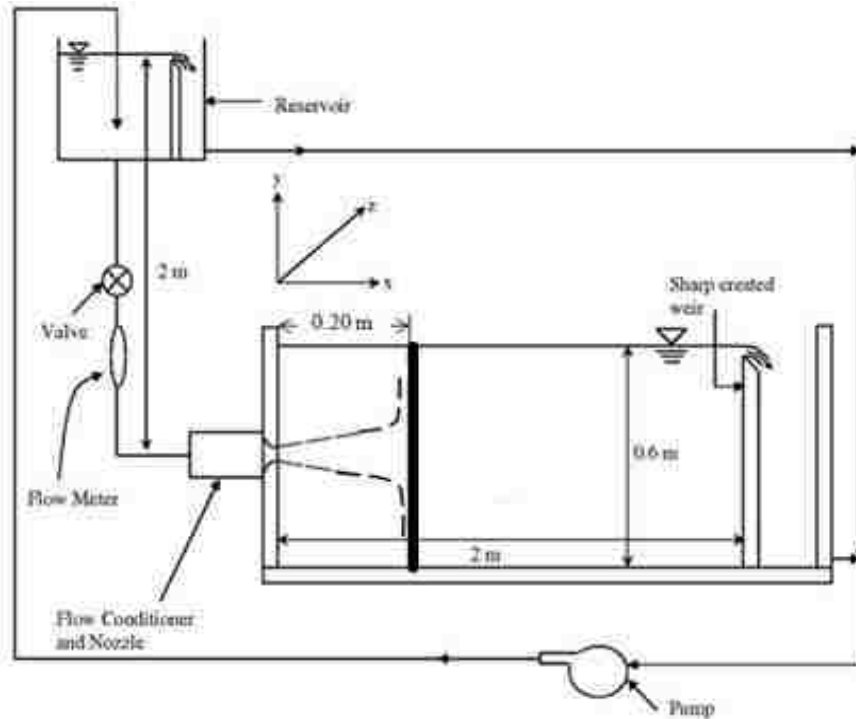
Fig. 3.1 Impinging jet experimental setup (Roussinova and Balachandar, 2012)

3.2. Numerical method

3.2.1. Geometry and boundary conditions

In the experimental studies of Tandalam et al. (2010) and Tian et al. (2012), the flow first passed through a well-designed nozzle (Yu et al. 2012) prior to entering the jet tank. To maintain consistency with the experimental setup, the flow through the nozzle used in these studies has been modelled. In the second step, the jet flow in the tank was simulated. The flow parameters extracted from the nozzle exit were set as the inlet conditions for the tank simulation. The following sections describe the modelling of the flow through the nozzle and the tank.

3.2.1.1. Nozzle flow modelling

A hybrid mesh combining a structured mesh in the wall region and an unstructured mesh in the rest of the nozzle is used. A total of 3.3 million cells were created for the entire nozzle geometry. A cross-section of the mesh is presented in Fig. 3.2. A mass flow rate of 0.35 kg/s is used at the inlet to the nozzle, resulting in a velocity of 2.86 m/s at the exit of the nozzle. A pressure outlet condition is applied for the outlet and a no-slip no-penetration condition is set for the walls.
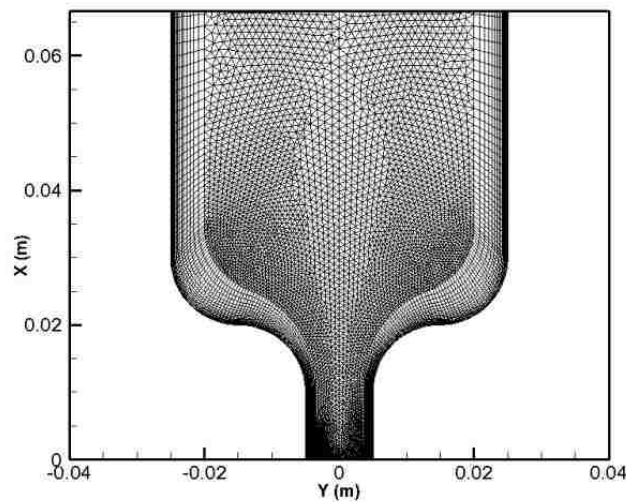
Fig. 3.2 Cross-section of the mesh in the nozzle

A finite volume RANS simulation using the Reynolds Stress Model (RSM) was performed for the flow through the nozzle. The RSM was selected because, as a non-isotropic model, it has the capability of predicting the turbulence quantities in different directions, i.e., the Reynolds stresses $\overline{uu}$, $\overline{vv}$, $\overline{ww}$, $-\overline{uv}$, $-\overline{uw}$ and $-\overline{vw}$, where $\overline{uu}$, $\overline{vv}$ and $\overline{ww}$ are normal stresses in x, y and z directions,

and the rest are shear stresses in x-y, x-z and y-z planes, respectively. The simulation was considered to have converged when no significant change in the drag force exerted on the nozzle was observed. Following this, the profiles of turbulence components and the mean velocity were extracted from the exit of the nozzle and introduced as inlet conditions for the next stage of the simulation. Ansys Fluent 14.0 has been used for performing the simulations.

3.2.1.2. Tank flow modelling

The dimensions of the computational domain for the tank were chosen to simulate the experimental setup described in section 3.1. To simplify the meshing and reduce the computational cost, the large rectangular tank was replaced by a large circular cylinder with its axis perpendicular to the nozzle outlet plane. To ensure that the location of the outlet boundary has negligible influence on the pressure and velocity fields produced by the impinging jet, the computational domain is taken to have a radius of 0.1 m (Fig. 3.3a). In order to reduce the lateral extent of the computational domain, the water is allowed to escape to the ambient through the outer cylindrical boundary of the computational domain. The plate is considered to be a no-slip boundary. The top plane is considered to be a wall with slip condition.

Three different mesh sizes have been tested, each constructed in such a way that the mesh requirements for LES are satisfied. The three meshes are of a hybrid type with triangular prisms in the region r/D < 0.5, where r is the radial

distance from the jet centreline. For the rest of the domain, hexahedral elements are used. Details of the computational domain and the mesh generated for one of the LES cases are shown in Figs. 3.3a-c. Table 3.1 presents the mesh information for the three cases.
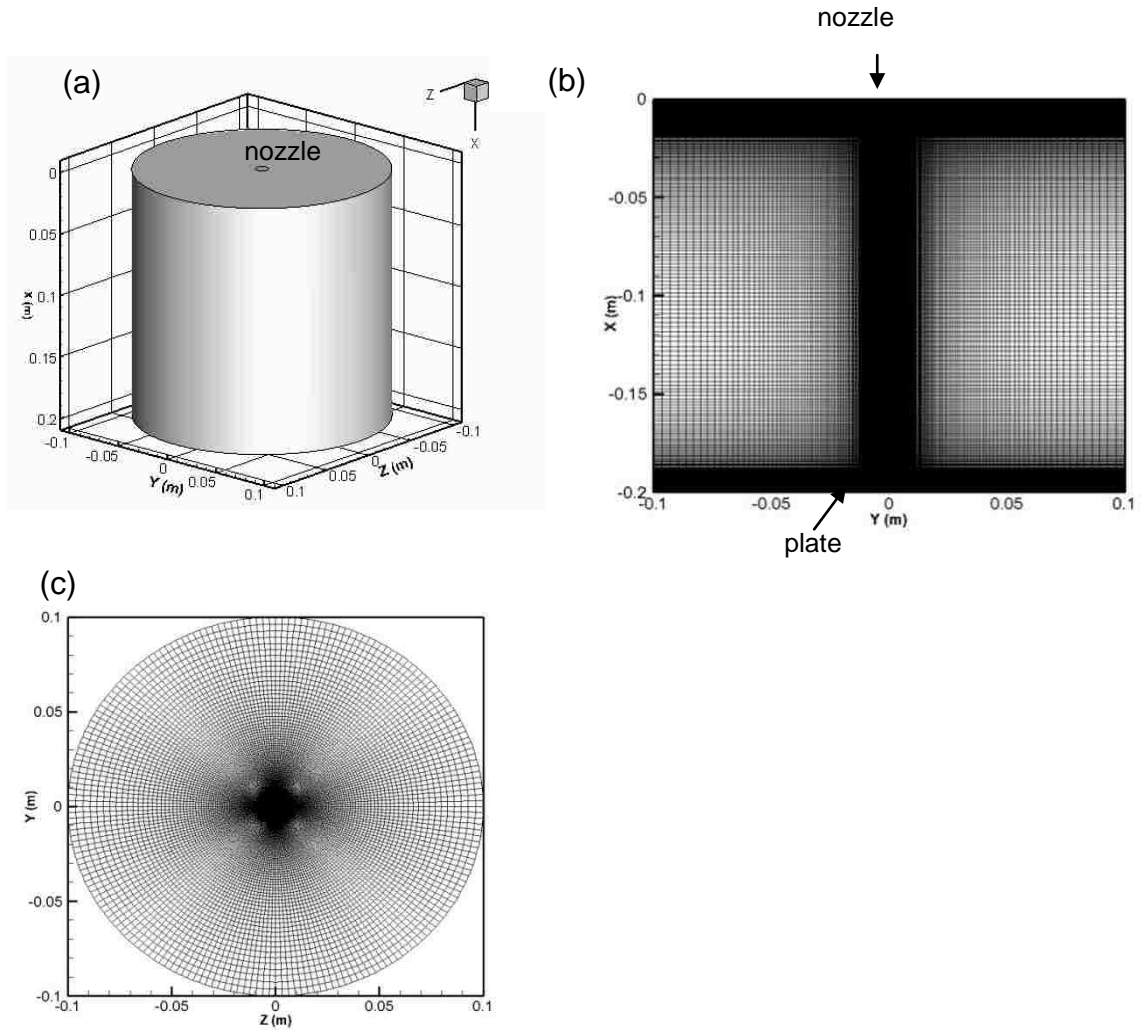
Fig. 3.3(a) Virtual tank dimensions, (b) cross-section of the mesh inside the tank, (c) cross-section of the mesh on the plate

Table 3.1 Grid data (virtual tank)

Mesh	Number of cells in each direction			Total number of cells
	Axial	Radial	Circumferential	
#1	300	150	120	6.3 M
#2	400	150	120	7.6 M
#3	400	150	160	10.6 M

The flow near a wall can be either resolved or modelled in LES, depending on the mesh resolution close to the wall. Since, in the current simulations, the analysis of the impingement zone is of primary interest, more emphasis is placed on the resolution of the mesh close to the target plate. Chapman (1979) determined that the resolution needed for the outer layer of a boundary layer is proportional to $Re^{0.4}$, while for the wall layer the number of grid points required increases to $Re^{1.8}$. The impingement wetted wall surface area increases rapidly with increase in the radial distance from the axis, resulting in a larger domain and consequently a need for more cells. In the area of interest (r/D < 4.0), the mesh resolution should satisfy the generally approved LES criteria for wall-attached flows suggested by Piomelli and Chasnov (1996), which requires that $\Delta r^+ < 100$, $(r\Delta\theta)^+ < 20$ and $\Delta h^+ < 2$ (h is the distance in the normal direction to the wall, θ is circumferential coordinate). Here $\Delta r^+ = \Delta r(u_\tau/\upsilon)$, $(r\Delta\theta)^+ = (r\Delta\theta)(u_\tau/\upsilon)$ and $\Delta h^+ = \Delta h(u_\tau/\upsilon)$, where u_τ is the friction velocity and υ is the kinematic viscosity.

The number of grid points in each direction ineach of the three meshes was increased in a way to evaluate its compliance with the above-mentioned criterion. Figure 3.4a shows that the value of h^+ is less than one for all three meshes for the near-wall cells. Figure 3.3b confirms that increasing the number

of grid points in the axial direction produces smaller Δh^+ values close to the wall and meets the requirements of $\Delta h^+ < 2$. Figures 3.4c and 3.4d show the effect of the mesh density in the near-wall region. To check for the radial direction requirements $(\Delta r^+ < 100,\ (r\Delta\theta)^+ < 20)$ suggested by Piomelli and Chasnov (1996), the values of Δr^+ and $(r\Delta\theta)^+$ for the three meshes are plotted against the radial distance from the axis. Figures 3.4c and 3.4d show that in the region of interest ($r/D < 4$) the values of $(r\Delta\theta)^+$ and Δr^+ for all meshes are less than 5 and 100, respectively. However, some increase in this value can be observed in regions far from the axis ($r/D > 4$), which is inevitable due to the expansion of the mesh in the radial direction. The marginal increase in the value of Δr^+ in the range of $4 < r/D < 10$ might be due to the enhancement of the mesh quality in the axial direction from mesh #1 to #3.
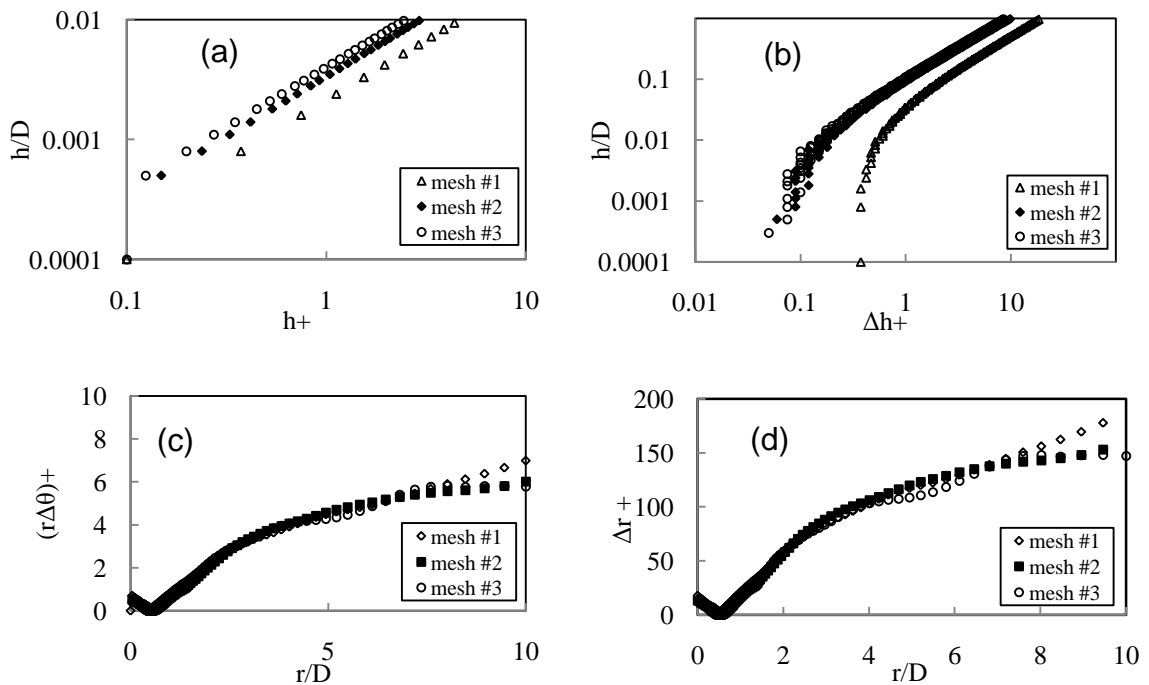
Fig. 3.4 Mesh requirement analysis

Figures 3.4c and 3.4d also show that increase in grid points in the circumferential direction does not have a significant effect on the results close to the wall. Figures 3.4a-d show that all three meshes meet the LES requirements. However, mesh #3 provides values closer to the criterion.

The mesh resolution quality can also be evaluated by comparing the mesh cell size $\Delta = (\Delta r \times r\Delta\theta \times \Delta h)^{1/3}$ to the Kolmogorov length scale $\eta = (\upsilon^3/\varepsilon)^{1/4}$. Here, υ is the molecular viscosity and ε is the dissipation rate. The value of ε can be estimated from the previous RANS simulation using the Realizable k - ε turbulence model. For isotropic turbulence, Pope (2000) has shown that a cell size of 12η or less is required in order to resolve the major contributions to the dissipation. Therefore, in the current study, attempts were made to keep the value of Δ/η value less than 12 in the regions of interest.
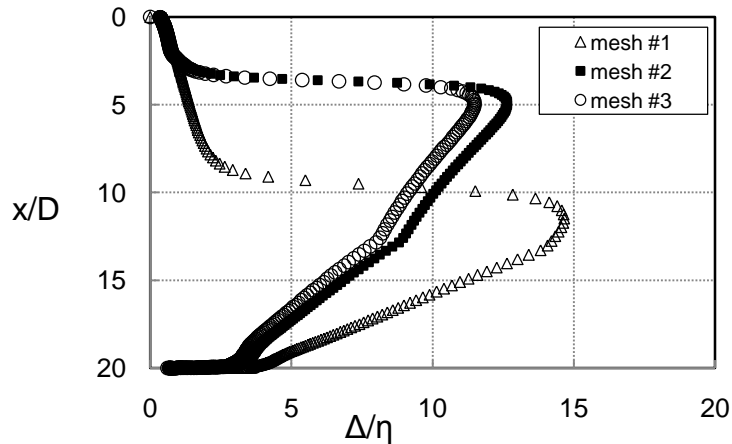
Fig. 3.5 Comparison of mesh cell size with the Kolmogorov length scale at r/D=0

Figure 3.5 compares the mesh cell size with the Kolmogorov length scale. It can be seen that mesh #3 meets the required criteria. Further details on the choice of mesh are provided in section 3.3.

57

3.2.2. Governing equations

The velocity and pressure fields in a Newtonian fluid flow problem are described by the Navier-Stokes equations. The governing equations used in LES are obtained by filtering the unsteady Navier-Stokes equations in Fourier space. The filtered equations are as follows:

$$\frac{\partial \rho}{\partial t} + \frac{\partial}{\partial x_i}(\rho \bar{u}_i) = 0 \tag{3.1}$$

$$\frac{\partial}{\partial t}(\rho \bar{u}_i) + \frac{\partial}{\partial x_j}(\rho \bar{u}_i \bar{u}_j) = \frac{\partial}{\partial x_j}\left(\mu \frac{\partial \sigma_{ij}}{\partial x_j}\right) - \frac{\partial \bar{p}}{\partial x_i} - \frac{\partial \tau_{ij}}{\partial x_j} \tag{3.2}$$

Here, $i = 1, 2, 3$ indicates the spatial direction, p is the pressure, ρ is the density, μ is the dynamic viscosity, $\bar{u}_i$ is the resolved velocity field, σ_{ij} is the shear stress tensor and τ_{ij} is the subgrid-scale (SGS) Reynolds stresses defined by

$$\tau_{ij} = \rho \overline{u_i u_j} - \rho \bar{u}_i \bar{u}_j \ . \tag{3.3}$$

where the overbar indicates a resolved quantity.

The subgrid-scale stresses resulting from the filtering operation are unknown and require modeling. The majority of the subgrid-scale models in use today are eddy viscosity models. These models assume proportionality between the anisotropic part of the SGS stress tensor $\tau_{ij} - (1/3)\delta_{ij}\tau_{kk}$ and the resolved scale strain rate tensor $\bar{S}_{ij}$ as

$$\tau_{ij} - \frac{1}{3}\delta_{ij}\tau_{kk} = -2\mu_t \bar{S}_{ij} \tag{3.4}$$

where μ_t is the subgrid-scale turbulent viscosity, and $\bar{S}_{ij}$ is defined by

$$\overline{S}_{ij} = \frac{1}{2}\left(\frac{\partial \overline{u}_i}{\partial x_j} + \frac{\partial \overline{u}_j}{\partial x_i}\right) .$$ (3.5)

One major drawback of the eddy viscosity subgrid-scale stress models used in LES is their inability to correctly represent the turbulent field in rotating or sheared flows near solid walls with a single universal model constant. The dynamic SGS model resolves this issue. The model coefficient is computed dynamically as the calculation progresses rather than being specified as apriori input. The model is based on an algebraic identity between the subgrid-scale stresses at two different filtered levels and the resolved turbulent stresses. The subgrid-scale stresses obtained using the dynamic model vanish in laminar flow and at a solid boundary, and have the correct asymptotic behaviour in the near-wall region of a turbulent boundary layer. In the current simulations the dynamic Smagorinsky method presented by Germano et al. (1991) is used for the modelling of the subgrid-scale stresses.

The Finite Volume Method (FVM) is used to discretize the governing equations. The second-order accurate central differencing scheme is used for discretizing the convective and diffusive terms. During the simulations, the drag force exerted on the plate is monitored, and the solution is considered to have converged when no significant change in drag was observed (changes less than the order of 10^{-3}). For the results presented herein, all residuals are of the order of 10^{-4}.

3.3. Time averaged results

Validation of the numerical model was carried out by comparing the mean and turbulent quantities at x/D = 1 with the PIV results of Tandalam et al. (2010). Furthermore, the numerical results are also compared in the forthcoming sections with other available experimental results (Shinneeb et al. 2008, Rajaratnam et al. 2010, Giralt et al. 1997).

To evaluate the accuracy of the inlet profiles, mean and turbulent profiles in the jet, obtained from the current LES analysis using the results of mesh #3, were compared with the PIV data close to the nozzle exit, at x/D = 1. As shown in Fig. 3.6, there is good agreement between the results of the LES and the PIV data. Considering the significant influence of the inlet condition on the development of the flow in the domain, the accuracy observed in the mean and turbulent profiles in the vicinity of the nozzle exit provides confidence in the validity of the calculation.
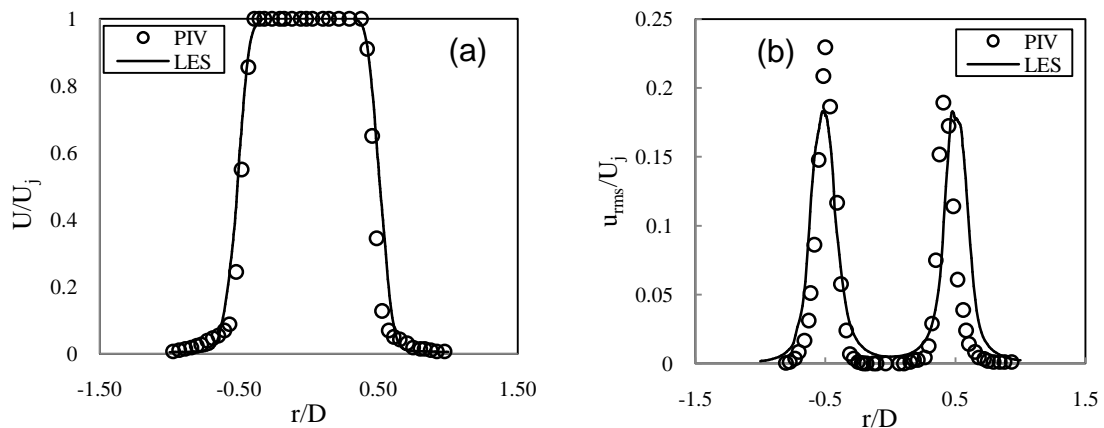
Fig. 3.6 Comparison of (a) mean axial velocity, (b) turbulent axial velocity, obtained from LES and PIV experiments (Tandalam et al. 2010) at x/D = 1

Figure 3.7 shows the normalized mean centreline velocity from the current simulations using the three meshes in comparison with the experimental results for 0< x/D < 25. These results demonstrate the improvement in accuracy achieved by refinement from mesh #1 to mesh #3. Results from the present simulations follow the expected trend observed for different H/D values. Up to about x/D = 15, the flow is not influenced by the impingement wall and essentially follows the behaviour of a free jet. The computational model agrees well with the experimental data as the flow approaches the plate. An impinging jet with H/D = 20 represents a flow with all three sub-regions discussed in Chapter 2. Up to about x/D = 4, the core of the jet is still developing and no decay in the centreline velocity can be observed. For x/D > 4, the free jet region starts to develop and a large decay in centreline velocity occurs up to about x/D = 15 as the ambient fluid is entrained into the jet. For x/D > 15, the flow senses the presence of the plate and a sharper decay in the centreline velocity can be seen due to the transfer of momentum from the axial to the radial direction. Based on the results presented in Fig. 3.7, as well as the mesh requirement analysis presented in the previous section, mesh #3 was selected for all subsequent simulations. Results obtained using mesh #3 compare well with the experiments along the axis and in the impingement zone. Better accuracy can be observed when comparing these LES results with the previous RANS study carried out inChapter 2.
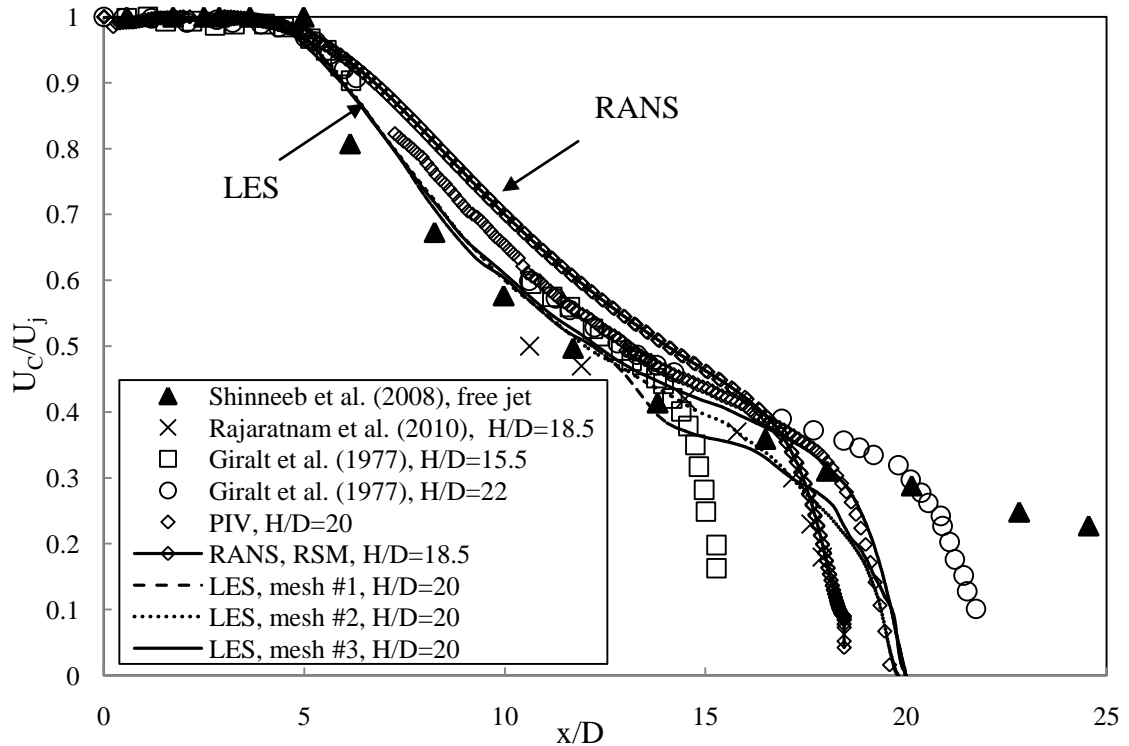
Fig. 3.7 Mean centreline velocity obtained from LES, RANS and experiments

Further validations were carried out by comparing other key flow parameters obtained from the numerical simulation (mesh #3) and experimental results. Figure 3.8a compares the mean static pressure distribution on the plate. The static pressure values are normalized by the pressure at the stagnation point (P_s). The radial direction is normalized by the jet half width ($r_{1/2}$), which is the radial position where $P = 0.5P_s$. Higher pressure is observed in regions close to the impingement zone, and the pressure decreases in the radial direction. The numerical prediction obtained from the current simulation is in good agreement with the measurements of Bradshaw and Love (1961), and a slight improvement over the RANS results.
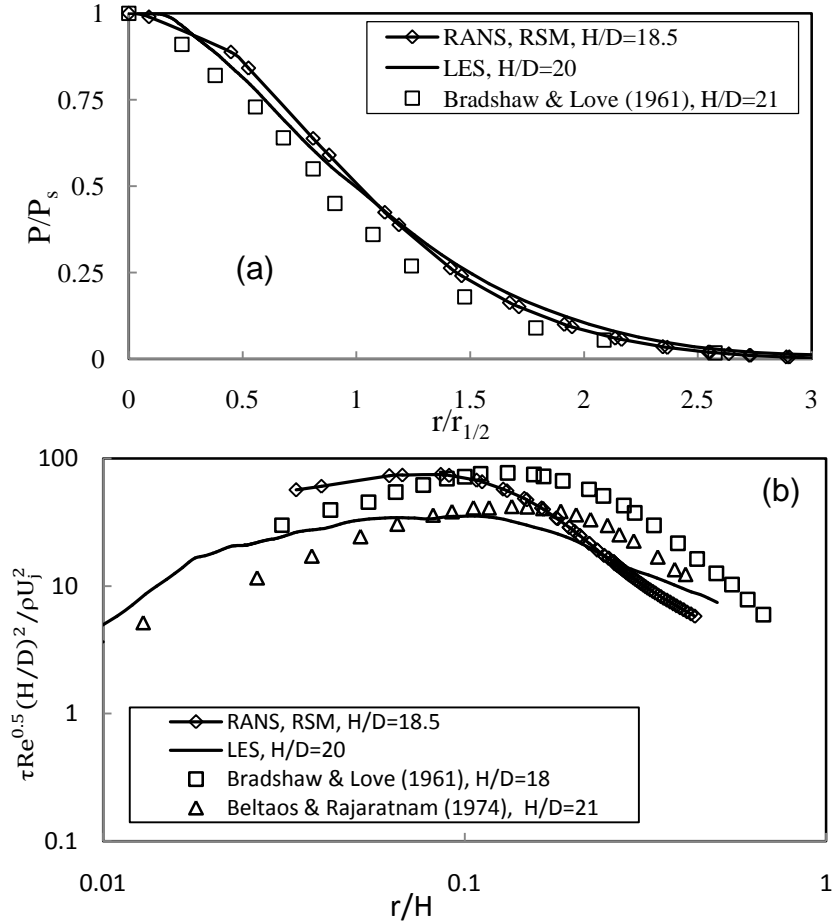
Fig. 3.8(a) Mean static pressure along the wall, (b) mean wall shear stress

Figure 3.8b displays the mean wall shear stress distribution. In this figure, the radial direction is normalized by the impingement distance, while the shear stress is normalized by ρU_j^2. The quantity plotted along the vertical axis is chosen to be consistent with other studies. A similar trend is observed between the data obtained from the simulations and the experimental data. The difference is likely due to different Reynolds number and variations in the experimental setups.

In Fig. 3.9 the turbulence intensities (u_{rms}, v_{rms} and w_{rms}) normalized with $U_j$are plotted to investigate the turbulence anisotropy along the centerline. Figure

3.9 shows that all three intensities start from a minimum value at x/D = 0 and reach a peak value at 6 < x/D < 8, indicating that the maximum rate of mixing occurs in this region. Streamwise turbulence intensity has larger values compared to the other components, suggesting that LES will be more accurate for impinging jet flows than models based on the assumption of isotropic turbulence. The results also show how the variation of the turbulence intensities are influenced by the presence of the impingement plate. Near the plate (x/D > 19), the v_{rms} and w_{rms} (turbulence components in y and z directions) exceed u_{rms} due to the strong anisotropy caused by the turning flow along the plate. In proximity of the plate, the large decay in streamwise turbulent velocity occurs due to the change in flow direction, where v_{rms} and w_{rms} components show a sudden increase. A good match between the numerical and experimental data is observed in the region of 10 < x/D< 18, and the results show that the turbulence intensities undergo a transition from x/D = 0 up to 8.
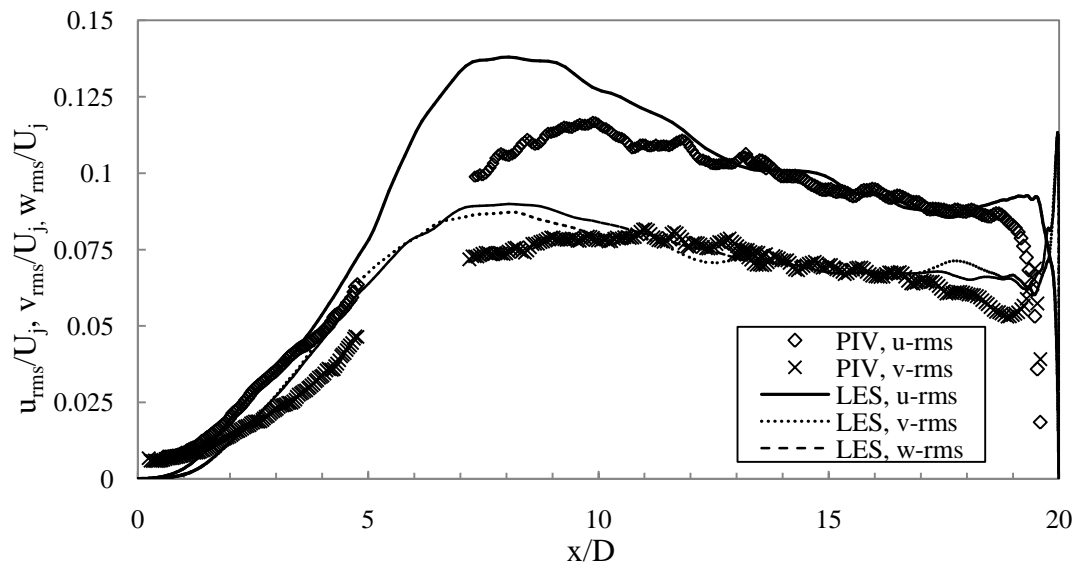
Fig. 3.9 Turbulence intensities obtained from LES and experiments
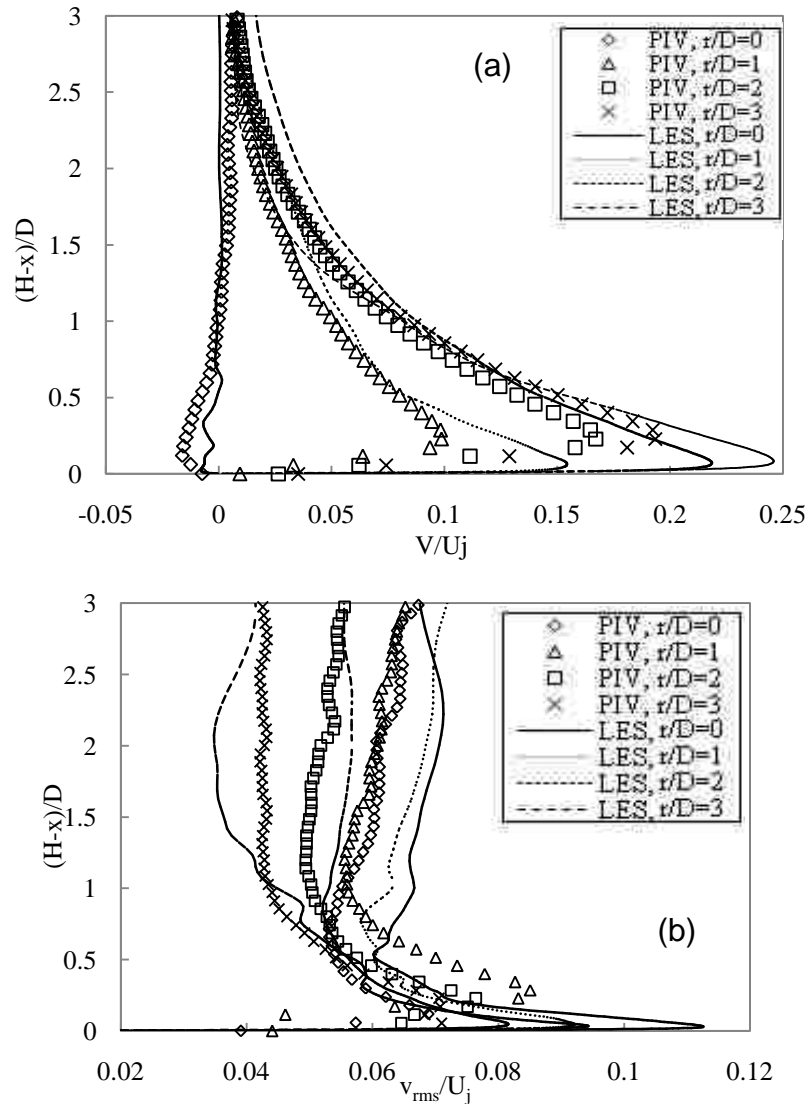
Fig. 3.10(a) Mean radial velocity profiles (V/U_j), (b) turbulent velocity profiles (v_{rms}/U_j) in wall region, at different r/D stations

Following impingement, the flow spreads out in the radial direction. Since the fluid flows along the wall, a boundary layer is expected to be formed. The mean and fluctuating radial velocities normalized with the jet exit velocity are plotted as a function of (H-x)/D in Fig. 3.10, where (H-x) is the normal distance from the plate. Figure 3.10 illustrates the comparison between the results

obtained from the LES and experiments at different r/D stations along the plate. Basically, these results show that both mean and fluctuating components of the velocity follow the developing behaviour of a wall jet. As discussed earlier, the flow changes direction from axial to radial when it gets close to the plate. This phenomenon can be observed in the mean radial velocity values in Fig. 3.10a, as they start to increase from zero at r/D = 0 to higher values at r/D = 1, 2 and 3. The space between the profiles decreases along the wall jet, indicating that the flow is tending to a fully developed condition.

For the turbulent values, although there is not good agreement between the experiments and CFD in the proximity of the plate, the trend of the profiles in this region is very similar. This issue may be expected due to the higher levels of uncertainty associated with the measurements in the wall proximity. In the region where the wall effect is negligible, good agreement between the CFD and experiments can be observed.

Figures 3.11a,c and e demonstrate the contours of mean velocity magnitude superimposed with the sectional streamlines, streamwise turbulent velocity fluctuations and shear stress distribution in the entire domain, respectively. Figures 3.11b,d and e show the contours of the same parameters in the proximity of the plate. These figures confirm that there is a symmetrical behaviour for the flow parameters with respect to the axis. Sectional flow streamlines show the presence of a stagnation streamline which is located along the jet axis. As one would expect, many of the unsteady flow features are absent in these figures. As can be seen in these figures, turbulent velocity fluctuations

66

and shear stresses also show symmetrical behaviour with respect to the axis. The marginal discrepancies observed are due to the averaging time during the simulation period. An unsteady analysis will reveal the behaviour of these parameters over time and elucidate their deviation from the mean values.
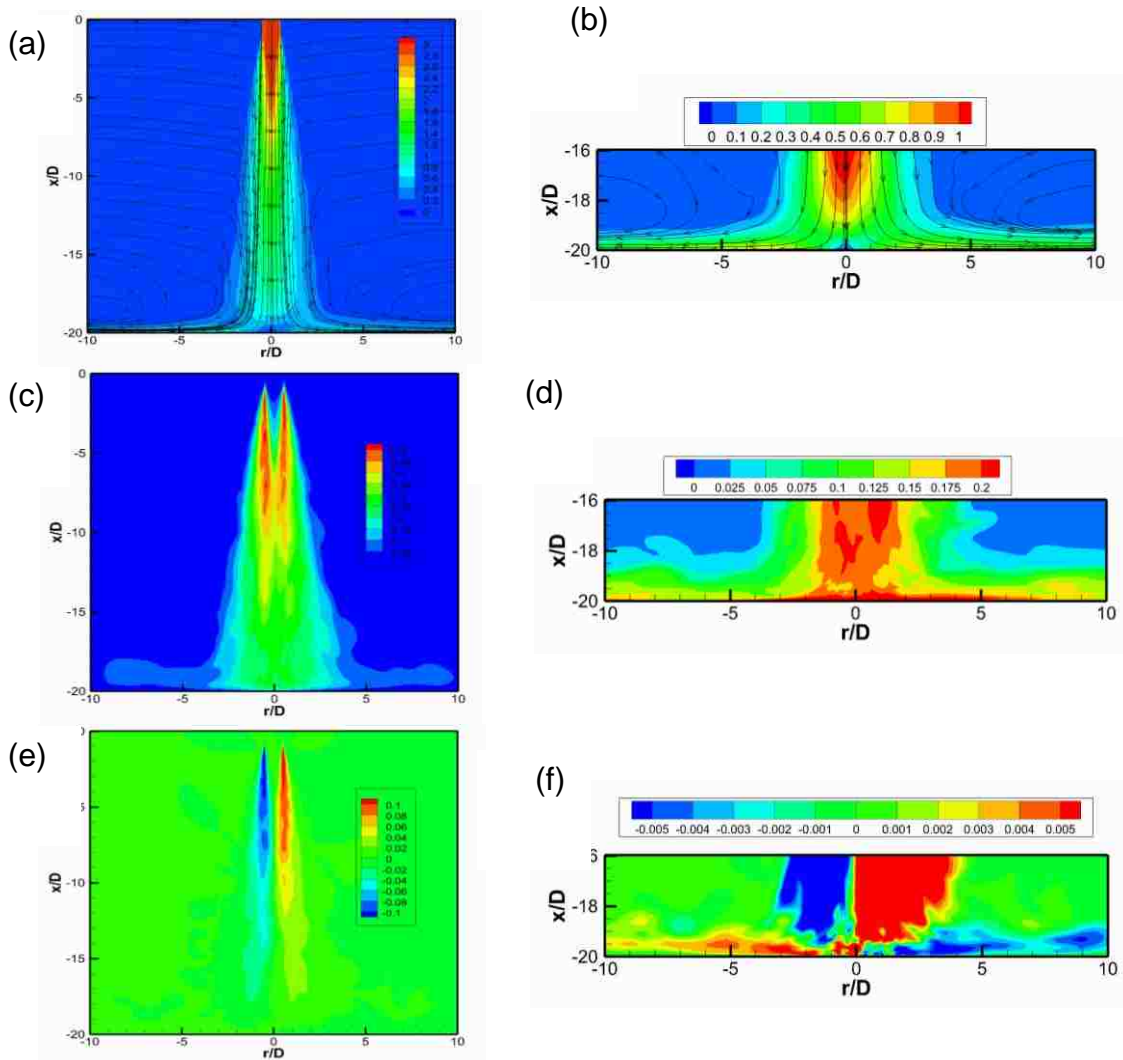
Fig. 3.11 Contours of (a,b) mean velocity magnitude superimposed with sectional streamlines, (c,d) streamwise turbulent velocity fluctuations and (e,f) shear stress in the whole domain and close to the plate

3.4. Unsteady results

In this section, the evolution of the ring vortices generated in the domain due to the entrainment of the jet and the ambient flow and their effect on different flow regions will be discussed. This includes behaviour of structures in the free jet region, impingement zone and also in the wall jet portion of the flow.

Different methods can be employed to visualize the three-dimensional flow structures. The literature shows that intuitive methods such as vorticity contours, pressure minima and streamline plots have largely been used for this purpose. Jeong& Hussain (1995) developed the λ_2 criterion which can be used to identify the core of the vortices that exist in the flow field, using the fact that these cores are related to the locations of minimum pressure in the flow. Basically, this method connects the high vorticity and minimum pressure regions in the flow.

Jeong & Hussain (1995) derived the λ_2 criterion by taking the gradient of the Navier-Stokes equation and decomposing the acceleration gradient term into symmetric and antisymmetric parts, expressed as $S_{ij}S_{ij} + \Omega_{ij}\Omega_{ij}$, where S_{ij} and Ω_{ij} are the symmetric and antisymmetric parts of the velocity gradient tensor, respectively. The Hessian of the pressure can then be connected to the vortical motions in the flow. According to the theory of multivariable calculus, the $S_{ij}S_{ij} + \Omega_{ij}\Omega_{ij}$ tensor has three real eigenvalues ($\lambda_1 \geq \lambda_2 \geq \lambda_3$). The point of local pressure minimum requires two eigenvalues of this tensor to be negative. λ_2, which corresponds to the second largest eigenvalue of this tensor, is representative of the local pressure minima region. The iso-surface of λ_2 can be

used for visualizing instantaneous structures in the flow. In this study, the different above-mentioned visualizing methods have been used depending on the flow region.

3.4.1. Free jet region

Figure 3.12a shows the iso-surface of λ_2 criterion coloured with velocity magnitude contours and Fig. 3.12b shows the iso-surface of static pressure (-20 Pa) coloured with vorticity magnitude contours.

For the current case (H/D = 20), from x/D = 0 ~ 15 the jet behaves very similar to a free jet, in which the core of the jet undergoes a decay before reaching the plate.

The vortices generated due to the Kelvin-Helmholtz instabilities form a street of rolled up vortex rings as illustrated in Fig. 3.12a. These vortices, while traveling towards the plate, interact, pair and coalesce with neighbouring vortices with increased azimuthal instability, thereby reducing their circumferential coherence. The distance between these vortices increases and the ring-like shape is lost when the flow approaches the impingement plate (Fig. 3.12b).

(a)
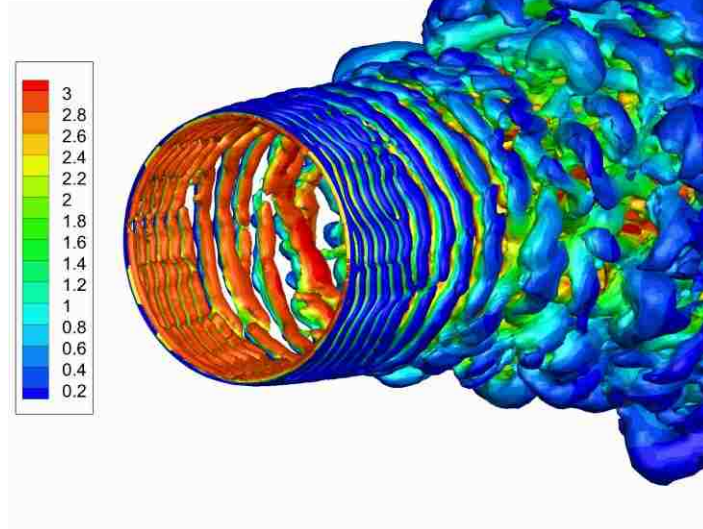
(b)
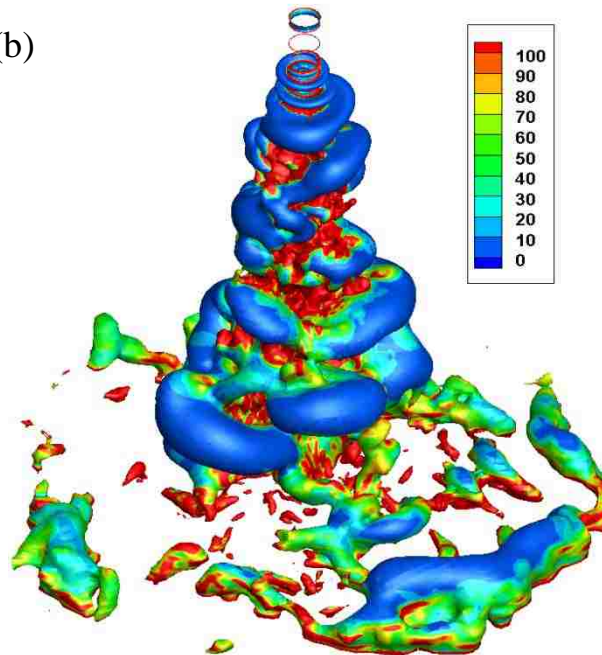
Fig.3.12 Iso-surfaces of a) λ_2 criterion colored with velocity magnitude contours,

b) static pressure (-20 Pa) colored with vorticity magnitude contours

70

The expansion and stretching of the ring-like vortices caused by the azimuthal instabilities are demonstrated in Figs. 3.13a-I, which show vorticity magnitude contours in the y-z plane at different axial stations. The colour scale has been kept the same for all figures except in Fig. 3.13h because of the reduced vorticity magnitude at this axial location ($x/D = 15$). In regions very close to the nozzle ($x/D = 1$~1.5), the ring vortices have a diameter similar to the nozzle exit diameter with the highest vorticity located around the ring at about $r/D = 0.5$. As the vortices move axially, they become highly deformed with vertical patches which are nested around the ring by the time they reach $x/D = 2$. Basically, these patches of instability serve as a mechanism for transforming into the large scale eddies downstream. Figure 3.13 show that the number of these patches reduces as the fluid flows towards the plate. This may be attributed to the pairing and growing of these structures.

At a particular distance from the nozzle, the ring-like vortices start to breakdown due to tilting and three-dimensional effects which cause the vortices to lose their axial symmetry. This results in the broken down structures striking the plate at different time instances. The asymmetric impingement of the large scale structures results in jet flapping and meandering around the jet axis.
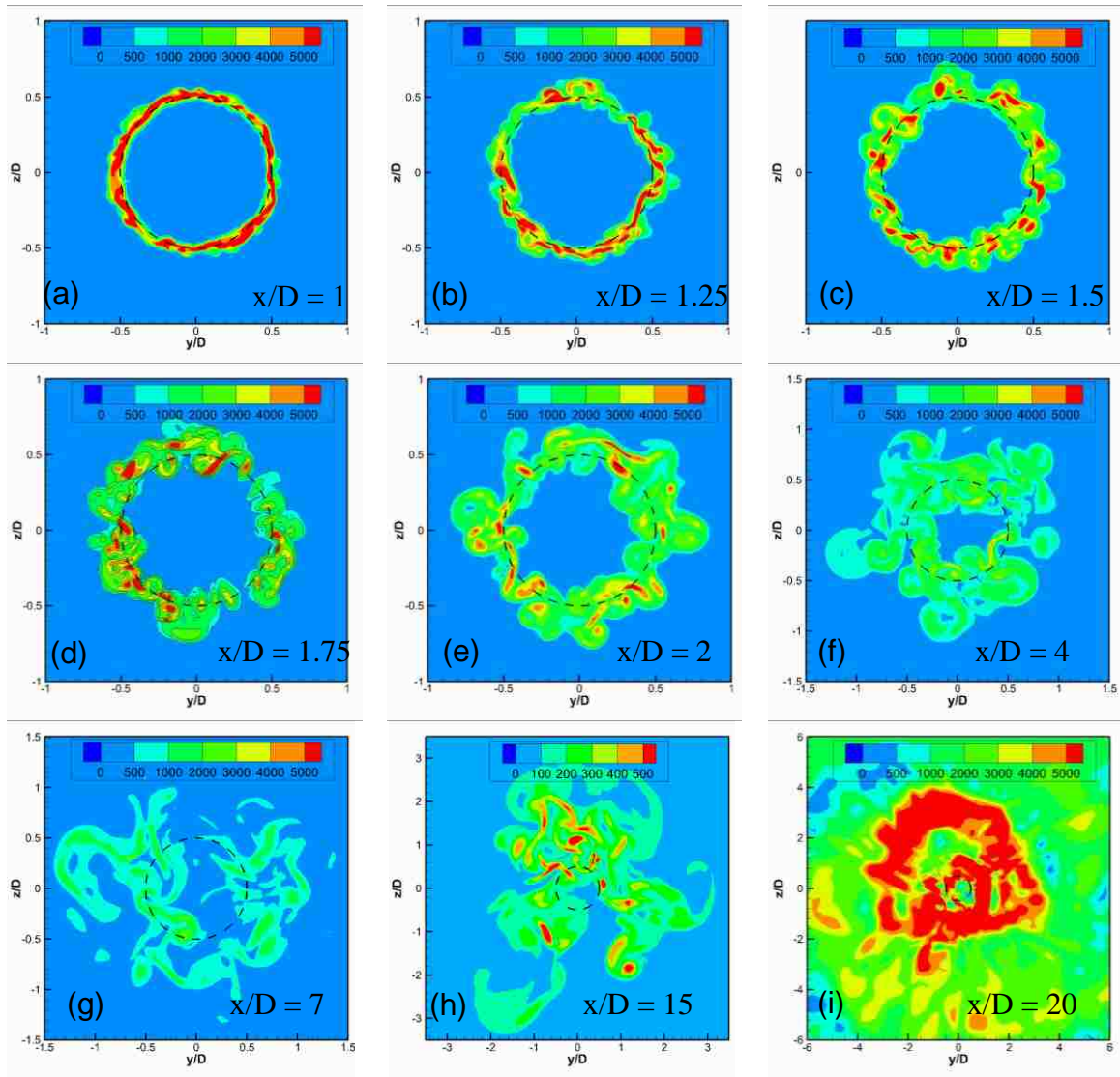
Fig. 3.13 Deformation of shear layer in y-z plane visualized by the instantaneous vorticity magnitude contours at (a) x/D = 1, (b) x/D = 1.25, (c) x/D = 1.5, (d) x/D =1.75, (e) x/D = 2, (f) x/D = 4, (g) x/D = 7, (h) x/D = 15, (i) x/D = 20

To analyze the frequency of the ring vortices generated, the Strouhal number ($St= f_1 D/U_j$) of these vortices was determined. Here, f_1 is the frequency of the generated ring vortices, D is the nozzle diameter and U_j is the jet exit velocity.

One should note that based on the observations of Hadziabdic and Hanjalic (2008) and Tsubokuraet al. (2003), the Strouhal number is strongly dependent on Reynolds number, initial velocity profile and most importantly the distance between the nozzle and the plate. In the current study, to determine the frequency of the shear layer instabilities, the energy-density spectra, obtained from a time series of the instantaneous static pressure at x/D = 2, r/D = 0.5 was examined. The time history of the pressure data is presented in Fig. 3.14a. Applying a FFT on this data identifies a dominant frequency of 180 Hz which corresponds to a Strouhal number of 0.63.
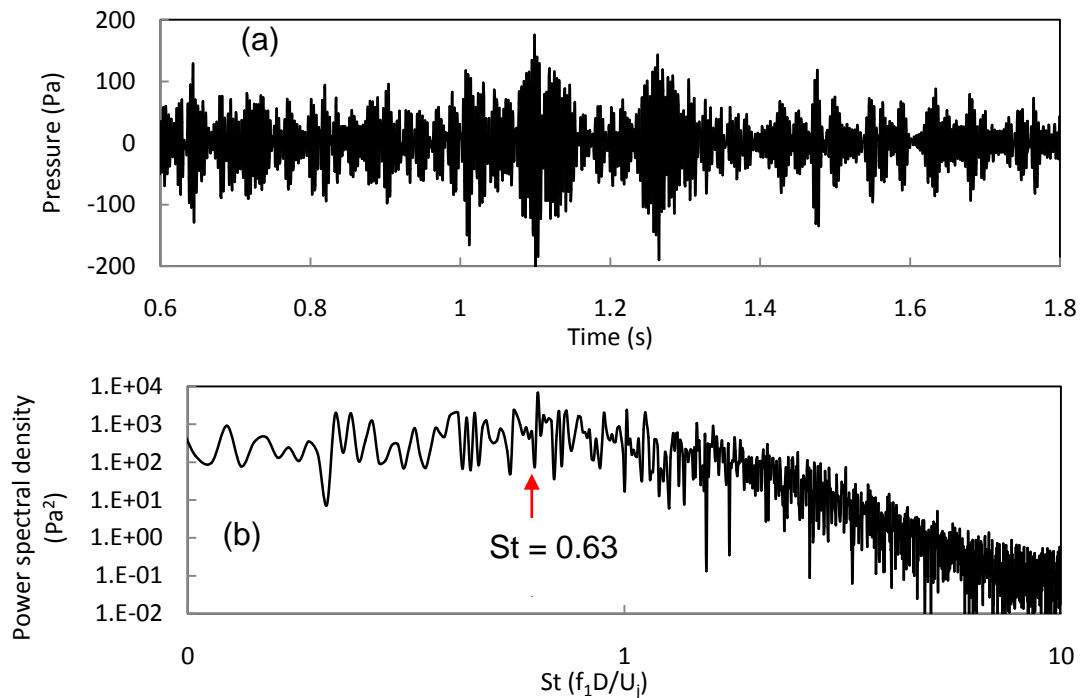
Fig. 3.14(a) History of static pressure, (b) power spectral density at x/D = 2 and r/D = 0.5

For comparison, Table 3.2 presents Strouhal numbers from previous studies and from the current simulation. As can be seen, the St predicted in the current simulation is in the range of previous experimental results at similar Reynolds numbers.

Table 3.2 Experimental and numerical values of Strouhal number

Experiments	x/D	Reynolds number	Strouhal number
Yule (1978), free jet	0.4	21,000	0.60
Yule (1978), free jet	5~6	21,000	0.33~0.4
Han & Goldstein (2003), free jet	1.0	8,000	0.65
Han & Goldstein (2003), free jet	1.0	120,000	0.60
Tsubokuraet al. (2003), H/D=10	3~8	6,000	0.37
Hadziabdic&Hanjalic (2008), H/D=2	0.1	21,000	0.64
Current LES study, H/D=20	2.0	28,000	0.63

As previously mentioned, due to the mixing and the level of the turbulence, the ring vortices lose their form, become entangled and evolve into large scale structures as they move towards the plate. As the ring vortices travel towards the impingement zone, they break down and lose their shape. The decrease in the number of ring vortices can be interpreted as a reduction in their frequency. To investigate the existence of a characteristic frequency (f_2) or period (T_2) for the structures hitting the plate, the pressure history at x/D = 18 and r/D = 5 was recorded. The time history of the static pressure monitored at this point is presented in Fig. 3.15a. Following this, a FFT was carried out to determine any possible peak frequency for this time history, as illustrated in Fig. 3.15b. Figure 3.15b shows a peak at a frequency of 5.6 Hz, which can be considered as the

characteristic frequency for the large structures impinging on the plate. Based on this frequency, the characteristic period (T_2) is equal to 0.18.
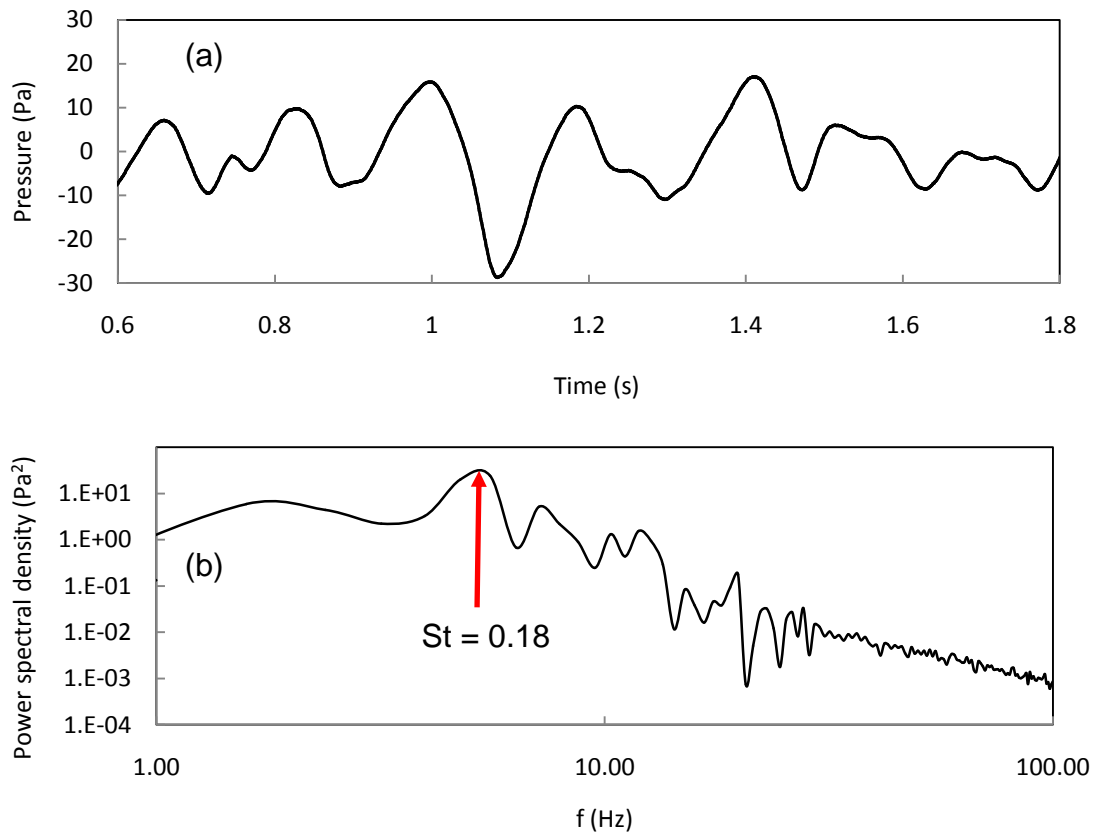
Fig. 3.15(a) History of static pressure, (b) power spectral density at x/D = 18 and r/D = 5

3.4.2. Stagnation zone and wall jet region

To analyze the flow structures in the impingement region, velocity magnitude contours in the y-z plane as well as the static pressure contours in x-y and x-z planes superimposed with the sectional flow streamlines at different time

instances over the characteristic period (T_2) are plotted in Fig. 3.16. The y-z plane parallel to the plate is located at (H-x)/D= 0.05, which is slightly above the plate. Five equal time intervals with $\Delta t = T_2/5$ was chosen for evaluation. In this comprehensive figure, a,b,c, etc denote the flow field at different time instants. The index 1 refers to y-z plane (e.g., Figure 3.16a1), index 2 refers to the x-y plane (e.g., Figure 3.16a2) and index 3 refers to the x-z plane (e.g., Figure 3.16a3).

In Figures 3.16a1-f1, the red patches indicate the high velocity regions. In each of these figures the red patches are located in different regions of the flow field. It appears that the location of these patches depend on the shape of the large scale structures impinging on the plate. Although a semi-circular pattern can be observed for these patches, they are not circumferentially connected. These figures confirm the asymmetric impact of the large scale structures on the plate.

The asymmetric impingement of the large scale structures also influences the location of the stagnation region, which can be observed by the behaviour of sectional streamlines in x-y plane. The dotted circle in the middle of Figures 3.16a1-f1 indicates the location of the nozzle above the plate. As seen in Figs. 3.16a1-f1, different stagnation patterns exist in the impingement zone at different times. One single patch of low velocity magnitude flow (in blue color with streamlines starting from that location) can be seen at the beginning of the characteristic period (T_2) which represents the stagnation zone. As time goes on the shape of the stagnation zone changes and becomes more distributed on the

plate. Different disperse patches of blue color (with streamlines starting from that region) representing the stagnation zones can be observed on the plate. These zones are located significantly off the axis of symmetry relative to the beginning of the period.

The stagnation regions reach a maximum distance of r/D = 2 from the axis of symmetry during the characteristic period. Note that, this dispersed form of stagnation regions are a result of the impingement of the broken down, disconnected, three-dimensional structures. At the end of the period (T_2), the shape of the impingement region gets close to its original form at the beginning of the period (T_2). At this instant of time the stagnation region gets close to the axis of symmetry and no other stagnation zone can be observed on the plate.

Figure 3.16 also shows the flow streamlines in the x-y and x-z planes at different time intervals of the characteristic period (example, Figs. 3.16a2 and a3, Figs. 3.16b2 and b3, etc). The fluid structures have different shapes and sizes and are deflected in the radial direction while getting close to the plate. This behaviour influences the flow in the impingement zone as can be observed in the x-y and x-z planes. One of these influences is the change in the pressure contours noticed in the impingement zone. The presence of an adverse pressure gradient in different directions will allow for the generation of secondary vortices in the impingement zone.
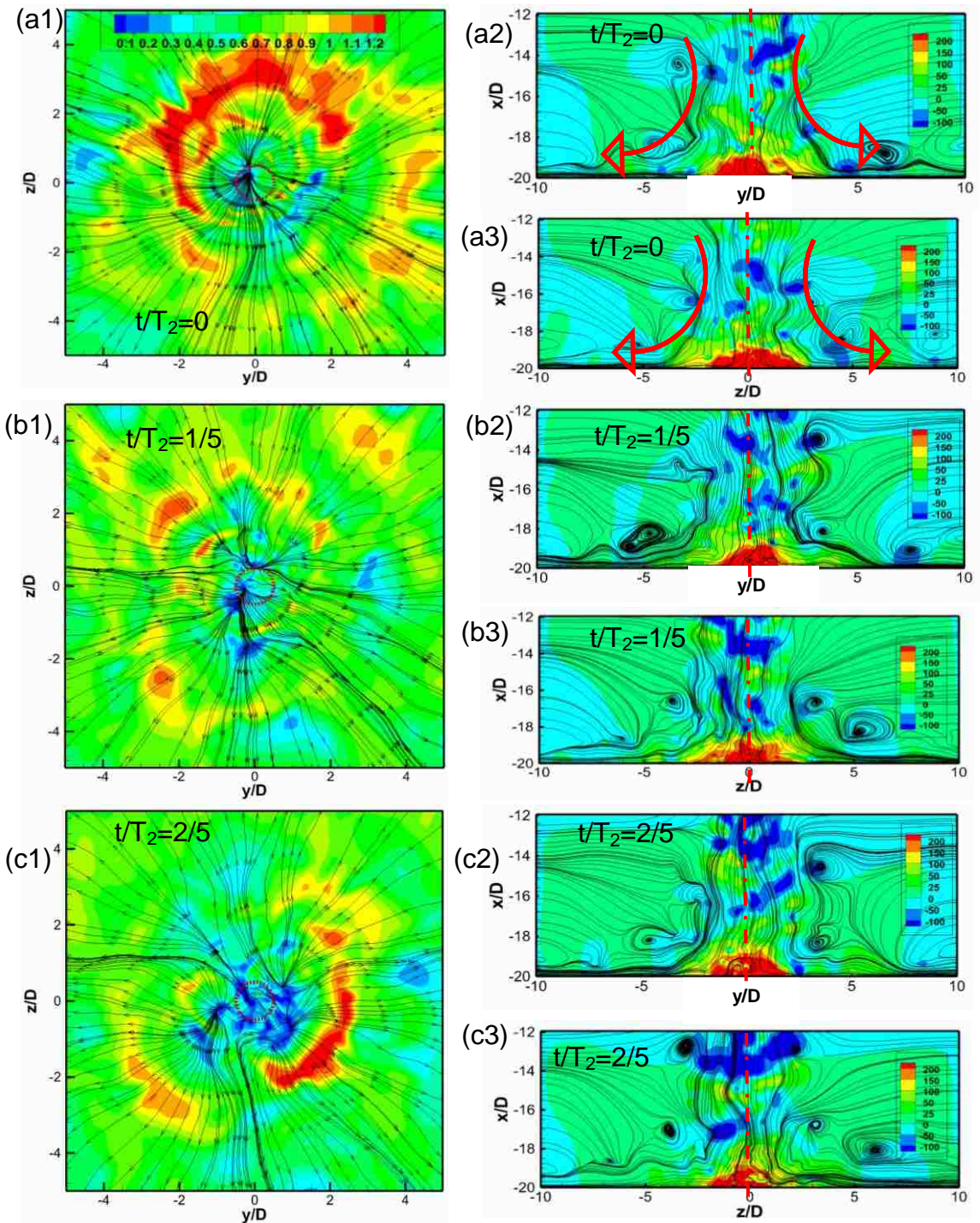
Fig. 3.16 Instantaneous velocity magnitude (y-z plane) and static pressure contours (x-y and x-z planes) with sectional streamlines over the characteristic period (T_2), (a) $t/T_2=0$, (b) $t/T_2=1/5$, (c) $t/T_2=2/5$, (d) $t/T_2=3/5$, (e) $t/T_2=4/5$ and(f) $t/T_2=5/5$ (the red circle in y-z plane shows the nozzle) (continued)
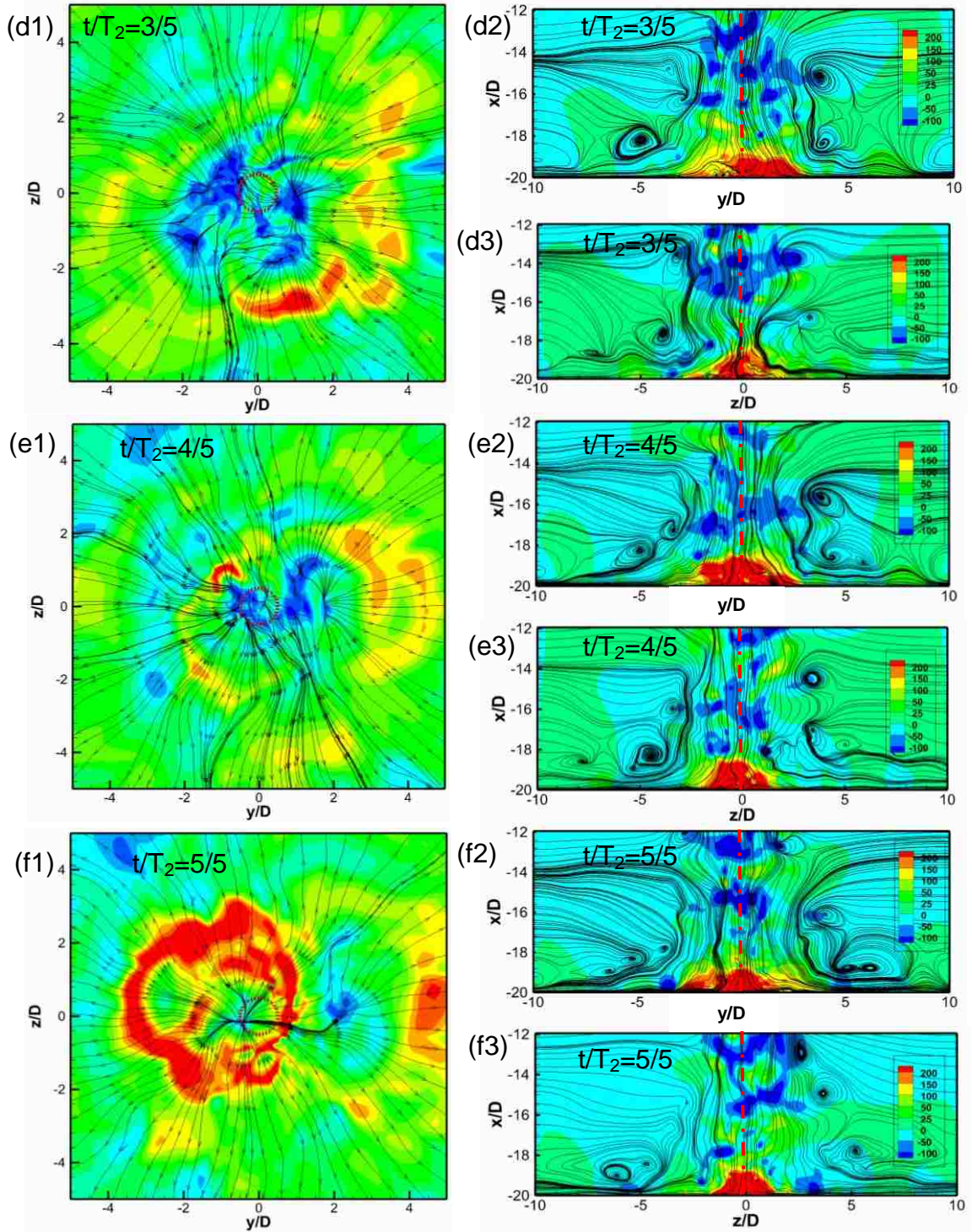
Fig. 3.16 (continued) Instantaneous velocity magnitude (y-z plane) and static pressure contours (x-y and x-z planes) with sectional streamlines over the characteristic period (T_2), (a) $t/T_2=0$, (b) $t/T_2=1/5$, (c) $t/T_2=2/5$, (d) $t/T_2=3/5$, (e) $t/T_2=4/5$ and(f) $t/T_2=5/5$ (the red circle in y-z plane shows the nozzle)

Due to the large distance between the nozzle and the plate (H/D = 20), the maximum dislocation of the impingement point from the axis of symmetry is quite different from impinging jets with small nozzle-to-plate ratio (H/D < 4). Hadziabdic and Hanjalic (2008) noticed a maximum dislocation of r/D = 0.1 and a split of impingement point to two lines for H/D = 2. They suggested that the origin of the impingement point oscillation arises from the instability and tilt of the structures generated from the shear layer of the jet.

In this study, due to the large distance between the nozzle and the plate, the oscillation of the structures is larger. At the beginning of the characteristic period the stagnation region (dark blue regions in Fig. 3.16a1) has a form of point with a maximum dislocation of r/D = 0.5 from the axis of symmetry. As time goes on different stagnation regions can be observed on the plate (at t/T_2 = 3/4 and 4/5). The maximum distance of these stagnation regions is about r/D = 2 from the axis of symmetry. Basically, one of the important differences observed for impinging jets with large nozzle stand-off distance relative to small nozzle height-to-diameter ratio cases is the existence of these unorganized patches of stagnation regions distributed over the plate.

After impingement the flow changes direction from axial to radial and a thin boundary layer is formed on the plate (referred to as the wall jet region). The sectional streamlines show an asymmetric behaviour at all times, caused by break-up and tilting of the largescale structures and the consequent three-dimensionality of the flow in this part of the flow region. The structures occurring in the wall jet region are remnants of the ring-like vortices generated from the

nozzle shear layer which survive the impingement. The radial deflection of the structures results in minor separated regions in the wall jet flow with a counter-rotating wall-attached form. Figure 3.17 is a magnified view of Fig. 3.16f2 which demonstrates this phenomenon.
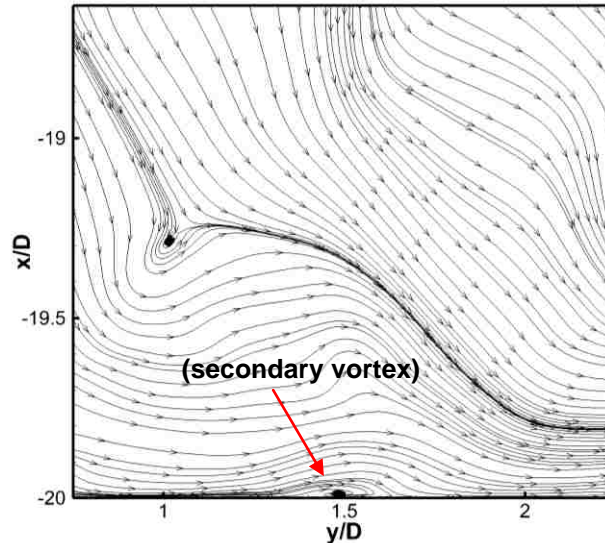
Fig. 3.17 Generation of secondary vortices in the wall region

According to the analyses of Dairay et al. (2015) for an impinging jet with H/D = 1 and Hadziabdic and Hanjalic (2008) for H/D = 2, several secondary vortices occur in the wall jet region which are generated due to the influence of deflected nozzle vortices. This behaviour causes unsteadiness and fluctuations in the wall pressure and shear stress. Based on the flow streamlines and pressure contours presented in Figs.3.16a-f, the deflected large scale structures do not result in significant flow separation in the wall region. Basically, this behaviour illustrates another major difference between impinging jets with large

and small stand-off distances. This phenomenon is investigated in detail in the next section.

3.4.3. Wall shear stress

At the start of the characteristic time period, Figures 3.18a and b show the instantaneous sectional streamlines in the x-y plane (not scaled) and the wall shear stresses in the y direction, respectively. Similarly the rest of the figures in Fig. 3.18 show the distributions at other time instants over the characteristic period. In these figures the mean wall shear stresses are compared with the instantaneous results over the characteristic period (T_2). The wall shear stress (τ) is normalized with the maximum mean value ($\tau_{\text{mean-max}}$) along the y direction. Note that these figures are presented at the same instantaneous time steps as presented in Fig. 3.16. Figures 3.18a-f show that, unlike that seen in the mean profile, there are multiple peaks in the instantaneous wall shear stress profile.
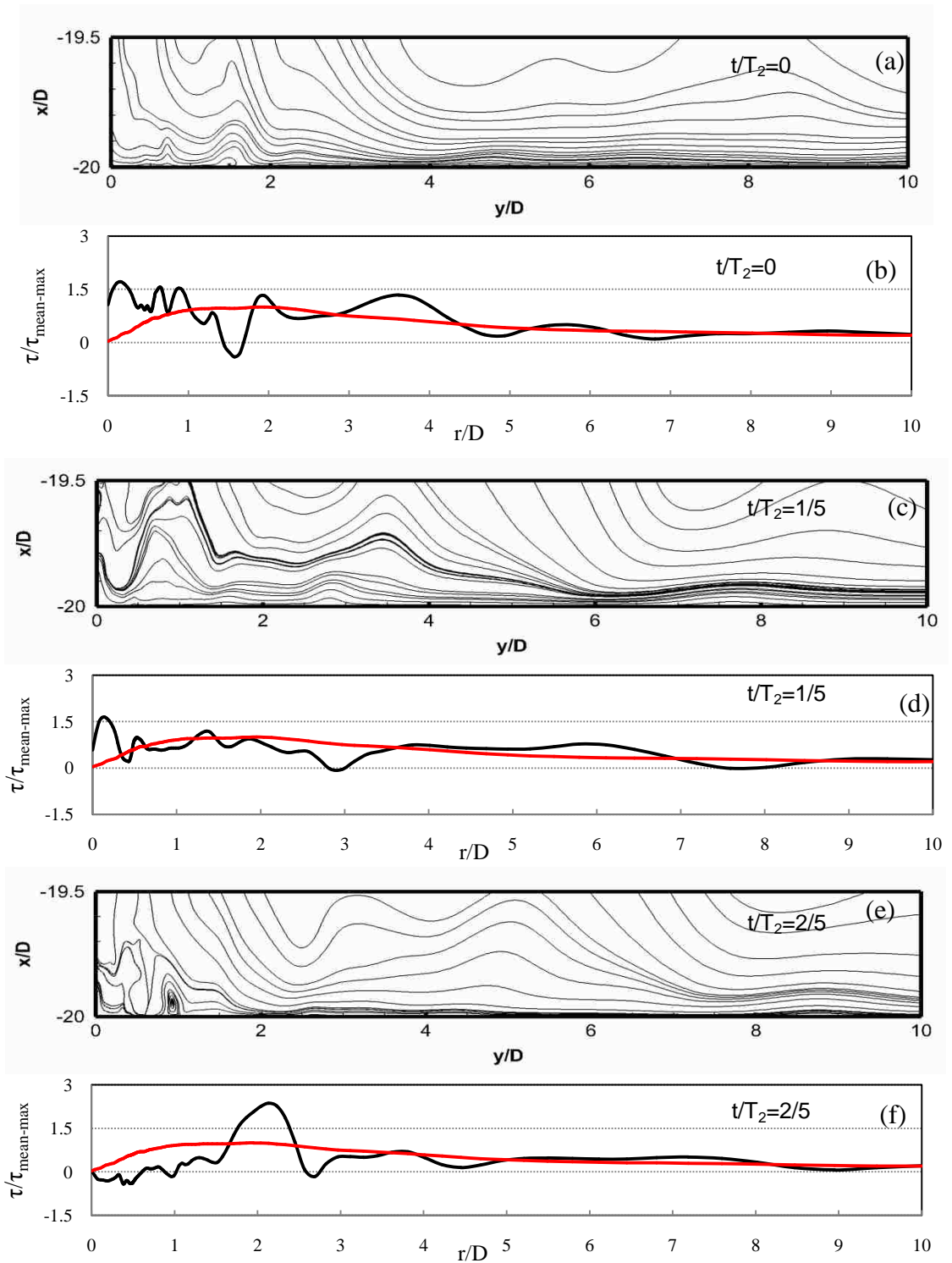
Fig. 3.18 Instantaneous sectional streamlines and (black) and mean (red) wall shear stress in x-y plan over the characteristic period (T_2), (a,b) $t/T_2=0$, (c,d) $t/T_2=1/5$, (e,f) $t/T_2=2/5$, (g,h) $t/T_2=3/5$, (i,j) $t/T_2=4/5$ and (k,l) $t/T_2=5/5$ (continued)
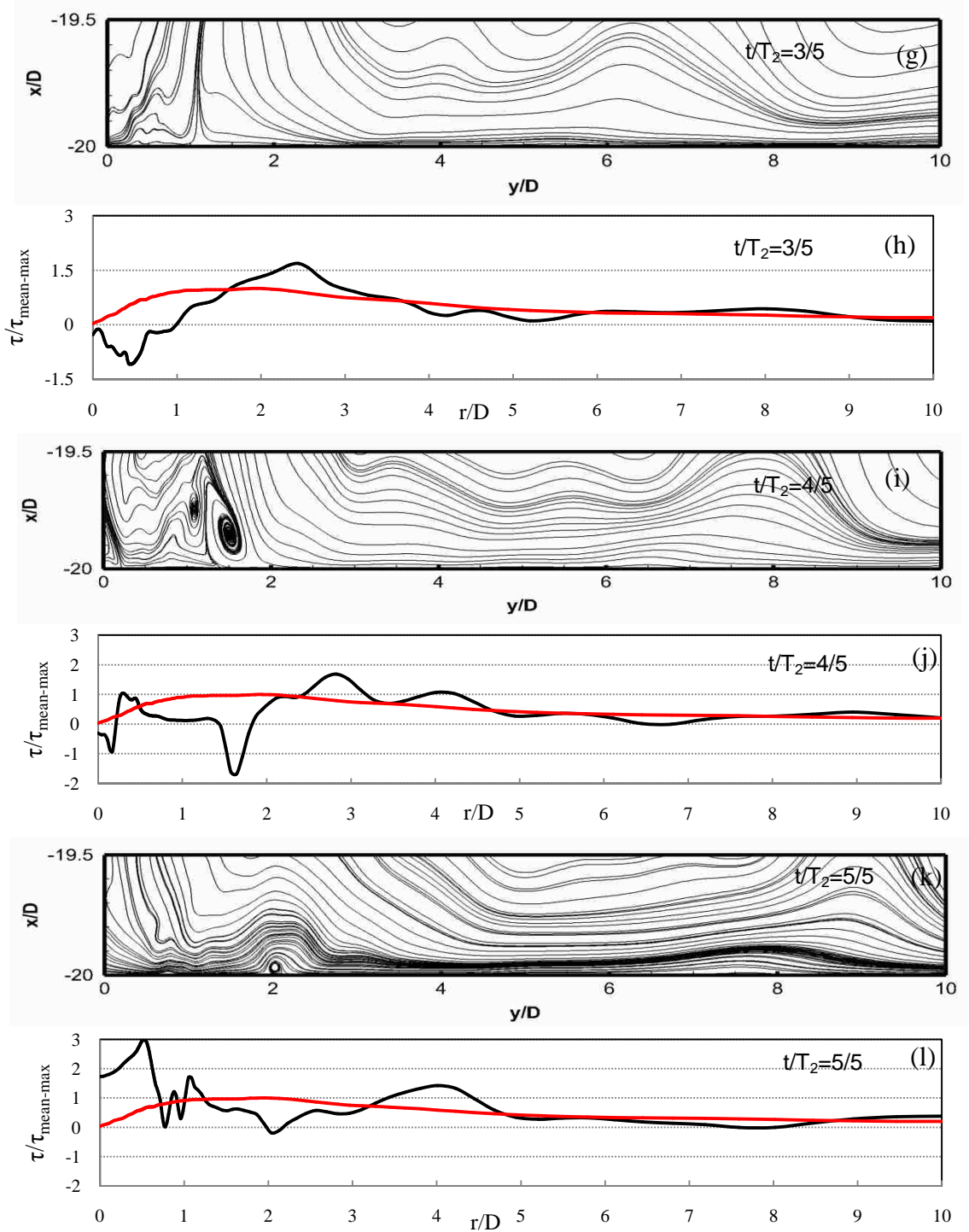
Fig. 3.18 (continued) Instantaneous sectional streamlines and (black) and mean (red) wall shear stress in x-y plan over the characteristic period (T_2), (a,b) t/T_2= 0, (c,d) t/T_2= 1/5, (e,f) t/T_2= 2/5, (g,h) t/T_2= 3/5, (i,j) t/T_2= 4/5 and (k,l) t/T_2=5/5

Three-dimensional unsteady structures impinging on the plate result in fluctuations in wall shear stresses. Comparison of the sectional streamlines with the associated wall shear stress profiles shows that large scale structures deflected after impingement do not cause severe wall shear stress fluctuation in regions with r/D > 5. No negative sign can be seen for the wall shear stress in this range during the characteristic period. However, large fluctuations relative to mean values, with a number of negative values, can be seen in the region between 0 < r/D < 5. These negative wall shear stress values are a result of the separation of flow in the impingement zone and generation of secondary vortices in that region (see Figs. 3.18a,c,e,g,i,k).

3.5. Conclusions

A LES based analysis was carried out to characterizea turbulent round impinging jet with a large stand-off distance. Modelling this type of long jet is computationally more expensive than short impinging jets normally discussed in the literature.

Three meshes with different number of cells (6.3M, 7.6M, 10.6M) were used to ensure the mesh requirements in LES were satisfied. In addition to the mesh requirement, a Courant number of less than 0.5 was also considered for the current simulations. The decay of centreline velocity from the three different meshes was compared with the available experimental data. Based on the mesh requirement analysis and the quality of the results when compared with the

experiments, the 10.6M cell mesh was selected for subsequent computations. Based on these evaluations the LES framework showed good capability in capturing the mean value fields in all three sub-regions of the domain including the free jet, impinging zone and wall jet regions.

Turbulence generation at the inlet of the computational domain plays an important role in large eddy simulations which significantly affects the downstream flow field. To introduce a correct shear flow and a proper level of turbulence at the exit of the nozzle, flow inside the nozzle was modelled separately. Good agreement between the experimental and computational results close to the nozzle and inside the tank suggests that the flow inside the nozzle has been accurately modelled.

The dynamics of the roll-up vortices created by the instabilities in the initial shear layer close to the nozzle influences the entire flow field including the free jet region, impinging zone and wall jet region. It was found that these roll-up vortices have aStrouhal number of 0.63 near the nozzle. However, this parameter is reduced along the centreline towards the impingement zone. While moving towards the plate, these vortices merge, breakdown or change into largescale structures. Up to four diameters from the nozzle exit, these vortices retain their ring-like shape. In the range of $4 < x/D < 7$, a transition occurs and the vortices start to change into largescale structures. For $x/D > 7$, there is no sign of the ring-like vortices as they are transitioned to form large scale structures. Due to the asymmetric behaviour of the structures, these eddies are tilted from the streamwise direction. The expansion, growth, tilt and unsteady behaviour of the

impinging structurescausedislocation of the impinging flow from the centreline, which is significantly larger when compared with cases with small H/D ratios. Unlike in the cases with small H/D ratios, for large stand-off cases, the largescale structures do not present a self-organizing tendency towards a ring-like shape after impingement.

No connection was observed between the frequency of generation ofthering-like vortices close to the nozzle with that for the largescale structures close to the plate. In the current study a pressure "probe" (numerical monitoring) was set at a location close to the plate to determine the frequency of the structures hitting the plate. Based on the pressure history, a FFT operation was carried out on the signal and the dominant frequency was captured. The behaviour of the structures in the impinging zone and in the wall region were analyzed using this characteristic frequency.

Different patterns of velocity distribution were observed in the impingement region over one cycle. Initially, the stagnation region was in the form of an organized circular shape. As time passes, different patches of low velocity magnitude contours representing different stagnation regions were observed. Due to rotation, tilting and unsteadiness of the large scale structures approaching the plate, and also considering the large distance between the nozzle and the plate, a large dislocation of the jet stagnation regions was observed compared to cases with small stand-off distances.

CHAPTER 4

CFD SIMULATION OF BOILING HEAT TRANSFER IN AN IMPINGING JET

USING OPENFOAM

4.1. General remarks

In this chapter a CFD model has been systematically developed to simulate subcooled boiling heat transfer in an impinging jet. Due to the difficulties associated with commercial software for modifying the code and implementing appropriate experimental correlations, the OpenFOAM source code is employed as the basic software upon which the boiling model has been built. OpenFOAM's two-phase Eulerian-Eulerian approach is used and the model development procedure involves three stages. Initially, the model is developed for an adiabatic two-phase flow in a pipe. In the second stage, the energy equation and boiling model are incorporated in the CFD model for pipe flow to solve for the heat transfer and boiling phenomena. The third part of the work involves extending the CFD model to simulate the boiling heat transfer due to an impinging jet.

4.2. Introduction

Subcooled boiling is a phenomenon which occurs in many applications such as in the automotive industry and cooling of electronic components. As Fig. 1.4 shows, in some conditions the boiling phenomenon increases the heat transfer rate from the surface, while in other cases it significantly reduces the heat transfer which could lead to the wall temperature increasing to the burnout point. This is directly related to the position of the point on the boiling curve where the amount of heat flux from the plate is related to the wall superheat temperature. If the point is located in the nucleate boiling regime, a minor change

in the wall superheat leads to the removal of a large amount of heat from the surface. If the point stays in a region before nucleate boiling, a change in the wall superheat will not be as beneficial as in the nucleate region and, if it is next to the nucleate region, any change in the wall superheat will be accompanied by a reduction in wall heat removal, which can lead to a burnout point and is potentially very dangerous.

There are a number of studies reported in the literature on the numerical modeling of subcooled boiling. In this regard, the model developed at Rensselaer Polytechnic Institute (RPI) by Kurul and Podowski (1991) has gained significant attention. According to the RPI model, the boiling heat transfer is divided into three components; convective, quenching and evaporative heat fluxes. The convective part is for single-phase convection, quenching refers to liquid filling the wall vicinity after bubble detachment due to vaporization, and the evaporative component is for the fluid that evaporates.

Due to the complex nature of the boiling phenomenon, numerical studies have had to deal with many challenges involved in modelling boiling. Hibiki and Ishii (2002) have introduced models for breakup and coalescence of bubbles. Yao and Morel (2004) studied the effect of a new time scale on the turbulence induced coalescence and breakup. They also investigated the nucleation of new bubbles on the volumetric interfacial area and were able to predict the local two-phase parameters under boiling flow conditions. Recently, Michta (2011) simulated nucleate boiling using OpenFOAM. However, he could not obtain satisfactory results when compared to the experimental results. Although he

intended to simulate two-phase pipe flow, the model that he developed used a 2D planar rectangular mesh instead of a 2D axisymmetric mesh. This created inaccuracy in the results due to the cancellation of circumferential fluxes in a 2D mesh.

In thepresent study, it is of interest to develop a numerical model using OpenFOAM, to predict and analyze the boiling phenomenon in mechanical systems such as impinging jets. It is also of interest to improve upon the results obtained by Michta (2011) by using different numerical setups and experimental correlations. The default Eulerian-Eulerian model was selected as the basic model for further development.

The developmentof the model is carried out in three stages. In the first stage, an isothermal two-phase model is developed for solving the two-phase bubbly flow without heat transfer in a pipe, taking into account the effect of different interfacial forces including drag, lift, added mass, wall lubrication and turbulent dispersion forces. For each of these forces, different experimental correlations have been selected from the literature to enable the user to choose the most appropriate correlation for the geometry which is being modeled. The effects of bubble breakup and coalescence have also been added to the model.

In the second stage, the energy equation is linked to the main loop. The boiling model is then incorporated and linked to the main loop. Different numerical setups and boundary conditions corresponding to the simulations carried out by Michta (2011) were also used in an effort to improve the quality of

the results. The results, which include prediction of the two-phase flow parameters and the temperature field, are compared with the available experimental data and previous numerical results.

In the third stage, the boiling model is upgraded to simulate the boiling heat transfer in an impinging jet. It is expected that at this stage of development, the code will be capable of modeling the subcooled boiling phenomenon with a higher level of accuracy than previous numerical studies.

4.3. Governing equations

The governing equations used in the current Eulerian-Eulerian model are the incompressible mass conservation, momentum and energy equations. Mass conservation is expressed as

$$\frac{\partial \alpha_k}{\partial t} + \nabla.\left(\alpha_k \vec{U}_k\right) = \frac{\Gamma_{ki} - \Gamma_{ik}}{\rho_k}. \tag{4.1}$$

In this equation α_k is the void fraction, $\vec{U}_k$ is the velocity and ρ_k is the density for phase k, which can be either liquid (L) or gas (G). Γ_{ki} represents the mass transfer due to a phase change from phase k to phase i and Γ_{ik} is for the same phenomenon but from phase i to k. As a result, in the case of no phase change, these terms will drop out of the equation. The momentum equation is

$$\frac{\partial}{\partial t}\left(\alpha_k \vec{U}_k\right) + \nabla.\left(\alpha_k \vec{U}_k \vec{U}_k\right) = -\frac{\alpha_k}{\rho_k}\nabla p - \nabla.\left[\alpha_k(R_k + R_k^t)\right]$$

$$+ \alpha_k \vec{g} + \frac{\vec{F}_k}{\rho_k} + \frac{\Gamma_{ki}\vec{U}_i - \Gamma_{ik}\vec{U}_k}{\rho_k} \tag{4.2}$$

where ∇p is the gradient of the pressure in the flow, $\nabla.\,[\alpha_k(R_k + R_k^t)]$ is the viscous diffusion term, $\vec{g}$ is the gravitational force and $\vec{F}_k$ represents the interfacial forces occurring due to the movement of the bubbles in the liquid. The last term in equation (4.2) represents the evaporation and condensation effects on the momentum equation. The energy equation for the two-phase flow is

$$\frac{\partial((1-\alpha_i)h_k)}{\partial t} + \nabla.\left((1-\alpha_i)h_k\vec{U}_k\right) = -\frac{1}{\rho_k}\nabla.\,[(1-\alpha_i)(q_k + q_k^t)]$$

$$+\frac{(1-\alpha_i)}{\rho_k}\frac{Dp}{Dt} + \frac{\Gamma_{ki}h_i - \Gamma_{ik}h_k}{\rho_k} + \frac{\ddot{q}_w\ddot{A}_w}{\rho_k}(4.3)$$

where h_k is the specific enthalpy of phase k, q_k and q_k^t are the molecular and turbulent heat flux inside phase k, $\ddot{q}_w$ is the wall heat flux density and $\ddot{A}_w$ refers to the contact area with the wall per unit volume (Michta, 2011).

4.3.1. Interfacial forces

In the current study, which is an Eulerian-Eulerian simulation, the interaction between the continuous liquid phase and discrete bubble phase is considered in different ways. One of them is the effect of interfacial forces which are exerted on the bubbles by the liquid phase. According to Newton's third law, the total force acting on the bubbles by the liquid phase is equal to the total force exerted on the liquid phase by the bubbles. Due to the movement of bubbles in the liquid phase, different forces act on them. These forces can be represented in the following form:

$$\vec{F}_G = \vec{F}_G^D + \vec{F}_G^L + \vec{F}_G^{WL} + \vec{F}_G^{TD} + \vec{F}_G^{VM} \tag{4.4}$$

In this equation, $\vec{F}_G^D$ is the (gas) drag force, $\vec{F}_G^L$ is the lift force, $\vec{F}_G^{WL}$ describes the wall lubrication force, $\vec{F}_G^{TD}$ is the turbulent dispersion force and $\vec{F}_G^{VM}$ represents the virtual mass force. These forces are discussed in the following subsections.

4.3.1.1. Drag force

As shown in eqn. (4.4), the drag force $(\vec{F}_G^D)$ is one of the interfacial forces which the bubbles experience due to their movement in the liquid. This force is in opposite direction to the movement of the bubbles and is defined by the following equation:

$$\vec{F}_G^D = -\frac{3C_D}{4d_B}\rho_L\alpha_G|\vec{U}_G - \vec{U}_L|(\vec{U}_G - \vec{U}_L) \tag{4.5}$$

Here $|.|$ refers to the magnitude of the vector, d_B is the bubble diameter and C_D is the drag coefficient, which can be calculated from the correlation developed by Ishii and Zuber (1979),

$$C_D = \frac{24}{Re_b}\left(1 + 0.1Re_b^{0.75}\right) \tag{4.6}$$

where Re_b is the Reynolds number based on bubble diameter and the relative velocity between bubble and liquid.

4.3.1.2. Lift force

The lift force on the bubbles has a significant influence on their radial distribution. The general form for the lift force is based on the formula presented by Tomiyamaet al. (2002) and is written as:

$$\vec{F}_G^L = -C_L \rho_L \alpha_G (\vec{U}_G - \vec{U}_L) \times (\nabla \times \vec{U}_L) \tag{4.7}$$

In this equation, C_L is the lift coefficient and can be determined using the correlation

$$C_L = \begin{cases} \min[0.288\tanh(0.121\text{Re}_b), f(\text{Eo}_d)] & \text{if Eo}_d < 4 \\ f(\text{Eo}_d) & \text{if } 4 \leq \text{Eo}_d \leq 10 \\ -0.27 & \text{if Eo}_d > 10 \end{cases} \tag{4.8}$$

where

$$f(\text{Eo}_d) = 0.00150\text{Eo}_d^3 - 0.0159\text{Eo}_d^2 - 0.0204\text{Eo}_d + 0.474 \tag{4.9}$$

This coefficient depends on the modified Eotvos number, given by

$$\text{Eo} = \frac{g(\rho_L - \rho_G)D_s^2}{\sigma} \tag{4.10}$$

where σ is the surface tension of the liquid and D_s is the maximum horizontal dimension of the bubble, which is calculated using the following equation by Wellek et al. (1966):

$$D_s = d_B(1 + 0.163\text{Eo}^{0.757})^{0.33} \tag{4.11}$$

4.3.1.3. Wall lubrication force

In two-phase flow there is another interfacial force which pushes the bubbles away from the wall. The force which is responsible for this wall peaking phenomenon is called the wall lubrication force ($\vec{F}_G^{WL}$). The calculation of this force in the current model is based on the correlation presented by Tomiyama (1998),

$$\vec{F}_G^{WL} = -0.5 C_{WL} \rho_L \alpha_G d_B \left(\frac{1}{y^2} - \frac{1}{(D-y)^2}\right)(|\vec{U}_G - \vec{U}_L|)^2 \vec{n} \tag{4.12}$$

$$C_{WL} = \begin{cases} e^{-0.933 Eo + 0.179} & \text{if } 1 \leq Eo \leq 5 \\ 0.00599 Eo - 0.0187 & \text{if } 5 \leq Eo \leq 33 \\ 0.179 & \text{if } Eo > 33 \end{cases} \tag{4.13}$$

Here C_{WL} is the wall lubrication force coefficient, D is the pipe diameter, $\vec{n}$ is the unit vector normal to the wall and y is the distance to the wall. Unlike the Michta (2011) model, which considered only the Tomiyama (1998) correlation for this force, in the current study the correlation of Frank (2005), which is geometry independent, is implemented in the code.

4.3.1.4. Turbulent dispersion force

The interfacial turbulent dispersion force is responsible for the effect of turbulent fluctuations of liquid velocity on the gas phase and plays a major role in the radial distribution of the bubbles. Burns et al. (2004) have proposed the following correlation for estimating this force:

$$\vec{F}_G^{TD} = -\frac{3C_D}{4d_B}\frac{\mu\alpha_L}{\sigma^{TD}}\rho_l|\vec{U}_G - \vec{U}_L|(\frac{1}{\alpha_L} + \frac{1}{\alpha_G})\nabla\alpha_G \qquad (4.14)$$

where $\sigma^{TD} = 0.9$ is an empirical parameter.

4.3.1.5. Virtual mass force

The virtual mass force or added mass force ($\vec{F}_G^{VM}$) is generated due to the relative acceleration of one phase with respect to the other. The correlation proposed by Zuber (1964) is used for modeling the added mass force in the current study, i.e.,

$$\vec{F}_G^{VM} = -0.5\rho_L\alpha_G\frac{1+2\alpha}{1-\alpha}(\frac{D\vec{U}_G}{Dt} - \frac{D\vec{U}_L}{Dt}) \qquad (4.15)$$

4.3.2. Boiling model

The wall boiling phenomenon is modeled by the RPI boiling model of Kurul and Podowski (1991). According to the RPI model, the total heat flux from the wall to the liquid is partitioned into three components, namely the convective heat flux, the quenching heat flux, and the evaporative heat flux, written as

$$Q_{total} = Q_C + Q_Q + Q_E. \qquad (4.16)$$

The heated wall surface is subdivided into an area A_b, which is the area covered by nucleating bubbles, and a portion $(1-A_b)$, which is the area covered by the fluid. The convective heat flux Q_C is expressed as

97

$$Q_C = h_C(T_W - T_L)(1 - A_b) \tag{4.17}$$

where h_C is the single phase heat transfer coefficient, and T_W and T_L are the wall and liquid temperatures, respectively. The evaluation of A_b is based on the departure diameter of the bubbles (d_B) and also the site density (N_w) using the following equation:

$$A_b = \pi N_w (a d_B^2/2)^2 \tag{4.18}$$

where a is the bubble influence factor, for which a value of 2 is used (Kurul and Podowski, 1991). The site density of bubbles (N_w) depends on different parameters such as the material properties and wall superheat ($\Delta T_{sup} = T_W - T_{sat,L}$), which is the temperature difference between the wall and the saturation temperature of the liquid. Lemmert and Chawla (1977) proposed the following equation for determining the site density of bubbles:

$$N_w = N_{ref}[(T_W - T_L)/(\Delta T_{refN})]^P \tag{4.19}$$

where $N_{ref} = 0.8 \times 10^6$ m^{-2} and $\Delta T_{refN} = 10K$, based on the recommendation of Bartolomej and Chanturiya (1967). The bubble detachment (or departure) diameter has a significant influence on the modeling of the subcooled boiling phenomenon. In the current study, for high subcooling cases ($\Delta T_{sub} = T_{sat,L} - T_L$), the experimental correlation of Unal (1976) is used for calculating the bubble detachment diameter, which is expressed as:

$$d_B = 2.42 \times 10^{-5} P^{0.705} a/\sqrt{b\varnothing} \tag{4.20a}$$

where P is the system pressure (Pa) and a, b and ∅ are experimental correlations defined in Unal (1976). For low subcooling cases (less than 2K) the Tolubinsky and Kostanchuk (1970) correlation is used and expressed as:

$$d_B = d_{ref} e^{\left(-\frac{T_{sat} - T_L}{\Delta T_{refd}}\right)} \tag{4.20b}$$

where d_{ref} is 0.6 mm and $\Delta T_{refd} = 45K$ (Krepper et al. 2007). Note that the current model is capable of evaluating different subcooling temperatures and automatically selects the proper experimental correlation for this purpose. The quenching heat flux (Q_Q) models the averaged transient energy transfer related to liquid filling the wall vicinity after bubble detachment, and is expressed by the following equation (Krepper and Rzehak, 2011):

$$Q_Q = A_b h_Q (T_W - T_L) \tag{4.21}$$

The quenching heat transfer coefficient h_Q is calculated based on the formula presented by Mikic and Rohsenow (1969):

$$h_Q = \frac{2}{\sqrt{\pi}} f \sqrt{t_w \rho_L k_L C_{pL}} \tag{4.22}$$

where k_L is the thermal conductivity of the liquid phase and C_{pL} is the specific heat of the liquid. The bubble detachment frequency (f) is given according to the formula presented by Cole (1960):

$$f = \sqrt{\frac{4g(\rho_L - \rho_G)}{3C_D d_B \rho_L}}. \tag{4.23}$$

In equation (4.22), t_w is the waiting time between the bubble departure and the appearance of the next bubble at the same spot and is set equal to $0.8f^{-1}$ as suggested by Kurul and Podowski (1990, 1991). The evaporation heat flux (Q_E) can be estimated via the evaporation mass flux at the wall,

$$Q_E = \dot{m}_W \left(h_{sat,L} - h_L \right) \tag{4.24}$$

Here, the generated vapor mass $\dot{m}_W$ is expressed as a function of bubble diameter at detachment (d_B), bubble generation frequency (f) and nucleation site density (N_w),

$$\dot{m}_W = \frac{\pi}{6} d_B^3 \rho_G f N_w. \tag{4.25}$$

4.3.2.1. Phase change rates

The evaporation of the liquid phase occurs at the wall where T_W exceeds the $T_{sat,L}$ of the liquid in its proximity. The evaporation rate (Γ_{ki}) can be determined using the following equation which is expressed in unit per volume (Yao and Morel, 2004):

$$\Gamma_{ki} = \frac{\pi}{6} d_B^3 \rho_G f N_w A_s \tag{4.26}$$

where A_s is the surface area of the wall per unit volume. The saturated bubbles move away from the wall and come in contact with the bulk of the fluid which is at lower temperature. This causes the vapor to condensate. The condensation rate can be calculated using the equation (Michta, 2011):

$$\Gamma_{ik} = \frac{h_{ii} \Delta T_{sub} \ IAC}{h_G - h_L} \tag{4.27}$$

where h_{ii} is based on the correlation by Wolfert et al. (1978) and IAC is the interfacial area concentration which is discussed in the next section. Figure 4.1 presents the flowchart of the boiling model developed in the current study, including the sequence of calculations and algorithm loops.
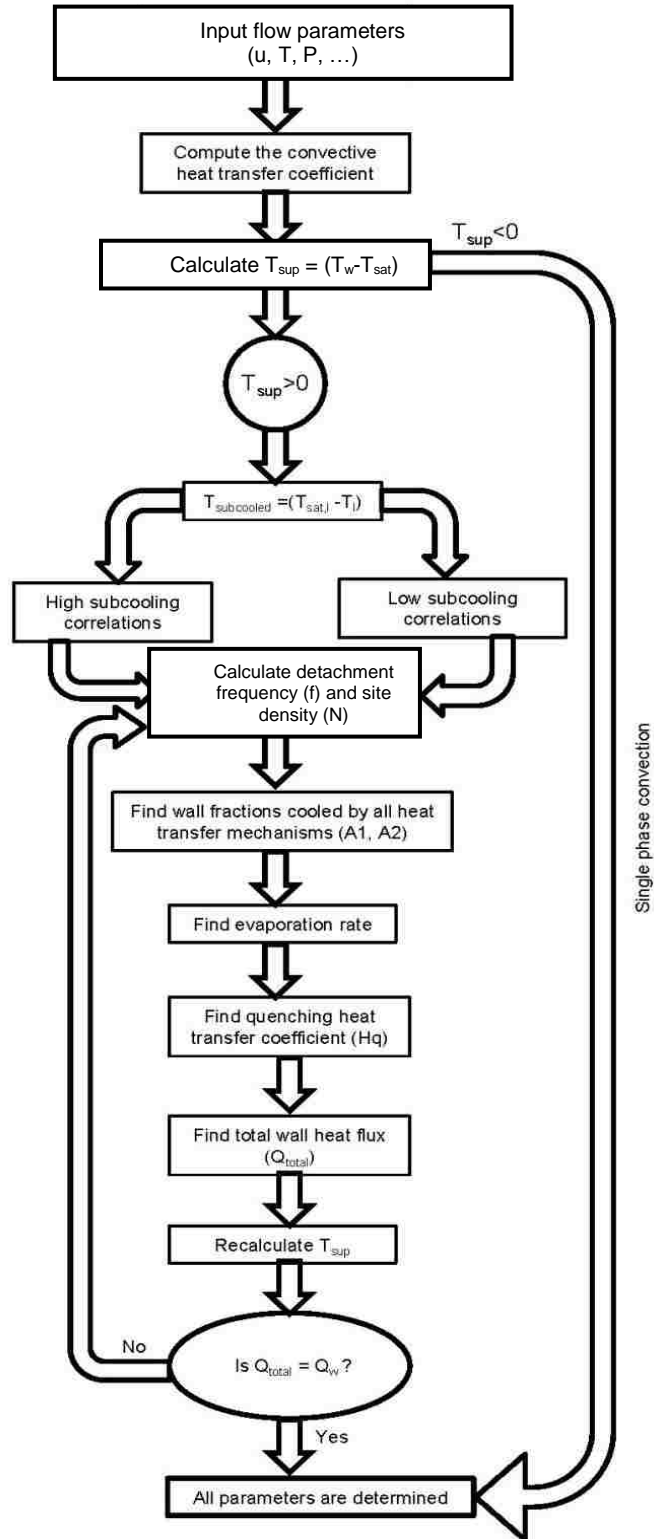
Fig. 4.1 Boiling model algorithm

4.3.3. Interfacial area concentration

The interfacial area concentration (IAC) accounts for the changes in the surface area of the bubbles. During bubble generation and movement, a number of phenomena can occur including change in shape and size, breakup and coalescence. To take all of these effects into consideration, the transport equation for the interfacial area concentration (IAC) is solved and linked to the mass, momentum and energy equations. The IAC equation solved in this study is the one proposed by Yao and Morel (2004):

$$\frac{\partial(IAC)}{\partial t} + \nabla.\left((IAC)\vec{U}_G\right) = \frac{2(IAC)}{3\alpha_G\rho_G}\dot{m}_{LG} + 12\pi(\frac{IAC}{\alpha_G})^2(\emptyset^C + \emptyset^B) + \pi d_w^2 \emptyset^{nuc} \tag{4.28}$$

where $\emptyset^C$ and $\emptyset^B$ represent the effect of bubble coalescence and breakup, respectively, and $\emptyset^{nuc} = fN_w A_s$ takes into account the effect of boiling on the IAC. There are different experimental correlations in the literature to determine the effect of bubble breakup and coalescence. In the current study the model developed by Hibiki and Ishii (2002) was chosen and applied to the IAC equation,

$$\emptyset^C = -\Gamma_C \frac{\alpha^2 \varepsilon^{1/3}}{d_B^{11/3}(\alpha_{max} - \alpha)} \exp\left(-K_C \frac{d_B^{11/3}\rho_L^{1/2}\varepsilon^{1/3}}{\sigma^{1/2}}\right) \tag{4.29}$$

where $\Gamma_C = 0.031$ and $K_C = 1.29$, and

$$\emptyset^B = \Gamma_B \frac{\alpha(1-\alpha)\varepsilon^{1/3}}{d_B^{11/3}(\alpha_{max} - \alpha)} \exp\left(-K_B \frac{\sigma}{d_B^{5/3}\rho_L^{1/2}\varepsilon^{2/3}}\right) \tag{4.30}$$

where $\Gamma_B = 0.021$ and $K_B = 1.37$.

An example of the implementation of the IAC, breakup and coalescence models in OpenFOAM is presented in Fig. 4.2.

```
    scalar alphaMax = 0.52;
    scalar GammaB = 0.0209;
    scalar GammaC = 0.0314;
    scalar Kb = 1.37;
    scalar Kc = 1.29;

//////////////////////////////////////////////////////////////////////////
//coalescence model
//////////////////////////////////////////////////////////////////////////

    volScalarField sourceRCa = -GammaC*pow(alpha,2.0)*pow(epsilon,1.0/3.0);
    volScalarField sourceRCb = pow(DS+plusIG,11.0/3.0)*(alphaMax-alpha);
    volScalarField sourceRCc = exp(-Kc*pow(rhob,1.0/2.0)
*pow(DS+plusDS,5.0/6.0)*pow(epsilon,1.0/3.0)/pow(sigma,1.0/2.0));
    volScalarField sourceRC1 = sourceRCa/sourceRCb*sourceRCc;
    volScalarField sourceRC = sourceRC1*scalar(1.0);

//////////////////////////////////////////////////////////////////////////
//breakup model
//////////////////////////////////////////////////////////////////////////

    volScalarField sourceTIa = GammaB*alpha*(1.0-
alpha)*pow(epsilon,1.0/3.0);
    volScalarField sourceTIb = pow(DS+plusDS,11.0/3.0)*(alphaMax-alpha);
    volScalarField sourceTIc = exp(-Kb*sigma/rhob/pow(DS+plusDS,5.0/3.0)
                      /pow(epsilon,2.0/3.0));
    volScalarField sourceTI1 = sourceTIa/sourceTIb*sourceTIc;
    volScalarField sourceTI = sourceTI1*scalar(1.0);
        surfaceScalarField phiMix = phi;
        surfaceScalarField phiRel = phia - phib;

//////////////////////////////////////////////////////////////////////////
// interfacial area concentration transport equation
//////////////////////////////////////////////////////////////////////////
fvScalarMatrix IACEqn(IAC,IAC.dimensions()*dimVol/dimTime);
{
    IACEqn=
    (
      (
       fvm::ddt(IAC)
       +fvm::div(phiMix,IAC,"div(phiMix,IAC)")
       +fvm::div(-fvc::flux(-phiRel, beta,
"div(phiRel,IAC)"),IAC,"div(phiRel,IAC)")
      )
        ==36.0*3.14/3.0*pow((alpha+
        scalar(1e-12))/IAC,2.0)*(sourceRC+sourceTI)
       +2.0/3.0*IAC/(alpha+scalar(1.0e-8))/rhoa*(-GammaLG)
       +3.1415*DM*DM*freq*ASD*sfPerVol
    );
        IACEqn.relax();
        IACEqn.solve();
}
IAC = max(IAC,smallIAC);
DS = 6*alpha/IAC;
```

Fig. 4.2 Implementation of breakup, coalescence and IAC equation in OpenFOAM

4.3.4. Turbulence modelling

Liquid phase turbulence simulation is carried out by implementing the standard k - ε turbulence model with additional terms representing the effect of gas bubbles. The effect of the liquid phase turbulence on the bubbles was modeled using the turbulent dispersion force described earlier in section 4.3.1.4. The total viscosity in a single phase flow is calculated from a molecular part (μ^{mol}) in addition to the turbulent viscosity part (μ^{turb}). The turbulent viscosity (μ^{turb}) is defined in equation (4.31). In this equation, k is the turbulent kinetic energy, ε is the turbulent eddy dissipation and $C_\mu = 0.09$,

$$\mu^{turb} = C_\mu \rho_L \frac{k^2}{\varepsilon}. \tag{4.31}$$

4.3.4.1. Bubble induced turbulence

Sato et al. (1981) suggested the following equation to consider the effect of bubbles on liquid phase turbulence:

$$\mu^{bubble} = C_B \rho_L \alpha d_B \left| \vec{U}_G - \vec{U}_L \right| \tag{4.32}$$

where $C_B = 0.6$. The total viscosity for the two-phase flow is calculated from a molecular part (μ^{mol}), the turbulent viscosity (μ^{turb}) and the bubble induced contribution (μ^{bubble}) as shown in Fig. 4. 3., i.e.,

$$\mu = \mu^{mol} + \mu^{turb} + \mu^{bubble}. \tag{4.33}$$

```
if (turbulence)
{
    if (mesh.changing())
    {
        y.correct();
    }
    tmp<volTensorField> tgradUb = fvc::grad(Ub);
    volScalarField G(2*nutb*(tgradUb() && dev(symm(tgradUb()))));
    tgradUb.clear();
    #include "wallFunctions.H"
    // Dissipation equation
    fvScalarMatrix epsEqn
    (
        fvm::ddt(beta, epsilon)
      + fvm::div(phib, epsilon)
      - fvm::laplacian
        (
            alphaEps*nuEffb, epsilon,
            "laplacian(DepsilonEff,epsilon)"
        )
      ==
        C1*beta*G*epsilon/k
      - fvm::Sp(C2*beta*epsilon/k, epsilon)
    );
    #include "wallDissipation.H"
    epsEqn.relax();
    epsEqn.solve();
    epsilon.max(dimensionedScalar("zero", epsilon.dimensions(), 1.0e-
15));
    // Turbulent kinetic energy equation
    fvScalarMatrix kEqn
    (
        fvm::ddt(beta, k)
      + fvm::div(phib, k)
      - fvm::laplacian
        (
            alphak*nuEffb, k,
            "laplacian(DkEff,k)"
        )
      ==
        beta*G
      - fvm::Sp(beta*epsilon/k, k)
    );
    kEqn.relax();
    kEqn.solve();
    k.max(dimensionedScalar("zero", k.dimensions(), 1.0e-8));
    //- Re-calculate turbulence viscosity
    nutb = Cmu*sqr(k)/epsilon;
    #include "wallViscosity.H"
}
nuEffb = nub + nutb+1.2*DS/2.0*alpha*magUr;
```

Fig. 4.3 k - ε turbulence model, modified to account for gas bubbles

4.4. Results

The code development procedure includes three stages. In the first stage, an adiabatic two-phase flow model has been developed which does not solve the energy equation. The second step of the model development process includes adding the energy equation to the solver and enabling the boiling model. The last stage includes extending the boiling model to an impinging jet flow. Validation of the code has also proceeded in stages, first testing the adiabatic model, followed by the boiling model for pipe flow, then jet impingement boiling.

4.4.1. Evaluation of adiabatic case

Initially, modeling of the interfacial forces and the Interfacial Area Concentration (IAC) transport equation were added to the solver. This gives the code the capability of predicting changes in the size of the bubbles due to breakup and coalescence (Fig. 4.2). The current model includes several improvements compared to the model developed by Michta (2011). The Frank (2005) correlation for wall lubrication force was added to the solver, enabling the user to apply this force to other flow geometries. A 2D axisymmetric mesh, instead of a 2D planar rectangular mesh which was employed by Michta (2011), was used for the current simulation. A slip condition was imposed for bubbles on the wall, whereas Michta (2011) used a no-slip condition.

This part of the solver, which is referred to as the adiabatic part, does not take into account the heat transfer phenomenon or any phase change.

107

To evaluate the accuracy of the code and to ensure that the developed model at this stage generates satisfactory results, the DEDALE1101 experiment (Grossetête, 1995) was modeled using the modified version of OpenFOAM. The model geometry is a pipe (Fig. 4.4a) with 6 m length and diameter D = 0.0381 m. A uniform 2D axisymmetric mesh shown in Fig. 4.4b was generated for this flow field, with the axis of the pipe aligned along the x-axis. The mesh is comprised of 20 cells in the radial direction and 300 cells in the streamwise direction. The number of cells selected in each direction is based on mesh convergence tests.

D= 0.0381m
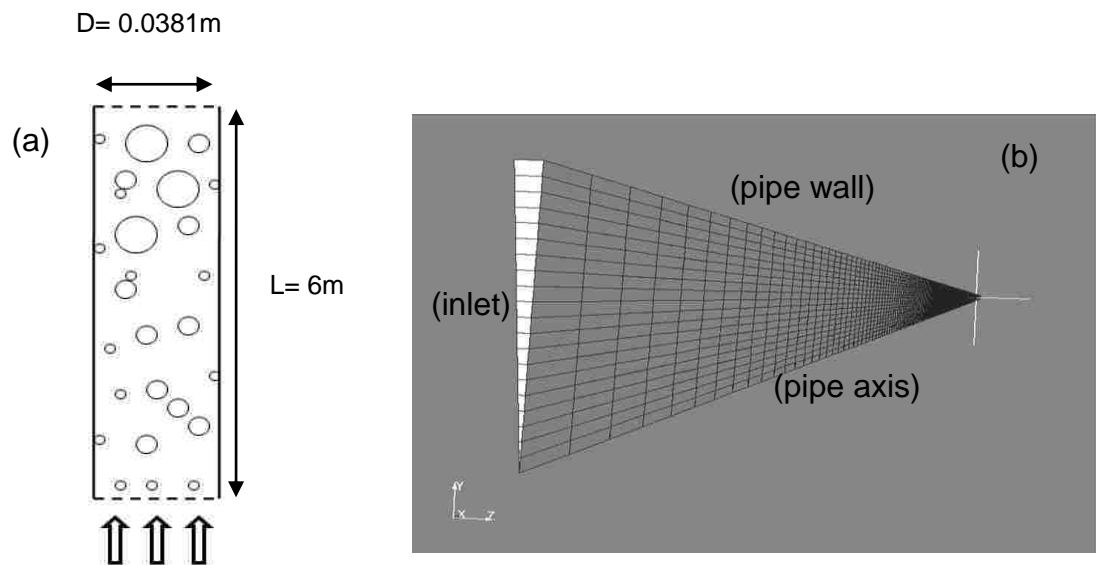
Fig. 4.4 a) Schematic of a two-phase pipe flow (not to scale), b) 2D axisymmetric mesh

The initial and boundary conditions used in this simulation were matched with the experimental setup. A liquid velocity of 0.91 m/s and a gas velocity of

1.36 m/s were introduced at the inlet. The inlet turbulent kinetic energy and dissipation rate obtained from the experiments were 0.00423 m^2/s^2 and 0.01695 m^2/s^3, respectively. Values of 97 m^{-1} for the interfacial area concentration and 0.048 for the void fraction were set at the inlet location. The no-slip condition was used at the wall for the liquid phase. For the gas phase, a slip condition was used. A pressure outlet condition was used at the outlet. Due to the 2D axisymmetric nature of the simulation, the pipe axis was taken as a computational boundary, on which a symmetry condition was imposed. Simulations were run until negligible change was observed in the pressure difference between the inlet and outlet of the domain.

Figure 4.5 illustrates the results on the cross-section at x/D = 55, i.e. about 1/3 of the pipe length, and compares these results obtained from the current model with DEDALE experimental data (Grossetête, 1995) and the numerical results of Michta et al. (2012) and Yao and Morel (2004). Figure 4.5a demonstrates that there is very good agreement between the IAC results obtained from the current study and the experiment. In particular, the current simulation predicts the correct IAC peak value and yields a good prediction of the peak IAC location in the wall proximity. The difference between the predicted and experimental location of the peak IAC near the pipe wall is less than 6%, while Michta et al. (2012) show a difference of about 17% and Yao and Morel (2004) is unable to capture the peak.

The radial distribution of void fraction is plotted in Fig. 4.5b. Similar to the behaviour observed in the IAC profile, the void fraction profile obtained from the

current model captures the peak location and peak value of the void fraction in the proximity of the wall. In regions close to the pipe axis, the computational model accurately predicts the void fraction profile, as does the model of Michtaet al. (2012). The Yao and Morel (2004) results follow the trend of the experimental data at the middle region of the pipe, but cannot capture the correct behaviour in the wall region.

Further evaluation of the model is carried out by comparing the liquid velocity at x/D = 55. The numerical results for the liquid velocity shown in Fig. 4.5c indicate an error of about 10% compared to the experimental values. Considering the assumptions of the model, the discretization errors in the numerical scheme and the uncertainties associated with the measurements, this level of discrepancy seems to be acceptable.

Comparison of the mean bubble diameter results predicted by the current model and previous numerical simulations with the experimental data shows that the current model generates satisfactory results in the middle region of the pipe. In the wall region, the results of Michta et al. (2012) are slightly closer to the experimental results, and neither simulation predicts the increase in mean bubble diameter.

The improvement observed in the current numerical results is likely due to incorporating a different mesh topology than Michta et al. (2012) and the use of a different boundary condition for the bubbles on the wall boundary. Michtaet al. (2012) used a no-slip condition on the wall for the bubbles. In the current

simulation a slip condition, which is a more realistic assumption for bubble movement, is used to allow bubbles to freely slide on the wall. A 2D axisymmetric mesh was employed here, instead of the 2D planar mesh which was used by Michta et al. (2012). Proper implementation of all equations and correlations has been investigated carefully in the current model. The inaccuracy of the experimental results due to the associated measurement uncertainties at the wall proximity should also be taken into consideration.
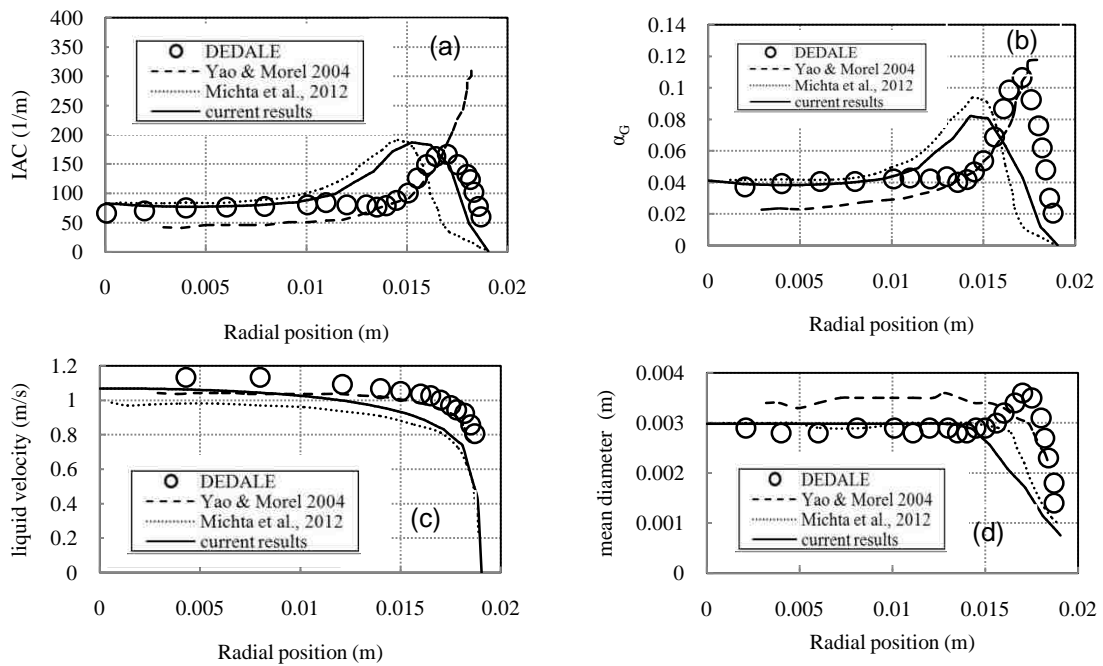
Fig. 4.5 Radial distribution of a) interfacial area concentration, b) void fraction, c) liquid velocity, d) bubble diameter

Based on the evaluations discussed above, the adiabatic part of the model appears to generate satisfactory results. Overall, the present results are an

improvement over the previous numerical results of Michta (2011) and Yao and Morel (2004). Therefore, we can confidently proceed to the next step, which is to activate the energy equation and enable the boiling model in the code.

4.4.2. Evaluation of boiling model

Similar to the adiabatic test case, an appropriate experiment was chosen to evaluate the boiling model. The DEBORA experiment (Garnier et al. 2001) was selected as a benchmark in this case. Unlike the DEDALE experiment, the DEBORA experiment involved two-phase flow with phase change. Therefore, to test the model developed in this research, a simulation was designed to match the geometry and boundary conditions of the DEBORA experimental setup (Fig 4.6). A vertical pipe with a diameter of 0.0192 m and heated length of 3.5 m was modeled. Subcooled Freon-12 (R12) was supplied at the inlet. Due to the heat flux on the pipe, bubbles start to form along the pipe wall and travel with the flow towards the exit of the pipe.

Similar to the adiabatic case, a 2D axisymmetric mesh with 20 cells in the radial direction and 300 cells in the streamwise direction was used. Liquid velocity of 1.7 m/s and gas velocity of 1.9 m/s were supplied at the inlet. To match the experimental setup, the IAC value was set to be 5000 at the inlet. Turbulent kinetic energy and dissipation rate were obtained from the experiments and set to be 0.114 m^2/s^2 and 0.149 m^2/s^3, respectively. Zero velocity and a no penetration condition were applied on the wall for the liquid phase. Unlike the no-

slip condition used by Michta (2011) for the bubble velocity on the wall, a slip condition was used in the current simulation. A pressure outlet condition was used at the outlet. The inlet temperature of the liquid phase was set at 68.5°C and a heat flux of 73,890 W/m^2 was imposed on the pipe.
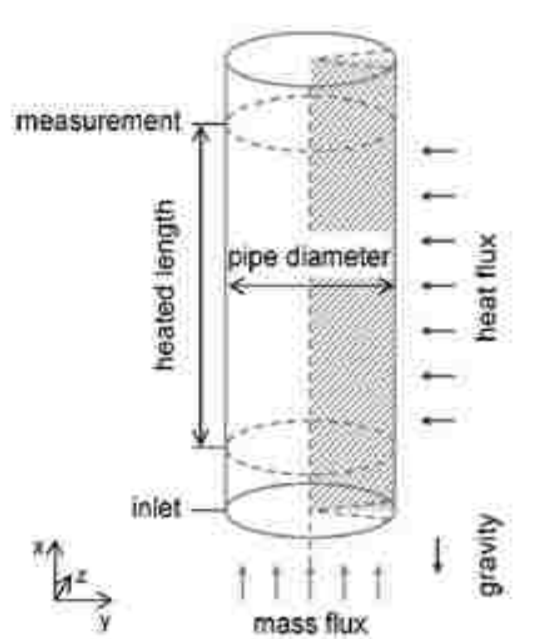
Fig. 4.6 Sketch of the DEBORA test setup (Garnier et al. 2001)

Due to the heat flux on the wall, the temperature of the liquid phase passing through the pipe increases over time. This increase continues until the liquid temperature reaches the saturation temperature in the proximity of the wall. At this stage small bubbles begin to form on the wall. As time progresses, these bubbles are convected downstream with the fluid.

In order to evaluate the accuracy of the boiling model and compare it with previous studies, several parameters including the radial temperature distribution

113

of the liquid, the void fraction, the IAC and the mean bubble diameter were extracted at the exit of the pipe. Figure 4.7a shows a comparisonof the temperature profiles obtained from the current CFD simulation, the experimental measurements and other numerical results. As the graph shows, there is good agreement between the current and experimental results. The current results show a small improvement over the results obtained by Michta (2011).

Figure 4.7b shows that the boiling model is capable of capturing the trend of the experimental IAC values over a significant portion of the pipe radius, especially in the near-wall region. The radial distribution of void fraction (Fig. 4.7c) is better predicted by the current CFD model compared to the previous numerical results of Michta (2011), although neither compares well to the experimental data. Figure 4.7d illustrates a comparison of the mean bubble diameter obtained from the different simulations and shows very good agreement between the results obtained from the current simulation and the experimental results. A significant improvement also can be seen in the results relative to the numerical simulations of Michta (2011). The analysis of these results suggests the validity of the numerical model for the simulation of boiling heat transfer in a pipe flow.
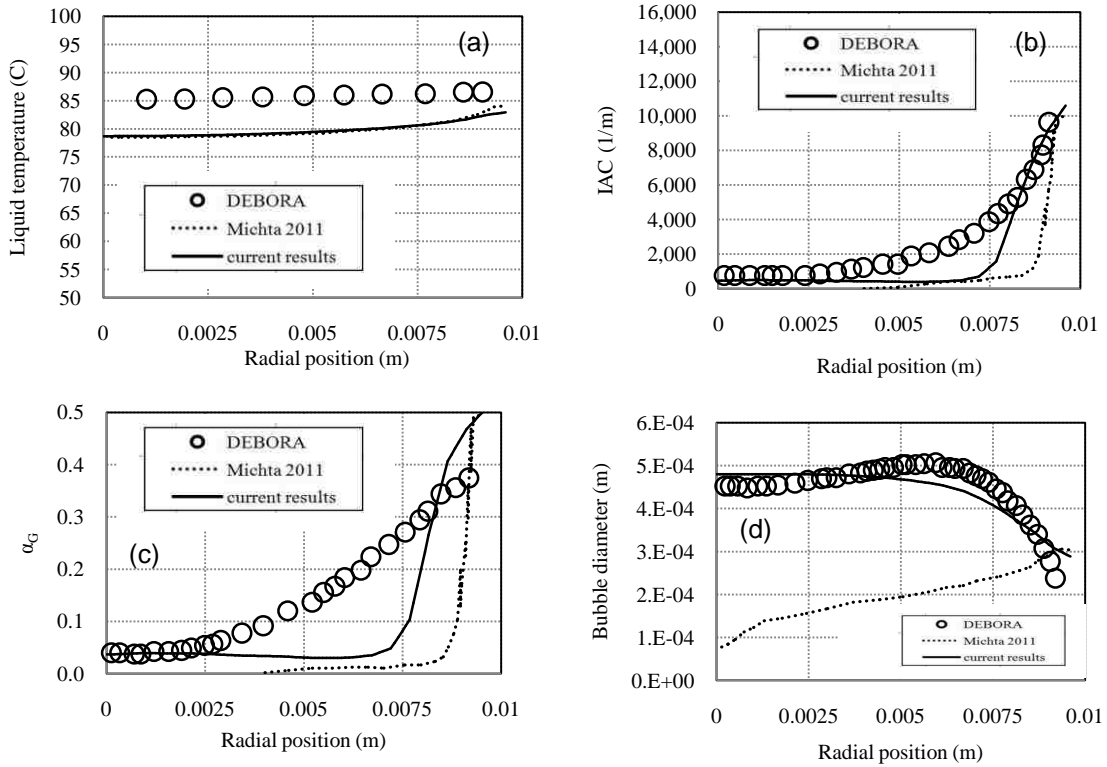
Fig. 4.7 Radial distribution of a) liquid temperature, b) interfacial area concentration, c) void fraction, d) bubble diameter

4.4.3. Boiling simulation in an impinging jet

The boiling model developed in the previous section is only applicable to flow through a circular pipe. However, it is of interest to extend the boiling model to an impinging jet. Boiling liquid jets benefit from the latent heat of vaporization of the fluid to remove large amounts of heat (>20,000 W/m^{2}K) from a surface (Narumanchi et al. 2008). This makes boiling an interesting phenomenon for an electronics cooling process. As illustrated in Fig 1.4, a small increase in T_{sup} in

the nucleate boiling part of the curve is accompanied by a large increase in the amount of heat flux (q") removed from the surface.

To make the boiling model of the pipe flow applicable to an impinging jet, a number of additional modifications are required. The following is a listing of the modifications applied to the boiling model developed in this research.

4.4.3.1. Lift force

The lift force formula of Tomiyama et al. (2002) used above (Section 4.3.1.2) is only valid for pipe flow. Here, the correlation suggested by Moraga et al. (1999) is used for the impinging jet:

$$C_L = \begin{cases} 0.0767 & \text{if } \varphi \leq 6000 \\ -\left(0.12 - 0.2e^{-\frac{\varphi}{36000}}\right)e^{\frac{\varphi}{3e+7}} & \text{if } 6000 \leq \varphi \leq 1.9e+05 \\ -0.002 & \text{if } \varphi \geq 1.9e+05 \end{cases} \qquad (4.34)$$

where $\varphi = \text{Re}_b \text{Re}_v$. In this equation $\text{Re}_b = d_B |\vec{U}_G - \vec{U}_L|/\nu_L$ and $\text{Re}_v = d_B^2 |\nabla \times \vec{U}_L|/\nu_L$, where ν_L is the liquid viscosity.

4.4.3.2. Wall lubrication force

Unlike the Tomiyama (1998) correlation used for the pipe flow, the correlation of Frank (2005), which is geometry independent, was employed in the code for the impinging jet model:

$$\vec{F}_G^{WL} = -C_{WLf}\rho_L\alpha\left(\left|(\vec{U}_G - \vec{U}_L) - ((\vec{U}_G - \vec{U}_L).\vec{n})\vec{n}\right|\right)^2\vec{n} \qquad (4.35)$$

$$C_{WLf} = C_{WL} \cdot \max\left\{0, \frac{(1 - \frac{y_w}{10\,d_B})}{6.8 y_w \left(\frac{y_w}{10\,d_B}\right)^{0.7}}\right\} \qquad (4.36)$$

where C_{WL} can be determined from equation (4.11).

4.4.3.3. Validation of the boiling model for impinging jet

An appropriate experiment was chosen to evaluate the boiling model developed for impinging jets. The experiment carried out by Katto and Kunihiro (1973) was selected as a benchmark and a simulation was designed to match the geometry and boundary conditions of the experimental setup (Fig. 4.8).
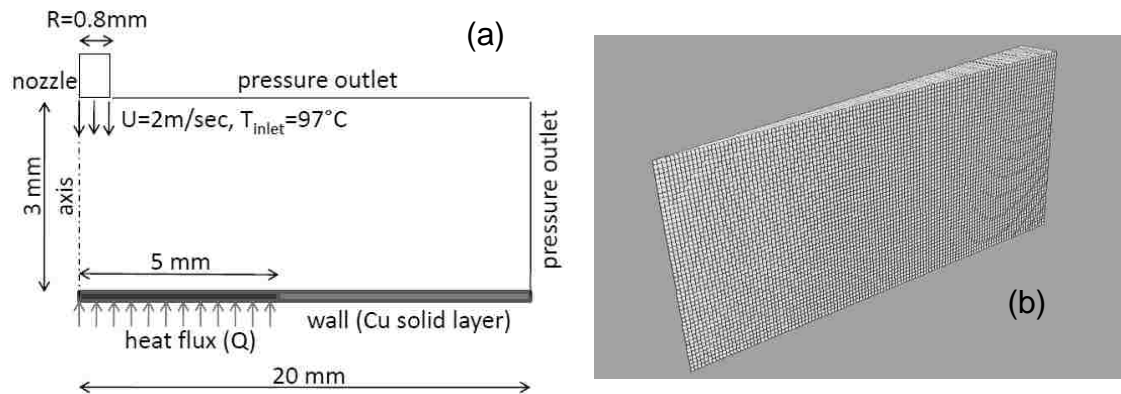
Fig. 4.8a) Computational domain, b) mesh for the impinging jet

A water jet with 3°C subcooling at atmospheric pressure (i.e., with T_{inlet} = 97°C) impinges on a 10 mm diameter disk with an inlet velocity of 2 m/s. The nozzle diameter is 1.6 mm, and the distance between the nozzle exit and the heated plate is maintained at 3 mm (H/D = 1.87). A heat flux is imposed on the

117

hotplate surface, as shown in Fig. 4.8a. Due to the heat flux on the plate, bubbles form on the wall and travel with the flow towards the exit of the domain.

A 2D axisymmetric mesh was built for the simulation (Fig. 4.8b). Zero velocity and a no penetration condition were applied on the wall for the liquid phase. A periodic boundary condition was used for the two side boundaries. For the bubble velocity on the wall, a slip condition was imposed. A pressure outlet condition was used at the outlet. The k - ε model with a standard wall function modified for the current study was used for turbulence modeling.

Fig. 4.9 shows the comparison of the boiling curve, which is a plot of heat flux vs. stagnation point wall superheat, obtained from the current CFD simulation, the numerical results of Narumanchi et al. (2008) and the experimental measurements of Katto and Kumihiro (1973). As seen in Fig. 4.9 there is fair agreement between the results obtained from the current simulation and the experiments, witha difference of about 20%. Given the complex nature of this problem and the experimental uncertainties, differences of the order of even 30% have been deemed acceptable (Narumanchi et al. 2008). This evaluation confirms that the current boiling model is capable of simulating boiling heat transfer in impinging jets.
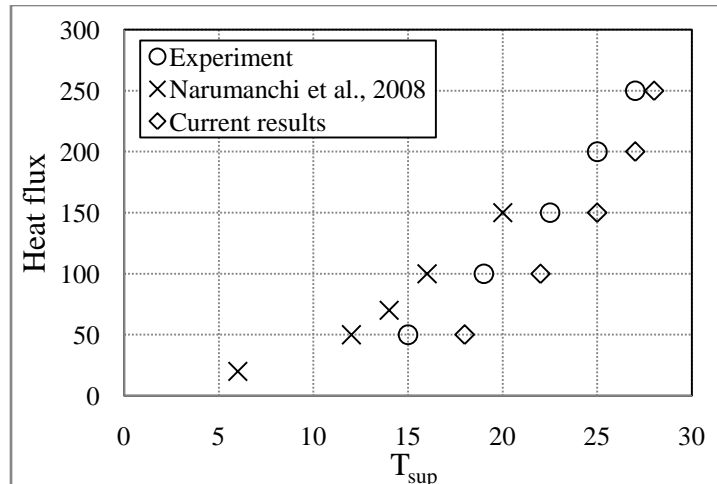
Fig. 4.9 Boiling curve obtained from current CFD analysis, simulation of Narumanchi et al. (2008) and experiment of Katto and Kunihiro (1973)

4.4.3.4. Results

Figure 4.10 shows the liquid velocity vectors and velocity magnitude contours obtained from the current impinging jet simulation. After the impingement the flow turns to the radial direction and a wall jet is formed on the plate.
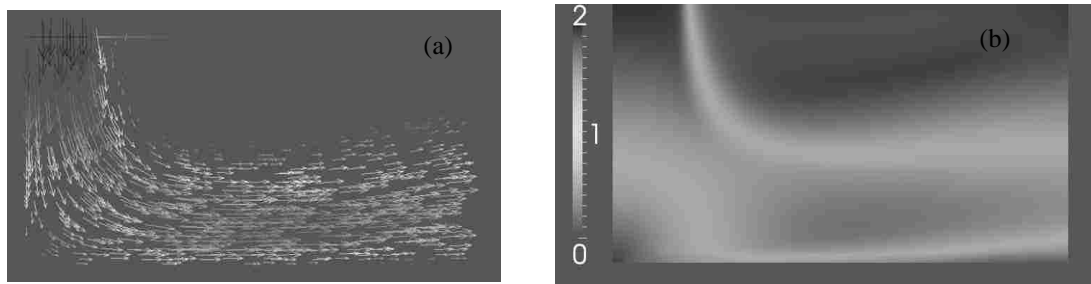
Fig. 4.10 Liquid a) velocity vectors, b) velocity magnitude contours

Figure 4.11 shows different flow parameters for the impinging jet with a heat flux of 100,000 W/m^2. The profiles of IAC and void fraction are plotted in Figs. 4.11a,b. A thicker profile and a higher peak can be observed as radial distance from the jet axis increases. This is due to the generation of more bubbles in regions far from the axis. Basically, the cooling effect of the impinging jet on the plate is weakened as the radial distance increases which is associated with more bubble generation in that region, i.e., an increase in IAC and void fraction.
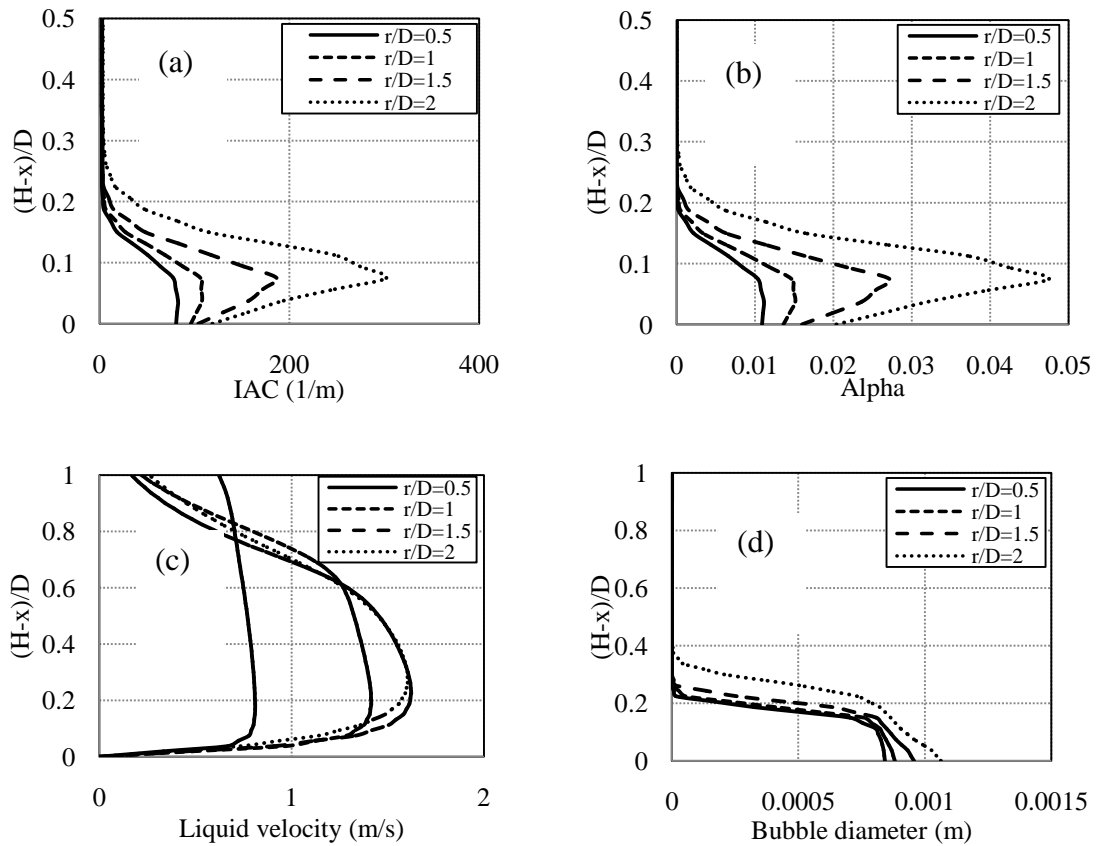
Fig. 4.11 Profiles at different radial stations; a) IAC, b) void fraction, c) liquid velocity, and d) bubble diameter

Fig. 4.11c plots the liquid velocity profiles for the same radial stations shown in Figs. 4.11a,b. This figure shows that the wall jet is approaching a fully developed condition as the radial distance increases. The bubble size profiles are shown in Fig. 4.11d for the same r/D stations. An increasing trend is observed for these profiles by moving towards the downstream region.

4.5. Concluding remarks

An Eulerian-Eulerian model has been developed to simulate the boiling heat transfer phenomenon in a pipe flow and in an impinging jet. The OpenFOAM software was used for developing the code. The default solver "twoPhaseEulerFoam" was modified to include boiling heat transfer.

The model development procedure is divided into three stages. In the first step, which is the adiabatic portion, the OpenFOAM default two-phase flow model was enhanced to take into account several aspects of two-phase flow phenomena, including most of the interfacial forces between the liquid and the bubbles, and the breakup and coalescence of the bubbles. In this regard, the code was modified to account for the effect of drag, lift, wall lubrication, turbulent dispersion and added mass forces. Then the transport equation for the interfacial area concentration (IAC) parameter, which is responsible for the change in bubble shape, was added to the code. Different mesh topologies, boundary conditions and experimental correlations were considered to improve the quality of the results. An experimental test case was selected to evaluate the

performance of this part of the code. The comparison of the results obtained from the code with the experimental results showed good agreement, confirming the validity of the two-phase part of the model. Overall Improvement in the quality of the results was also observed when compared with previous numerical simulations available in literature.

For the second stage, which is the heat transfer part of the study, the energy equation was activated and the boiling model was added to the code. The RPI boiling model implemented in the code partitions the heat flux on the wall into three different heat transfer mechanisms; convection, evaporation and quenching. The code was modified to account for the effect of each of these mechanisms. Updated versions of different correlations were used in the model. Furthermore, mass, momentum, energy and IAC equations were modified to incorporate the boiling phenomenon. Comparison of the results obtained from the current code with available experimental data on the pipe exit shows that the code generates satisfactory results. The results obtained from the current simulations show significant improvement for many of the important flow parameters in comparison with previous numerical results.

In the last stage, the developed model was extended to an impinging jet. Modifications were made to some of the experimental correlations used for pipe flow in order for the model to be applicable to an impinging jet. The comparison of results obtained from the current simulation and other numerical and experimental studies confirms the accuracy and validity of the current model for the analysis of boiling phenomenon in impinging jets.

CHAPTER 5

CONCLUSIONS AND RECOMMENDATIONS

In the current study, numerical simulations were carried out to investigate the behaviour of impinging jets with different flow configurations. Steady and unsteady analyses as well as adiabatic and non-adiabatic cases were analyzed. The study was divided into three parts. In the first part, the effect of nozzle stand-off distance on mean flow parameters was analyzed using RANS simulations. In the second section, an unsteady simulation was performed to obtain the time history of the flow parameters in an impinging jet with large stand-off distance. Finally, a CFD model was developed for the analysis of boiling heat transfer in an impinging jet using OpenFOAM source code. The significant contributions of this research are summarized below.

Effect of nozzle stand-off distance on impinging jets (Chapter 2):

The performance and efficiency of impinging jets strongly depends on the nozzle stand-off distance. This influence is due to the fact that the core part of the jet ends at a certain axial location, following which a large decay occurs in the jet axial velocity. In the current investigation, we carried out three RANS simulations with different H/D values to evaluate the effect of H/D on mean flow parameters. The three H/D ratios were selected for this analysis representing the small, medium and large stand-off impinging jet cases. Furthermore, it was of interest to analyze the accuracy of different turbulence models for modeling this type of flow, and the results were evaluated by comparing with available experimental results. The Realizable k - ε and RSM models show some over-prediction of the centreline velocity in the impingement zone, but recover to provide a close match to the experimental data near the plate surface. The k - ω

SST model provides good agreement with the experimental results through the impingement zone and very close to the plate.

From this investigation it was found that there is a significant influence of H/D ratio on the behaviour of the impinging jet. For small H/D cases, the three well-known flow regions of an impinging jet were found to be indistinguishable. It was found that the core part of the jet impinged on the plate. By increasing the H/D ratio, the three distinct regions of the impinging jets including free jet, impingement zone and wall region became distinguishable. At small H/D values, two peaks in the wall shear stress distributionexist. However, for large H/D cases, a single peak was observed. The variation of pressure along the plate becomes more gradual when the H/D ratio increases.

Unsteady analysis of impinging jets with large stand-off distance (Chapter 3):

To address some of the unsteady flow related issues that could not be accounted for with a RANS turbulence model in Chapter 2, a Large Eddy Simulation (LES) was carried out for an impinging jet with a large stand-off distance. The choice of LES for this evaluation was based on the fact that it is computationally efficient since it only resolves the large and high energy-containing eddies and the small scales are modeled.

Three different mesh sizes were used to ensure that the mesh requirement in LES was satisfied. The mesh resolution in the wall region was checked to comply with the generally approved LES criteria for wall-attached

flows. The mesh resolution quality inside the domain was also evaluated by comparing the mesh size to the Kolmogorov length scale. To validate the accuracy of the numerical model for unsteady analysis, the frequency of the ring vortices generated in the vicinity of the nozzle was compared with similar previous studies in the literature. It was found that the ring vortices generated by the interaction of the flow exiting the nozzle with the ambient flow in the tank undergo breakdown, stretching and merging and finally transform into large scale structures as they move towards the impingement plate. The vortical patches existing in the ring vortices are found to be the main reason for this transformation.

The frequency of ring vortices that appear close to the nozzle reduces as the vortices move towards the plate. In the impinging zone, the frequency of the structures was significantly lower than the frequency of the ring vortices near the nozzle. The breakdown of ring vortices after five or six diameter from the nozzle is associated with three-dimensionality and unsteady effects which causes the fluid structures to lose their symmetry on approaching the plate. This causes an unsteady pressure fluctuation in the impinging region as well as jet meandering around the axis.

After impingement the flow transforms into a wall jet. The structures hitting the plate result in separation of the flow on the plate, generating separation bubbles in the impinging region which influences the shear stress distribution in the wall region.

126

CFD analysis of boiling heat transfer in impinging jets (Chapter 4):

An Eulerian-Eulerian two-phase flow model using OpenFOAM source code was developed to simulate the boiling heat transfer phenomenon in an impinging jet. The model development process included three stages.

In the first stage, an adiabatic two-phase flow model was developed for pipe flow. The default solver for two-phase flow simulation in OpenFOAM was upgraded to take into account the effect of different interfacial forces and area concentration. The model was used to simulate a benchmark problem and the results showed good agreement with experimental data and an improvement over previous numerical simulations.

In the second part of the model development process, the energy equation and the boiling model were activated. A benchmark experiment was selected for evaluating the quality of the developed model at this stage. The CFD simulation of this experiment showed very close agreement with the experimental results and significant improvement compared to previous simulations, particularly for the bubble size distribution.

Having benchmarked the boiling model for the pipe flow, the model was upgraded to simulate the boiling phenomenon in an impinging jet. For this purpose, the experimental correlations valid for pipe flow were replaced with the ones for impinging jets. Comparison of the present results with the experimental results confirmed the validity of the developed model for impinging jets.

Recommendations for future research:

- Due to the significant influence of the inlet condition on the flow development in jet flows, CFD simulation should be carried out to understand the effect of turbulence at the inlet of the domain. LES studies can be used to capture the influence of turbulence on generation, transfer and break down of vortical structures in the domain. This investigation can lead to a better understanding of the origin of vortical structure breakup in jet flows.

- Another potential future study related to the current research is implementation of more accurate turbulence generation methods at the inlet. The LES in the current study uses the spectral synthesizer method which is based on mean value results obtained from previous RANS studies. Due to the nature of the LES analysis, a real time true turbulence level needs to be introduced at the inlet in order to generate more realistic results. This can be done by performing a separate simulation using LES to capture the time history of the turbulence fluctuations at the inlet and storing this data. Following this, another simulation which uses this time history data at the inlet can be employed to model the entire domain.

- In the current dissertation, RANS and LES studies have been carried out to understand the flow in impinging jets. Based on the nature of these methods they are not as accurate as DNS for flow simulation. DNS will provide more

detailed data for analysis of the behaviour of the steady and unsteady flow features in this type of flow.

- For the boiling simulation of impinging jets, the current simulation uses the OpenFOAM source code, which gives modifying permissions to the user. To improve the quality of the results it is possible to implement new experimental and numerical correlations for different parts of the model. Furthermore, having an open source code, it is possible to extend the model to other 3D geometries.

REFERENCES

Abishek, S., Narayanaswamy, R., Narayanan, V., 2013. Effect of heater size and Reynolds number on the partitioning of surface heat flux in subcooled jet impingement boiling. International Journal of Heat and Mass Transfer, 59: 247-261.

Alekseenko, S.V., Markovich, D.M., 1994. Electro-diffusion diagnostics of wall shear stresses in impinging jets. Journal of Applied Electrochemistry, 24: 626-631.

Antal, S.P., Lahey Jr, R.T., Flaherty, J.E., 1991. Analysis of phase distribution in fully developed laminar bubbly two-phase flow. International Journal of Multiphase Flow, 7: 635-652.

Bartolomej, G.G., Chanturiya, V.M., 1967. Experimental study of true void fraction when boiling subcooled water in vertical tubes. Thermal Engineering, 14: 123–128 (translated from Teploenergetika, 1967, 14(2): 80–83).

Beaubert, F., Viazzo, S., 2003. Large eddy simulation of plane turbulent impinging jets at moderate Reynolds numbers. International Journal of Heat and Fluid Flow, 24: 512–519.

Beltaos, S., Rajaratnam, N., 1974. Impinging circular turbulent jets. Journal of Hydraulic Engineering, ASCE, 100: 1313-1328.

Beltaos, S., Rajaratnam, N., 1977. Impingement of axisymmetric developing jets. Journal of Hydraulic Research, 15(4): 311-326.

Bradshaw, P., Love, E.M., 1961. The normal impingement of a circular air jet over a flat surface. ARC, R&M 3205.

Burns, A.D., Frank, T., Hamill, I., Shi, J.M., 2004. The Favre averaged drag model for turbulence dispersion in Eulerian multi-phase flows. 5th International Conference on Multiphase Flow, ICMF'2004, Yokohama, Japan.

Chapman, D.R., 1979. Computational aerodynamics development and outlook. AIAA Journal, 17(12): 1293-1313.

Chung, Y.M., Luo, K.H., Sandham, N.D., 2002. Numerical study of momentum and heat transfer in unsteady impinging jets. International Journal of Heat and Fluid Flow, 23: 592-600.

Cole, R., 1960. A photographic study of pool boiling in the region of the critical heat flux. AIChE Journal, 6: 533–542.

Colucci, D.W., Viskanta, R., 1996. Effect of nozzle geometry on local convective heat transfer to a confined impinging air jet. Experimental Thermal and Fluid Science, 13: 71-80.

Cooper, D., Jackson, D.C., Launder, B.E., Liao, G.X., 1993. Impinging jet studies for turbulence model assessment-I. Flow-field experiments. International Journal of Heat and Mass Transfer, 36: 2675-2684.

Coursey, J.S., 2007. Enhancement of spray cooling heat transfer using extended surfaces andnanofluids. Ph.D. Dissertation, Department of Mechanical Engineering, University of Maryland, Maryland, USA.

Craft, T., Graham, L., Launder, B.E., 1993. Impinging jet studies for turbulence model assessment-II. An examination of the performance of four turbulence models. International Journal of Heat and Mass Transfer, 36: 2685-2697.

Dairay, T., Fortuné, V., Lamballais, E., Brizzia, L.E., 2015. Direct numerical simulation of a turbulent jet impinging on a heated wall. Journal of Fluid Mechanics, 764: 362-394.

Deshpande, M.D., Vaishnav, R.N., 1982. Submerged laminar jet impingement on a plane. Journal of Fluid Mechanics, 114: 213-236.

Dewan, A., Dutta, R., Srinivasan, B., 2012. Recent trends in computation of turbulent jet impingement heat transfer. Heat Transfer Engineering, 33 (4–5): 447–460.

El Hassan, M.,Assoum, H. H., Martinuzzi, R., Sobolik, V., Abed-Meraim, K., Sakout, A., 2013. Experimental investigation of the wall shear stress in a circular impinging jet. Physics of Fluids, 25, 077101.

FLUENT 6.3 User's Guide, 2006. FLUENT Inc., Lebanon, New Hampshire, USA.

Frank, T., 2005. Advances in computational fluid dynamics (CFD) of 3-dimensional gas–liquid multiphase flows. NAFEMS Seminar "Simulation of Complex Flows (CFD)", Wiesbaden, Germany, April 25–26, 2005, pp. 1–18.

Garnier, J., Manon, E., Cubizolles, G., 2001. Local measurements on flow boiling of refrigerant 12 in a vertical tube. Multiphase Science and Technology, 13: 1-111.

Germano, M., Piomelli, U., Moin, P., Cabot, W.H., 1991. A dynamic subgrid-scale eddy viscosity model. Physics of Fluids, A3, 1760-1765.

Giralt, F., Chia, C., Trass, O., 1977. Characterization of the impingement region in an axisymmetric turbulent jet. Industrial & Engineering Chemistry Fundamentals, 16 (1): 21-28.

Grossetête, C., 1995. Caractérisation expérimentale et simulation de l'évolution d'un écoule mentdiphasique à bulles ascendant dansune conduite verticale, Ph.D. Dissertation, Ecole Centrale Paris.

Hadziabdic, M., Hanjalic, K., 2008. Vortical structures and heat transfer in a round impinging jet. Journal of Fluid Mechanics, 596: 221–260.

Hall, J.W., Ewing, D., 2006. On the dynamics of the large-scale structures in round impinging jets. Journal of Fluid Mechanics, 555: 439–458.

Han, B., Goldstein, R.J., 2003. Instantaneous energy separation in a free jet. Part I. Flow measurement and visualization. International Journal of Heat and Mass Transfer, 46: 3975–3981.

Hattori, H., Nagano, Y., 2004. Direct numerical simulation of turbulent heat transfer in plane impinging jet. International Journal of Heat and Fluid Flow, 25: 749-758.

Hibiki, T., Ishii, M., 2002. Development of one-group interfacial area transport equation in bubbly flow systems. International Journal of Heat and Mass Transfer, 45: 2351-2372.

133

Hoffmann, K.A., Chiang, S.T., 2000. Computational Fluid Dynamics, Volume III, Fourth Edition. Engineering Education System, Wichita, KS, USA.

Ishii, M., Zuber, N., 1979. Drag coefficient and relative velocity in bubbly, droplet or particulate flow. AIChE Journal, 25: 843-855.

Jeong, J., Hussain, F., 1995. On the identification of a vortex. Journal of Fluid Mechanics, 285: 69-94.

Katto, Y., Kunihiro, M., 1973. Study the mechanism of burn-out in boiling system of high burn-out heat flux. Bulletin of JSME, 16(99): 1357-1366.

Kataoka, K., Mizushina, T., 1974. Local enhancement of the rate of heat transfer in an impinging round jet by free-stream turbulence. Proceedings of the Fifth International Conference in Heat Transfer, Tokyo, Japan, 305-309.

Krepper, B., Koncar, B., Egorov, Y., 2007. Modelling of subcooled boiling—concept, validation and application to fuel assembly design. Nuclear Engineering and Design, 237: 716–731.

Krepper, E., Rzehak, R., 2011. CFD for subcooled flow boiling: simulation of DEBORA experiments. Nuclear Engineering and Design, 241: 3851-3866.

Krepper, E., Rzehak, R., Lifante, C., Frank, T., 2013. CFD for subcooled flow boiling: coupling wall boiling and population balance models. Nuclear Engineering and Design, 241: 3851-3866.

Kurul, N., Podowski, M.Z., 1990. Multidimensional effects in forced convection subcooled boiling. Proceeding of the 9th International Heat Transfer Conference, Jerusalem, Israel.

Kurul, N., Podowski, M. Z., 1991. On the modeling of multidimensional effects in boiling channels. Proceedings of the 27th National Heat Transfer Conference, Minneapolis, Minnesota, USA.

Kunkelmann, C., Stephan, P., 2010. Numerical simulation of the transient heat transfer during nucleate boiling of refrigerant HFE-7100. International Journal of Refrigeration, 33(7): 1221-1228.

Launder, B.E., Reece, G.J., Rodi, W., 1975. Progress in the development of a Reynolds-stress turbulence closure. Journal of Fluid Mechanics, 68(3): 537-566.

Launder, B.E., Spalding, D.B., 1974. The numerical computation of turbulent flows. Computer Methods in Applied Mechanics and Engineering, 3: 269-289.

Lemmert, M., Chawla, J.M., 1977. Influence of flow velocity on surface boiling heat transfer coefficient. Heat Transfer and Boiling (eds. E. Hahne, and U. Grigull), Academic Press, 237-247.

Manceau, R., Perrin, R., Hadžiabdić, M., Benhamadouche, S., 2014. Investigation of the interaction of a turbulent impinging jet and a heated, rotating disk. Physics of Fluids, 26, 035102: 1-30.

Menter, F.R., 1994. Two-equation eddy-viscosity turbulence models for engineering applications. AIAA Journal, 32(8): 1598-1605.

Michta, E., 2011. Modeling of Subcooled Nucleate Boiling with OpenFOAM. M.Sc. Thesis, KTH University.

Michta, E., Fu, K., Anglart, H., Angele,K., 2012. Numerical predictions of bubbly two-phase flows with OpenFOAM. Journal of Computational Multiphase Flows, 4(4): 351-362.

Mikic, B.B., Rohsenow, W.M., 1969. A new correlation of pool-boiling data including the fact of heating surface characteristics. ASME Journal of Heat Transfer, 91: 245–250.

Moraga, F.J., Bonetto, F.J., Lahey, R.T., 1999. Lateral forces on spheres in turbulent uniform shear flow. International Journal of Multiphase Flow, 25: 1321-1372.

Narumanchi, S., Treshko, A., Bharathan, D., Hassani, V., 2008. Numerical simulations of nucleate boiling in impinging jets: applications in power electronics cooling. International Journal of Heat and Mass Transfer, 51: 1-12.

Nishino, K., Samada, M., Kasuya, K., Torii, K., 1996. Turbulence statistics in the stagnation region of an axisymmetric impinging jet flow. International Journal of Heat and Fluid Flow, 17(3): 193-201.

Olsson, M., Fuchs, L., 1998. Large eddy simulation of a forced semiconfined circular impinging jet. Physics of Fluids, 10: 476-486.

OpenCFD Limited, http://www.openfoam.com.

Patankar, S.V., Spalding, D.B., 1972. A calculation procedure for heat, mass and momentum transfer in three-dimensional parabolic flows. International Journal of Heat and Mass Transfer, 15: 1787-1806.

Piomelli, U., Chasnov, J.R., 1996. Large-eddy simulations: theory and applications. In Transition and Turbulence Modelling, page 269. (eds. A. Henningson, K. Hallback, L. Alfredsson, M. Johansson). Kluwer Academic Publishers, Dordrecht.

Pope, S.B., 2000. Turbulent Flows. Cambridge University Press, Cambridge, UK.

Rajaratnam, N., Zhu, D.Z., Rai, S.P., 2010. Turbulence measurements in the impinging region of a circular jet. Canadian Journal of Civil Engineering, 37(5): 782-786.

Roussinova, V., Balachandar, R., 2012. Experimental study of a round impinging jet, 16th International Symposium on Applied Laser Techniques to Fluid Mechanics, Lisbon, Portugal.

Sato, Y., Sadatomi, M., Sekoguchi, K., 1981. Momentum and heat transfer in two-phase bubble flow-I. International Journal of Multiphase Flow, 7: 167–177.

Second ERCOFTAC-IAHR Workshop on Refined Modelling, 1993. Round normally impinging turbulent jet and turbulent flow through tube bank sub-

channel. 16th Meeting of the IAHR Working Group on Refined Flow Modelling, University of Manchester, Inst. of Sci. and Tech., UK.

Shademan, M., Balachandar, R., Barron, R.M., 2013. CFD analysis of the effect of nozzle stand-off distance on turbulent impinging jets. Canadian Journal of Civil Engineering, 40(7): 603-612.

Shih, T.H., Liou, W.W., Shabbir, A., Yang, Z., Zhu, J., 1995. A new k - ε eddy-viscosity model for high Reynolds number turbulent flows - model development and validation. Computers and Fluids, 24: 227-238.

Shinneeb, A.M., Bugg, J.D., Balachandar, R., 2008. Quantitative investigation of vortical structures in the near-exit region of an axisymmetric turbulent jet. Journal of Turbulence, 9(19): 1–20.

Tandalam, A., Balachandar, R., Barron, R., 2010. Reynolds number effects on the near-exit region of turbulent jets. Journal of Hydraulic Engineering,136(9): 633-641.

Tian, J., Roussinova, V., Balachandar, R., 2012. Characteristics of a jet in the vicinity of a free surface. Journal of Fluids Engineering, 134: 31204.

Tolubinsky, V.I., Kostanchuk, D.M., 1970. Vapor bubble growth rate and heat transfer intensity at subcooled water boiling. 4th International Heat Transfer Conference, Paris, France, 5, Paper No. B-2.8.

Tomiyama, A., 1998. Struggle with computational bubble dynamics. ICMF'98, 3rd International Conference on Multiphase Flow, 1-18, Lyon, France.

Tomiyama, A., Tamai, H., Zun, I., Hosokawa, S., 2002. Transverse migration of single bubbles in simple shear flows. Chemical Engineering Science, 57: 1849-1858.

Tsubokura, M., Kobayashi, T., Taniguchi, N., Jones, W.P., 2003. A numerical study on the eddy structures of impinging jets excited at the inlet. International Journal of Heat and Fluid Flow, 24: 500-511.

Uddin, N., Neumann, S.O., Weigand, B., 2013. LES simulations of an impinging jet: on the origin of the second peak in the Nusselt number distribution. International Journal of Heat and Mass Transfer, 57(1): 356-368.

Unal, H.C., 1976. Maximum bubble diameter, maximum bubble growth time and bubble growth rate. International Journal of Heat and Mass Transfer, 19: 643–649.

Voke, P.R., Gao, S., 1998. Numerical study of heat transfer from an impinging jet. International Journal of Heat and Mass Transfer, 41: 671–680.

Xu, G., Antonia, R.A., 2002. Effect of different initial conditions on a turbulent round free jet. Experiments in Fluids, 33: 677-683.

Wellek, R.M., Agrawal, A.K., Skelland, A.H.P., 1966. Shape of liquid drops moving in liquid media. AIChE Journal, 12: 854-860.

Wolfert, K., Burwell, M.J., Enix, D., 1978. Non-equilibrium mass transfer between liquid and vapour phases during depressurization process in transient two-

phase flow. Proceeding of 2nd CSNI Specialists Meeting, 2: 1377-1387, Paris, France.

Wu, W., Piomelli, U., 2014. Large-eddy simulation of impinging jets with embedded azimuthal vortices. Journal of Turbulence, 16(1): 44-66.

Yao, W., Morel, C., 2004. Volumetric interfacial area prediction in upward bubbly two-phase flow. International Journal of Heat and Mass Transfer, 47: 307-328.

Yu, Y., Shademan, M., Balachandar, R., Barron, R., 2012. A CFD study of the effect of geometry variations on flow in a nozzle. Engineering Applications of Computational Fluid Mechanics, 6(3): 412-425.

Yule, A.J., 1978. Large-scale structure in the mixing layer of a round jet. Journal of Fluid Mechanics, 3: 413–432.

Zuber, N., 1964. On the dispersed two-phase flow in the laminar flow regime. Chemical Engineering Science, 19(11): 897-917.

Zuckerman, N., Lior, N., 2005.Impinging heat transfer: correlations and numerical modeling. Journal of Heat Transfer, 127(5): 544–552

APPENDIX A- REPRINT PERMISSIONS

Copyright for Chapter 2

RightsLink

Copyright Clearance Center

Thank You For Your Order!

Dear Mr. mehrdad shademan,

Thank you for placing your order through Copyright Clearance Center's RightsLink service. NRC Research Press has partnered with RightsLink to license its content. This notice is a confirmation that your order was successful.

Your order details and publisher terms and conditions are available by clicking the link below:
http://s100.copyright.com/CustomerAdmin/PLF.jsp?ref=2dd7df21-0e93-4b3a-8b13-561b8e139214

Order Details
Licensee: mehrdad shademan
License Date: Dec 1, 2014
License Number: 3520000020464
Publication: Canadian Journal of Civil Engineering
Title: CFD analysis of the effect of nozzle stand-off distance on turbulent impinging jets
Type Of Use: Thesis/Dissertation
Total: 0.00 CAD

To access your account, please visit https://myaccount.copyright.com.

Please note: Online payments are charged immediately after order confirmation; invoices are issued daily and are payable immediately upon receipt.

To ensure that we are continuously improving our services, please take a moment to complete our customer satisfaction survey.

B.1:v4.2

Copyright for Chapters 3 and 4

Dear Mr. Shademan,

It has been confirmed that your papers were presented at the IMECE2014.It is our pleasure to grant you permission to publish any part or all of the following ASME materials:

- "Large Edddy Simulation of Round Impinging Jets with Large Stand-off Distance," by M. Shademan, V. Roassinova, R. Barron, R. Balachandar, Paper No. IMECE-37194.
- "CFD Simulation of Boiling Heat Transfer using Open Foam," by M. Shademan, R. Barron, R. Balachandar, Paper No. IMECE-37585.

as cited in your letter in the Thesis entitled CFD Simulation of Impinging Jets Flows and Boiling Heat Transfer to be published by University of Windsor.

Permission is granted for the specific use as stated herein and does not permit further use of the materials without proper authorization. Proper attribution must be made to the author(s) of the materials. Please note: if any or all of the figures and/or Tables are of another source, permission should be granted from that outside source or include the reference of the original source. ASME does not grant permission for outside source material that may be referenced in the ASME works.

As is customary, we request that you ensure proper acknowledgment of the exact sources of this material, the authors, and ASME as original publisher. Acknowledgment must be retained on all pages printed and distributed.

Many thanks for your interest in ASME publications.

Sincerely,

Beth Darchi
Publishing Administrator
ASME
2 Park Avenue, 6th Floor
New York, NY 10016-5990
Tel 1.212.591.7700
darchib@asme.org

VITA AUCTORIS

NAME: Mehrdad Shademan

PLACE OF   Ghochan, Iran
BIRTH:

YEAR OF BIRTH: 1977

EDUCATION: Ferdowsi University of Mashhad, B.Sc. in
                            Mechanical Engineering, Mashhad, Iran, 2000

                            Iran University of Science and Technology, M.Sc. in
                            Mechanical Engineering, Tehran, Iran 2003

                            University of Western Ontario, M.E.Sc. in
                            Mechanical Engineering, London, Ontario, Canada,
                            2010

                            University of Windsor, Ph.D. in Mechanical
                            Engineering, Windsor, Ontario, Canada, 2015